LAJC **LATIN-AMERICAN
JOURNAL OF
COMPUTING**

Associated Institutions:

udla

UTA
UNIVERSIDAD
TÉCNICA DE AMBATO

UDEM

UPR
Recinto Universitario de Mayagüez

ESCUELA POLITÉCNICA NACIONAL

MISIÓN
La Escuela Politécnica Nacional es una Universidad pública, laica y democrática que garantiza la libertad de pensamiento de todos sus integrantes, quienes están comprometidos con aportar de manera significativa al progreso del Ecuador. Formamos investigadores y profesionales en ingeniería, ciencias, ciencias administrativas y tecnología, capaces de contribuir al bienestar de la sociedad a través de la difusión del conocimiento científico que generamos en nuestros programas de grado, posgrado y proyectos de investigación. Contamos con una planta docente calificada, estudiantes capaces y personal de apoyo necesario para responder a las demandas de la sociedad ecuatoriana.

VISIÓN
En el 2024, la Escuela Politécnica Nacional es una de las mejores universidades de Latinoamérica con proyección internacional, reconocida como un actor activo y estratégico en el progreso del Ecuador. Forma profesionales emprendedores en carreras y programas académicos de calidad, capaces de aportar al desarrollo del país, así como promover y adaptarse al cambio y al desarrollo tecnológico global. Posiciona en la comunidad científica internacional a sus grupos de investigación y provee soluciones tecnológicas oportunas e innovadoras a los problemas de la sociedad.

La comunidad politécnica se destaca por su cultura de excelencia y dinamismo al servicio del país dentro de un ambiente de trabajo seguro, creativo y productivo, con infraestructura de primer orden.

ACCIÓN AFIRMATIVA
La Escuela Politécnica Nacional es una institución laica y democrática, que garantizar la libertad de pensamiento, expresión y culto de todos sus integrantes, sin discriminación alguna. Garantiza y promueve el reconocimiento y respeto de la autonomía universitaria, a través de la vigencia efectiva de la libertad de cátedra y de investigación y del régimen de cogobierno.

https://www.epn.edu.ec

FACULTAD DE INGENIERÍA DE SISTEMAS

https://fis.epn.edu.ec

MISIÓN

La Facultad de Ingeniería de Sistemas es el referente de la Escuela Politécnica Nacional en el campo de conocimiento y aplicación de las Tecnologías de Información y Comunicaciones; actualiza en forma continua y pertinente la oferta académica en los niveles de pregrado y postgrado para lograr una formación de calidad, ética y solidaria; desarrolla proyectos de investigación, vinculación y proyección social en su área científica y tecnológica para solucionar problemas de transcendencia para la sociedad.

VISIÓN

La Facultad de Ingeniería de Sistemas está presente en posiciones relevantes de acreditación a nivel nacional e internacional y es referente de la Escuela Politécnica Nacional en el campo de las Tecnologías de la Información y Comunicaciones por su aporte de excelencia en las carreras de pregrado y postgrado que auspicia, la calidad y cantidad de proyectos de investigación, vinculación y proyección social que desarrolla y su aporte en la solución de problemas nacionales a través del uso intensivo y extensivo de la ciencia y la tecnología.

LATIN-AMERICAN JOURNAL OF COMPUTING

—

EDITORIAL

Denys Flores
PhD.

Editor LAJC
Escuela Politécnica Nacional,
Ecuador

Modelado Computacional: Resolviendo Problemas Actuales para un Mejor Futuro

En los últimos años, la Revista Latin-American Journal of Computing (LAJC) ha servido como un espacio para presentar investigaciones de vanguardia en diferentes áreas de la Informática y las Ciencias de la Computación. En nuestro número actual, hemos sido testigos del resurgimiento del modelado computacional como una herramienta fascinante y poderosa para dar forma a nuestro futuro al abordar importantes problemas cotidianos. Estamos encantados de presentar a nuestros lectores una colección de artículos excepcionales en este campo, que enfatizan el poder transformador del modelado computacional y las matemáticas para comprender y resolver problemas en varios dominios.

En primer lugar, explorando el ámbito de los sistemas de alerta temprana, Anika Manz et al. resalta la importancia de las técnicas de modelado precisas para detectar situaciones de emergencia e implementar las medidas de seguridad necesarias. Su trabajo examina el rendimiento del modelo SWASH en el prototipo de Ericeira, comparándolo con el sistema de alerta temprana HIDRALERTA. Sus hallazgos demuestran la necesidad de seleccionar el enfoque de modelado más adecuado para mejorar la precisión y confiabilidad de los sistemas de alerta temprana.

En el dominio de la predicción de enfermedades, Ilha da Silva et al. analiza el ampliamente utilizado modelo Susceptible-Infectado-Recuperado (SIR) y sus implicaciones para comprender la propagación de enfermedades en una población. Al enfatizar la naturaleza no lineal de la dinámica del modelo SIR, los autores destacan la necesidad de emplear métodos numéricos para obtener soluciones aproximadas. Asimismo, Carolina Maurmann et al. abordan la intrigante pregunta relacionada con la propagación de enfermedades entre distintas poblaciones, cada una de las cuales posee inmunidad parcial a las cepas circulantes. Este estudio contribuye a la comprensión de la aplicación de modelos compartimentales multi-fraccionados en epidemiología.

Además de estas notables contribuciones, LAJC también presenta algunos estudios en otras aplicaciones importantes del modelado computacional. Por ejemplo, Rafael da Silva et al. analiza el comportamiento dinámico de grandes estructuras como puentes y viaductos, cuyo desempeño requiere un monitoreo frecuente. Los autores discuten la importancia de modelar la deflexión de estas estructuras; particularmente, cuando aumentan las posibilidades de tener condiciones de mantenimiento adversas debido a las vibraciones producidas por los vehículos pesados. Del mismo modo, Elisa Ferreira et al. explora el problema del coeficiente de rigidez en micro y nano vigas. Al introducir el método de regularización iterativo de Landweber, los autores proponen una solución más estable para identificar la rigidez de dichas estructuras, incluso en presencia de ruido en las mediciones de deformación.

En resumen, el último número de LAJC destaca la evaluación crítica de los enfoques de modelado computacional, la selección de métodos numéricos apropiados y la consideración de complejidades dinámicas en varios dominios. Los trabajos presentados en este número demuestran un creciente interés de investigación en esta área para resolver problemas complejos, llamando a la colaboración constante, el intercambio de conocimientos y la innovación dentro de la comunidad de científicos informáticos.

Invitamos a nuestros lectores a explorar este nuevo número, que muestra estudios interesantes que nos invitan a adoptar técnicas de resolución de problemas apalancadas por el poder transformador del modelado computacional y su profundo impacto en nuestra sociedad.

Denys A. Flores

Editor en Jefe

Computer Modeling: Solving Current Problems for a Better Future

In the last years, the Latin-American Journal of Computing (LAJC) has served as a venue to showcase groundbreaking research in different areas of Informatics and Computer Science. In our current issue, we have witnessed the resurgence of computer modeling as a fascinating and powerful tool for shaping our future by tackling important day-to-day problems. We are thrilled to present to our readership, a collection of exceptional papers in this field, which emphasize the transformative power of computer modeling and mathematics to understand and solve problems in various domains.

Firstly, exploring the realm of early warning systems, Anika Manz et al. underscore the significance of accurate modeling techniques in detecting emergency situations and implementing necessary safety measures. Their work examines the performance of the SWASH model in the Ericeira prototype, comparing it with the HIDRALERTA early warning system. Their findings demonstrate the need to select the most suitable modeling approach for enhancing the accuracy and reliability of early warning systems.

In the domain of disease prediction, Ilha da Silva et al. analyze the widely used Susceptible-Infected-Recovered (SIR) model and its implications for understanding illness spreading in a population. By emphasizing the non-linear nature of the SIR model's dynamics, the authors highlight the necessity of employing numerical methods to obtain approximate solutions. Likewise, Carolina Maurmann et al. tackle the intriguing question of disease spreading between distinct populations, each possessing partial immunity to circulating strains. This study contributes to the understanding of the application of multi-fractional compartmental models in epidemiology.

In addition to these remarkable contributions, LAJC also presents some studies in other important applications of computer modeling. For instance, Rafael da Silva et al. discusses the dynamic behavior of large structures such as bridges and viaducts, the performance of which requires frequent monitoring. The authors discuss the importance of modeling the deflection of these structures; particularly, when the chances of having adverse maintenance conditions increase due to the vibrations produced by heavy vehicles. Similarly, Elisa Ferreira et al. explore the stiffness coefficient problem in micro and nano beams. By introducing Landweber's iterative regularization method, the authors propose a more stable solution for identifying stiffness in such structures, even in the presence of noise in strain measurements.

In short, the latest issue of LAJC highlights the critical evaluation of computer modeling approaches, the selection of appropriate numerical methods, and the consideration of dynamic complexities across various domains. The works submitted to this issue demonstrate an increasing research interest in this area to solve complex problems, calling out to constant collaboration, knowledge exchange, and innovation within the community of computer scientists.

We invite our readership to explore this new issue, which showcase interesting studies that invite us to embrace problem solving techniques leveraged by the transformative power of computer modeling and its profound impact on our society.

Denys A. Flores

Editor-in-Chief

LAJC

LATIN-AMERICAN JOURNAL OF COMPUTING

Reviewers

Carlos Anchundia, PhD.
Escuela Politécnica Nacional

Daniela Buske, PhD.
Universidade Federal de Pelotas

Elizaldo Domingues, PhD.
Federal University of Rio Grande - FURG

Emanuel Estrada, PhD.
Federal University of Rio Grande - FURG

Fernando Molina, PhD.
Universidad Nacional de Chimborazo

Fran Lobato, PhD.
Universidade Federal De Uberlândia

Jenny Torres, PhD.
Escuela Politécnica Nacional

Juan Solano, PhD.
Universidad Nacional de Loja

Julián Galindo, PhD.
Escuela Politécnica Nacional

Julio Sandobalín, PhD.
Escuela Politécnica Nacional

Liércio Isoldi, PhD.
Federal University of Rio Grande - FURG

Luis Urquiza, PhD.
Escuela Politécnica Nacional

Marco Galarza, MSc.
Universidad de las Américas

Régis Quadros, PhD.
Universidade Federal de Pelotas

Richard Rivera, PhD.
Escuela Politécnica Nacional

Roberto Andrade, MSc.
Escuela Politécnica Nacional

Vera Ferreira, PhD.
Universidade Federal do Pampa

TABLE OF CONTENTS

Implementation of the SWASH model into HIDRALERTA system

Anika Manz
Hidraulics and Environment Department
National Laboratory of Civil Engineering
Lisbon, Portugal
a67280@ualg.pt
ORCID: 0009-0009-7519-3613

Ana Catarina Zózimo
Hidraulics and Environment Department
National Laboratory of Civil Engineering
Lisbon, Portugal
aczozimo@lnec.pt
ORCID: 0000-0001-5948-6824

Conceiçao Fortes
Hidraulics and Environment Department
National Laboratory of Civil Engineering
Lisbon, Portugal
jfortes@lnec.pt
ORCID: 0000-0002-5503-7527

Liliana Pinheiro
Hidraulics and Environment Department
National Laboratory of Civil Engineering
Lisbon, Portugal
lpinheiro@lnec.pt
ORCID: 0000-0001-8604-5450

Juan L. Garzon
Centre for Marine and Environmental
Research
Universidade do Algarve
Faro, Portugal
jlhervas@ualg.pt

LATIN-AMERICAN JOURNAL OF COMPUTING (LAJC), Vol X, Issue 2, July 2023

A. Manz, A. C. Zózimo, C. Fortes, L. Pinheiro and J.L. Garzon,
"Implementation of the SWASH model into HIDRALERTA system",
Latin-American Journal of Computing (LAJC), vol. 10, no. 2, 2023.

Implementation of the SWASH model into HIDRALERTA system

Anika Manz
Hidraulics and Environment Department
National Laboratory of Civil Engineering
Lisbon, Portugal
a67280@ualg.pt
ORCID: 0009-0009-7519-3613

Ana Catarina Zózimo
Hidraulics and Environment Department
National Laboratory of Civil Engineering
Lisbon, Portugal
aczozimo@lnec.pt
ORCID: 0000-0001-5948-6824

Conceiçao Fortes
Hidraulics and Environment Department
National Laboratory of Civil Engineering
Lisbon, Portugal
jfortes@lnec.pt
ORCID: 0000-0002-5503-7527

Liliana Pinheiro
Hidraulics and Environment Department
National Laboratory of Civil Engineering
Lisbon, Portugal
lpinheiro@lnec.pt
ORCID: 0000-0001-8604-5450

Juan L. Garzon
Centre for Marine and Environmental Research
Universidade do Algarve
Faro, Portugal
jlhervas@ualg.pt

Abstract— Early warning systems are an important tool for local authorities to detect emergency situations in advance and initiate the necessary safety measure. These systems often depend on numerical models to estimate wave overtopping in the affected areas. The SWASH model has shown to deliver good results in recent overtopping studies. The To-SEAlert project has the aim of increasing the efficiency, robustness and reliability of the HIDRALERTA early warning system. This study shows a first intent to implement the SWASH model to simulate wave overtopping for the Ericeira prototype. SWASH was implemented for one breakwater profile to simulate the overtopping discharge and evaluate the associated risk levels. It was compared to the current approach used in HIDRALERTA, which resorts to a neural network trained with a physical modeling database, NN_OVERTOPPING2. Finally, both approaches were compared with previously analyzed video images of the breakwater. The results showed that SWASH generally overestimates overtopping and is not in good agreement with the video images. NN_OVERTOPPING2 has a better agreement with the video images. A possible reason for the overestimation might be the wave direction, which cannot be included in one-dimensional simulations in SWASH.

Keywords— *Early Warning System, Wave Overtopping, Risk Reduction, SWASH model*

I. INTRODUCTION

Early Warning Systems (EWS) are fundamental tools for local authorities to prevent damage and loss of lives due to coastal flooding during storms. Among the different early warning systems dealing with coastal hazards, there is a variety of systems aiming at forecasting wave-induced overtopping, relying on accurate wave overtopping estimations by numerical models.

As wave overtopping at coastal structures is a complex phenomenon and depends on different parameters, the existing methods that can be used to estimate and simulate it are diverse. The parameters considered for the estimation of overtopping include, for example, the incident significant wave height, the spectral wave period at the toe of the structure (the spectral wave period is preferred to either the peak period, or the average period, as it gives more weight to the longer periods in the spectrum), the crest freeboard and the slope of the structure, as well as other geometrical features [1].

While the application of (semi-) empirical formulas is restricted to specific geometries, structure configurations and wave conditions, the prediction of wave overtopping under different or more complex conditions can be a challenge. Therefore, in cases where those formulae fail to give accurate estimations, numerical models can be used to model overtopping at coastal structures. As overtopping is a nonlinear, highly dynamic and stochastic phenomenon, the focus of the efforts of engineers and researchers lies on the modelling of the entire process that leads to the wave-induced overtopping [2].

A recent approach to model wave overtopping is based on the dispersive nonlinear shallow water (NLSW) equations, which allow non-hydrostatic pressure, as well as a resolution of the vertical flow and its structure. The SWASH model [3] numerically simulates non hydrostatic, free-surface, rotational flows in one or two horizontal dimensions. As the governing equations are NLSW equations and include non hydrostatic pressure, they can describe complex and rapidly changing flows in detailed topo-bathymetries that are often found in coastal flooding events. Therefore, the model is able to simulate shallow water flows and nearshore processes, including wave propagation, breaking and runup, wave transmission through structures, non-linear interaction and wave-induced circulation [3].

Several studies on wave overtopping have been carried out using the SWASH model in past years, e.g. [2], [4]–[6]. Zhang et al. [7], for example, computed mean overtopping discharge over a breakwater with an armour layer of Accropode and compared their results with the physical model results of the CLASH database. The authors discovered the necessity to properly calibrate the model to obtain the apparent friction coefficient of the armour layer and to meet the physical model results for the mean overtopping discharge. In the calibration process, they found that the friction coefficient is correlated with the relative crest freeboard Rc/Hs and the wave steepness Sop and developed an empirical equation to be used for the determination of the friction coefficient of Accropode in future studies.

The performance of SWASH was also compared with two numerical models based on the full Navier-Stokes equations, namely DualSPHysics and FLOW-3D [8]. For the estimation of wave overtopping and the impact on a seawall, reasonable predictions were observed from all three models, with SWASH having a significantly lower computational cost than the other two.

Although the development of EWS is still in early stages, efforts have been made to implement these systems in Europe, e.g. through the iCoast [9] and RISC-KIT project [10], where the latter uses the numerical models XBeach (for open beaches) and SWASH (for harbors, pocket beaches and revetments) to simulate overtopping and flooding.

HIDRALERTA [11]–[15] is an EWS for forecast and risk assessment of wave overtopping in coastal zones. It provides forecasts 72 hours in advance and with a 3-hour interval, of wave characteristics and the risk levels associated with specific port activities and coastal receptors. The system uses datasets of several years of sea-wave/water level characteristics and/or pre-defined scenarios, to evaluate wave overtopping and flooding risks of the protected areas.

Eight prototypes are operational in the HIDRALERTA system, five in mainland Portugal (Ericeira and Sines harbours, and Costa da Caparica, Praia de Faro and Quarteira coastal zones) and three in the Azores archipelago (Praia da Vitória, S. Roque do Pico and Madalena do Pico harbours). Presently, HIDRALERTA is being extended to the port of Peniche. The system gets the offshore boundary conditions (wind an wave characteristics) from ECMWF forecasts for the north Atlantic region, which are then propagated to the shore using the wave propagation models SWAN [16] and DREAMS [17]. The astronomical tide is obtained with the XTIDE model [18]. In harbor areas (Fig. 1), the neural network NN_OVERTOPPING2 [19] computes the estimated mean overtopping discharge, q, at each cross-section of the structure. As input conditions, the results of the DREAMS and XTIDE models are used. Warnings are triggered when pre-set thresholds for q are exceeded.
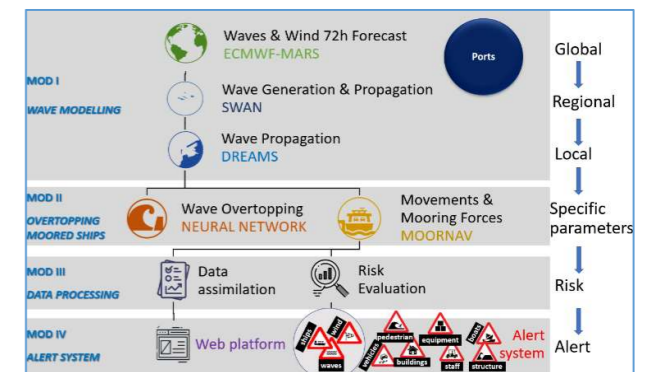
Fig. 1. Structure of the HIDRALERTA system for the harbour prototypes

This study describes a first effort to implement the numerical model SWASH [3] to replace NN_OVERTOPPING2 in the HIDRALERTA system for the Ericeira harbor prototype. SWASH is a numerical model that simulates the wave propagation and transformations nearshore and in shallow waters and is also capable of computing the amount of water that overtops the coastal structure in the sea-land interface. Several non-linear physical phenomena are present in its formulation, some explicitly and others are parameterized, thus needing an adequate calibration in order to achieve good results. On the other hand, NN_OVERTOPPING2 is a tool that estimates the mean overtopping of a structure based on a set of data obtained from physical models. The SWASH model is considered a robust process-based model with high accuracy of simulating wave propagation in shallow water [20]. As any point in the numerical domain can be specified in the output of the model, it allows to estimate the inland incursion of overtopping discharges or, in the case of two-dimensional models, the flooded area, and the wave propagation along the domain, which the neural network tool NN_OVERTOPPING2 is not capable of.

Within the scope of the To-SEAlert project, SWASH was applied for one of the cross-sections of the structure to compute the mean overtopping discharge for a range of test cases and to compare the results and the associated risk levels with NN_OVERTOPPING2.

II. METHODOLOGY

A. Model Setup

Ericeira harbor is located on the west coast of Portugal and is sheltered by a 430 m long breakwater, oriented to the south-west, with a quay in the rear side (Fig. 2). The profile chosen for the implementation of the SWASH model has an orientation of 309°N, it has an armor layer of tetrapods (Fig. 2) and is in the vicinity of a quay on the lee side of the breakwater.

A. Manz, A. C. Zózimo, C. Fortes, L. Pinheiro and J.L. Garzon,
"Implementation of the SWASH model into HIDRALERTA system",
Latin-American Journal of Computing (LAJC), vol. 10, no. 2, 2023.

Fig. 2. Ericeira breakwater and the profile that was chosen for simulations

Overtopping simulations with SWASH were performed in a one-dimensional mode for a computational period of 131 minutes with an additional spin-up period of 15% of the computational period and an initial timestep of 0.01 seconds. An automatic time step control was implied with a maximum Courant number of 0.5 and a minimum Courant number of 0.1. The recommended number of vertical layers was checked, following the instructions of the user manual, which resulted in one vertical layer for all simulations. To account for bottom roughness, a different Manning friction coefficient was applied to the offshore area (0.019 s/(m$^{1/3}$), the user's manual default Manning friction coefficient for wave simulations over large distances) and to the armor layer of tetrapods (0.078 s/(m$^{1/3}$)). The latter is as an average value that was chosen based on the results of [21], where the Manning coefficient was calibrated for the same breakwater profiles for SWASH simulations.

The length of the numerical domain was 419 m, where 334.5 m corresponded to the area offshore, 48 m to the breakwater and 36.5 m to the lee side of the structure (Fig. 3). The bathymetry was constructed with data acquired from EMODnet (150 m grid spacing) and DGTerritorio (LiDAR survey of 2011, 2 m spacing). The profile had a constant grid spacing of 0.5 m.
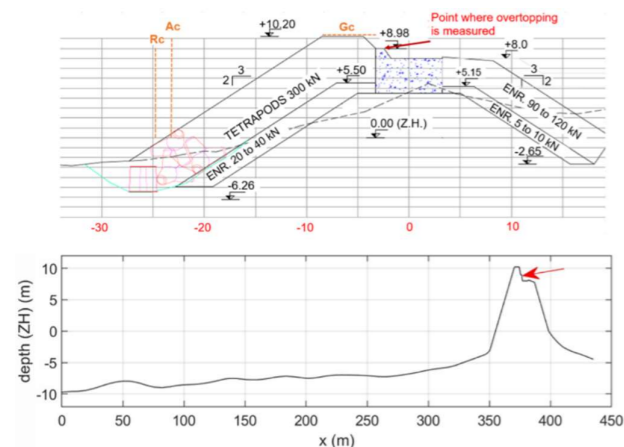

Fig. 3. Cross-section of the breakwater profile used for the simulations (top) and bathymetry used in SWASH, with the cross-shore distance referred to the wavemaker boundary and red arrow indicating where overtopping results were extracted (bottom)

At the offshore boundary, a JONSWAP wave spectrum defined the shape of the irregular waves, with a peak enhancement parameter γ=3.3 and a weakly-reflective boundary was imposed. A sponge layer of 100 m was applied at the end of the domain to prevent the reflection of outgoing waves that would give rise to instabilities within the numerical domain. The boundary conditions were chosen based on existing overtopping studies, e.g. [2], [5]. For the non-hydrostatic pressure term a Keller-Box scheme with ILU preconditioner was used to increase the stability of the model.

B. Validation

HIDRALERTA was used to generate overtopping discharge and the associated risk levels for three past storms that covered overtopping and no-overtopping events. Four risk levels (no risk, low risk, moderate and high risk) were produced for five coastal receptors (TABLE 1).

TABLE 1. COASTAL RECEPTORS AND OVERTOPPING THRESHOLDS (L/S/M) IN HIDRALERTA ACCORDING TO EACH RISK LEVEL

Risk level	Trained staff	Aware pedestrian	Unaware pedestrian	Vehicles (low speed)	Vehicles (moderate/high speed)
No risk	[<1[	[<0.1[	[<0.01[	[<10[	[<0.01[
Low risk	[1-5[	[0.1-0.5[	[0.01-0.02[	[10-25[	[0.01-0.03[
Moderate risk	[5-10[	[0.5-1[	[0.02-0.03[	[25-50[	[0.03-0.05[
High risk	[≥10[	[≥1[	[≥0.03[	[≥50[	[≥0.05[

The results of HIDRALERTA with the newly implemented SWASH model were compared to the approach currently used in HIDRALERTA, where NN_OVERTOPPING2 is used to compute overtopping discharges. Additionally, both approaches were compared to previously analyzed video images of the breakwater. For that, a video-monitoring system was used and it had been implemented in Ericeira within the To-SEAlert project (Fig. 4 top). As that system had some problems (namely the damage of the video-camera during a storm), the project NAVSAFETY (Fundo Azul program, FA_04_2017_013) has provided some images from another video-monitoring system placed in Ericeira (Fig. 4 bottom). However, this latter system was placed at some distance of the breakwater, making the video images analysis more difficult. As not for every event of this study video images were available, only a total of 46 images were analyzed.
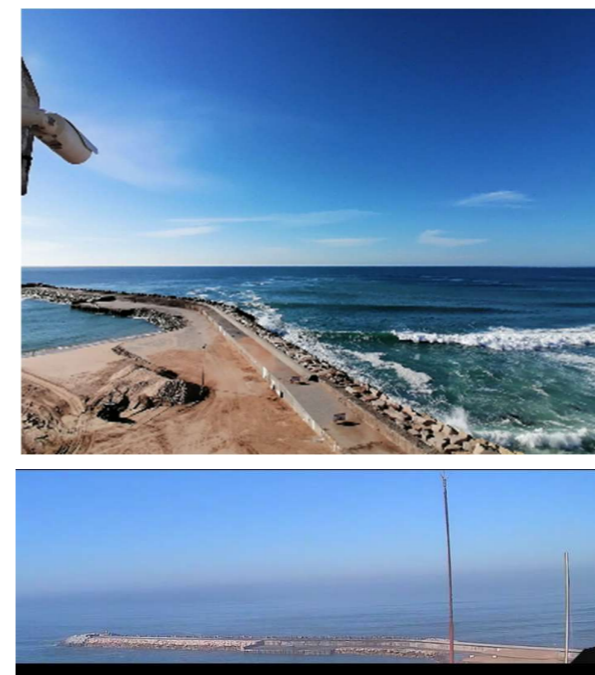

Fig. 4. Video-systems installed in Ericeira: To-SEAlert project (top) and NAVSAFETY project (bottom)

The comparison with the video images was only undertaken for two of the above-mentioned receptors: "Aware pedestrian" and "Vehicles (low speed)". The videos were categorized into the same risk levels as presented in TABLE 1¡**Error! No se encuentra el origen de la referencia.** for these two receptors. For the definition of risk levels, possible impacts of the overtopping occurrences in the video images were analyzed according to TABLE 2.

TABLE 2. RISK LEVEL DEFINITION FOR VIDEO IMAGES BASED ON IMPACTS FOR EACH RECEPTOR

Risk level	Aware pedestrian	Vehicles low speed
No risk	No injuries	Safe to drive
Low risk	Minor injuries	Light motorbikes or bicycles become unstable
Moderate risk	Multiple minor injuries or some serious injuries	Serious damage that affects its use, but without temporary stoppage
High risk	Multiple serious injuries and/or loss of lives	Serious damage that doesn't allow its use

III. RESULTS

The overtopping discharge computed by SWASH and by NN_OVERTOPPING2 in HIDRALERTA showed significant differences (Fig. 5). While the SWASH model performed well at no-overtopping events, which mainly resulted in the same discharge (0 l/s/m), SWASH generally presented higher overtopping values when compared to NN_OVERTOPPING2. The Root-Mean-Square-Error (RMSE) was 5.47 l/s/m, which is a large error considering the average overtopping discharge of the test cases estimated by SWASH was 0.73 l/s/m.
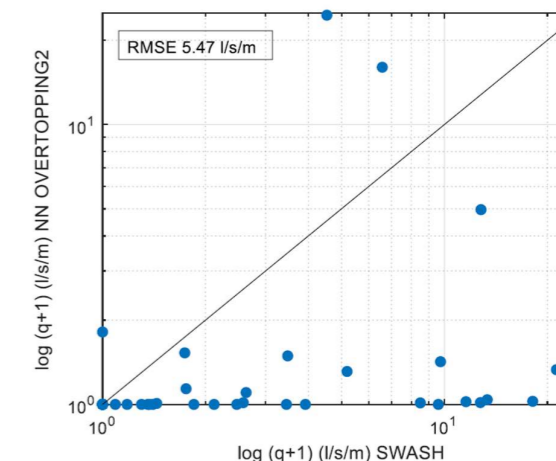
Fig. 5. Comparison of q estimated by HIDRALERTA using SWASH and using NN_OVERTOPPING2

As a consequence, the risk levels generated by HIDRALERTA based on the overtopping discharge resulted in higher alerts when using SWASH than when using NN_OVERTOPPING2. Fig. 6 shows the differences in risk levels computed by HIDRALERTA with SWASH and NN_OVERTOPPING2 for the five receptors. It could be observed that the majority of the cases resulted in the same risk level for all five receptors. This majority included 38 of the 63 total cases which were no-overtopping events.

Once overtopping occurs, however, especially for the receptors with lower thresholds for q, the SWASH simulations resulted in higher risk levels than NN_OVERTOPPING2. For aware pedestrians, the risk level was higher in SWASH in 38% of the cases and a maximum difference of three risk levels was found. For trained staff the thresholds for q are slightly higher than for pedestrians and high speed vehicles, which is why the risk levels are mainly surpassed by one risk level (13%) and only 6% and 8% by two and three risk levels, respectively. For vehicles at low speed, which have high thresholds for q compared to the other receptors, a maximum difference of one risk level was found.

A. Manz, A. C. Zózimo, C. Fortes, L. Pinheiro and J.L. Garzon,
"Implementation of the SWASH model into HIDRALERTA system",
Latin-American Journal of Computing (LAJC), vol. 10, no. 2, 2023.

Fig. 6. Risk levels generated for the five receptors by HIDRALERTA. Comparison between results of SWASH and NN_OVERTOPPING2

The validation with video images revealed an overall better performance of NN_OVERTOPPING2 when compared to video images of the breakwater (Fig. 7). For aware pedestrians and low speed vehicles the neuronal network generates the same risk level for the majority of cases (69% and 92%, respectively). Again, for low speed vehicles, a maximum difference of one risk level was found due to the higher thresholds. SWASH showed good results for vehicles, with 85% of consensus and 4% of one level under- and one or more levels over, respectively. For the lower thresholds of the pedestrians, in 42% of the cases it presents a higher risk level, whereas 46% resulted in the same risk level and 13% were lower by one risk level .

Fig. 7. Risk levels generated for aware pedestrians and slow driving vehicles. Comparison between results of NN_OVERTOPPING2 and video images (top) and SWASH and video images (bottom)

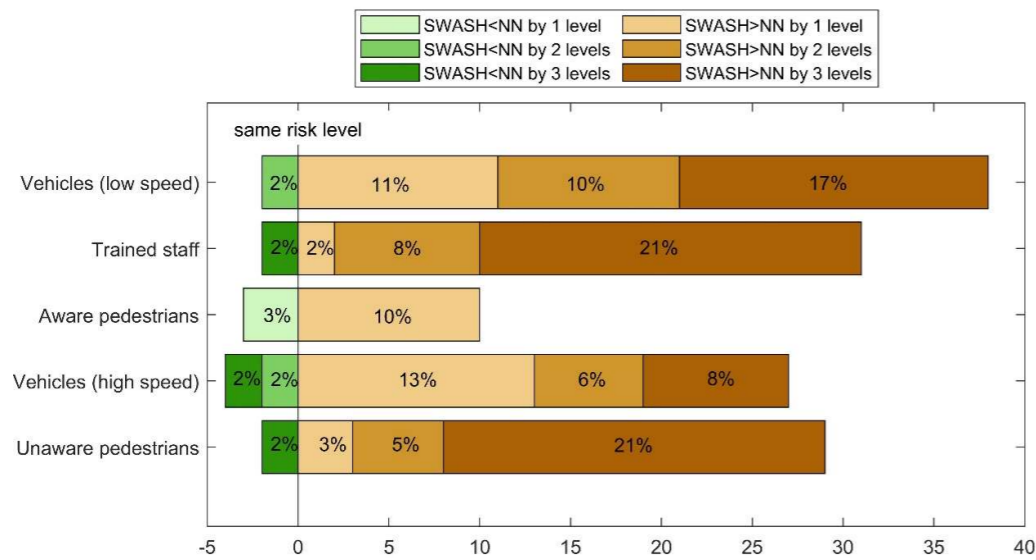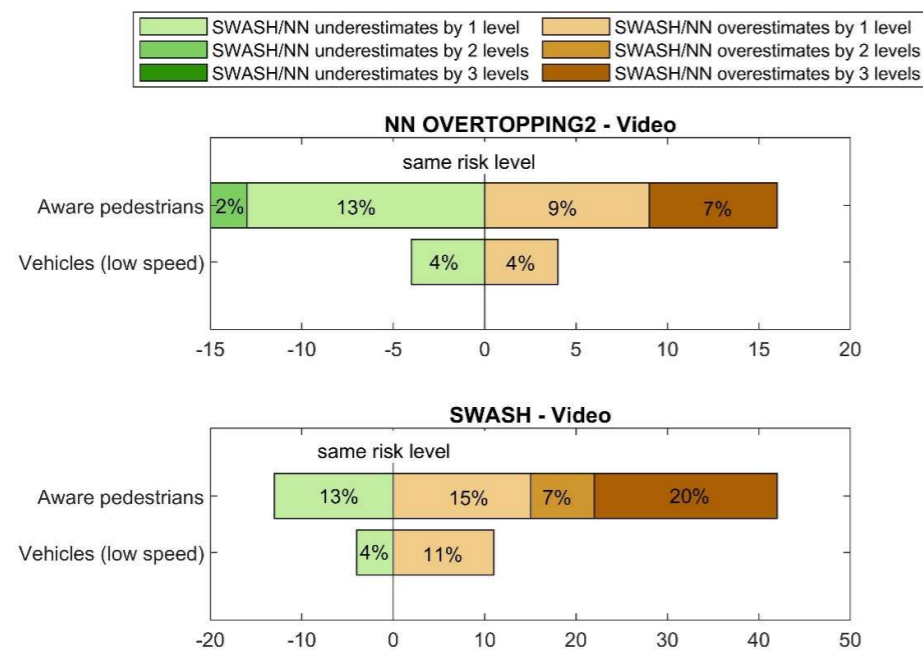There are several factors that may influence the performance of SWASH within HIDRALERTA. While NN_OVERTOPPING2 accounts for wave obliquity, it is not possible to include the wave direction in one-dimensional simulations in SWASH and wave obliquity affects the amount of wave overtopping at a coastal structure, e.g. [20]. More specifically, waves attacking a structure perpendicularly cause higher overtopping discharges than oblique approaching waves. Consequently, SWASH assumed in each case that waves approached the structure normally and the results for q may have been particularly high due to this assumption.

Furthermore, in this first test phase, a constant Manning coefficient for the armour layer of the breakwater was applied for the overtopping simulations of SWASH. Previous studies have shown (e.g. [7], [22]) that the performance of SWASH improves when the Manning coefficient is calibrated for a particular breakwater material and that it is correlated to the dimensionless crest freeboard and wave steepness. In [22], several empirical equations have been developed to define the Manning coefficient based on the wave direction, dimensionless crest freeboard and wave steepness, and the results of the SWASH model could be improved when compared to NN_OVERTOPPING2.

While the neural network NN_OVERTOPPING2 is a commonly used tool to estimate overtopping discharge, it does not reflect real data. Although the video images implied an opportunity to compare the simulated discharges and risk levels against qualitative data, it must be considered that the analysis of the videos and categorization of risk levels is partially subjective and furthermore dependent on the visibility and quality of the material. In general, however, the video validation confirmed what the comparison of the two approaches had shown: an overall overestimation of discharge (and thus, of risk) by the SWASH model.

IV. CONCLUSIONS

This study demonstrated that the implementation of the SWASH model into HIDRALERTA for the chosen profile was successful but did not deliver good results. The results outlined that SWASH computes significantly higher overtopping discharges than NN_OVERTOPPING2, expect in cases of no overtopping, where it mostly agreed with the neuronal network.

It can be concluded that the wave direction, which is not considered in one-dimensional simulations of SWASH, might play a role in causing these discrepancies, as well as the definition of the Manning friction coefficient of the breakwater material and the video analysis. Although delivering qualitative data to assess the performance of the two methods in terms of risk level predictions, the video analysis does not allow for the quantitative assessment of the two methods performance.

Future work will include implementing of the empirical equations developed by [21] for the definition of the Manning friction coefficient, which considers the angle of wave attack and material of the breakwater. The use of 2D SWASH simulation is also a goal to consider the wave direction. However, a set of simulations should be made a priori to obtain in real time the results of overtopping for the HIDDRALERTA system. Also, efforts must be undertaken to develop low-cost methodologies to deliver quantitative overtopping data in prototype conditions.

REFERENCES

[1] C. Altomare, T. Suzuki, X. Chen, T. Verwaest, and A. Kortenhaus, "Wave overtopping of sea dikes with very shallow foreshores," *Coast. Eng.*, vol. 116, pp. 236–257, 2016, doi: https://doi.org/10.1016/j.coastaleng.2016.07.002.

[2] T. Suzuki *et al.*, "Efficient and robust wave overtopping estimation for impermeable coastal structures in shallow foreshores using SWASH," *Coast. Eng.*, vol. 122, pp. 108–123, 2017, doi: https://doi.org/10.1016/j.coastaleng.2017.01.009.

[3] M. Zijlema, G. Stelling, and P. Smit, "SWASH: An operational public domain code for simulating wave fields and rapidly varied flows in coastal waters," *Coast. Eng.*, vol. 58, no. 10, pp. 992–1012, 2011, doi: https://doi.org/10.1016/j.coastaleng.2011.05.015.

[4] T. Suzuki, T. Verwaest, W. Veale, K. Trouw, and M. Zijlema, "A NUMERICAL STUDY ON THE EFFECT OF BEACH NOURISHMENT ON WAVE OVERTOPPING IN SHALLOW FORESHORES," *Coast. Eng. Proc.*, vol. 1, no. 33, Oct. 2012, doi: 10.9753/icce.v33.waves.50.

[5] T. Suzuki, C. Altomare, T. Verwaest, K. Trouw, and M. Zijlema, "TWO-DIMENSIONAL WAVE OVERTOPPING CALCULATION OVER A DIKE IN SHALLOW FORESHORE BY SWASH," *Coast. Eng. Proc.*, vol. 1, no. 34, Oct. 2014, doi: 10.9753/icce.v34.structures.3.

[6] T. Suzuki, C. Altomare, M. Willems, and S. Dan, "Non-Hydrostatic Modelling of Coastal Flooding in Port Environments," *Journal of Marine Science and Engineering*, vol. 11, no. 3. 2023. doi: 10.3390/jmse11030575.

[7] N. Zhang *et al.*, "Numerical Simulation of Wave Overtopping on Breakwater with an Armor Layer of Accropode Using SWASH Model," *Water*, vol. 12, no. 2, 2020, doi: 10.3390/w12020386.

[8] D. F. A. Vanneste, C. Altomare, T. Suzuki, P. Troch, and T. Verwaest, "COMPARISON OF NUMERICAL MODELS FOR WAVE OVERTOPPING AND IMPACT ON A SEA WALL," *Coast. Eng. Proc.*, vol. 1, no. 34, p. structures.5, Oct. 2014, doi: 10.9753/icce.v34.structures.5.

[9] V. Gracia *et al.*, "A NEW GENERATION OF EARLY WARNING SYSTEMS FOR COASTAL RISK. THE ICOAST PROJECT," *Coast. Eng. Proc.*, vol. 1, no. 34, p. management.18, Oct. 2014, doi: 10.9753/icce.v34.management.18.

[10] A. van Dongeren *et al.*, "Introduction to RISC-KIT: Resilience-increasing strategies for coasts," *Coast. Eng.*, vol. 134, pp. 2–9, 2018, doi: https://doi.org/10.1016/j.coastaleng.2017.10.007.

[11] C. J. E. M. Fortes *et al.*, "The HIDRALERTA system: Application to the ports of Madalena do Pico and S. Roque do Pico, Azores," *Aquat. Ecosyst. Health Manag.*, vol. 23, no. 4, pp. 398–406, Oct. 2020, doi: 10.1080/14634988.2020.1807295.

[12] L. Pinheiro, C. J. E. M. Fortes, M. T. Reis, J. Santos, and C. G. Soares, "Risk Forecast System for Moored Ships," Oct. 2020.

[13] P. Poseiro, "Forecast and Early Warning System for Wave Overtopping and Flooding in Coastal and Harbour Areas: Development of a Model and Risk Assessment," IST-UNL, Lisbon, 2019.

[14] M. I. Santos *et al.*, "Simulation of hurricane Lorenzo at the port of Madalena do Pico, Azores, by using the HIDRALERTA system," in *Developments in Maritime Technology and Engineering*, Lisbon: MARTECH 5th International Conference on Maritime Technology and Engineering, 2021, pp. 815–823. doi: 10.1201/9781003216599-89.

[15] A. C. Zózimo, A. M. Ferreira, L. Pinheiro, C. J. E. . Fortes, and M. Baliko, "Implementação do sistema HIDRALERTA para a zona costeira da Costa da Caparica," 2021.

[16] Swan Team, *Swan User Manual*, 40.51. Department of Civil Engineering and Geosciences, Delft university of Technology, Delft, The Netherlands, 2006.

[17] C. J. E. . Fortes, "Transformações não-lineares de ondas marítimas em zonas portuárias. Análise pelo método dos Elementos Finitos.," 2002.

[18] D. Flater, *Xtide*. 2021.

[19] E. M. Coeveld, M. R. A. Van Gent, and B. Pozueta, "Neural network manual for NN_Overtopping program," 2005.

[20] EurOtop, *Manual on wave overtopping of sea defences and related structures. An overtopping manual largely based on European research, but for worldwide application.* 2018.

[21] A. Manz, "Application of SWASH to determine overtopping during storm events in the port of Ericeira and its introduction into HIDRALERTA system," Universidade do Algarve, 2021.

[22] A. Manz, A. Zózimo, and J. L. Garzon, "Application of SWASH to Compute Wave Overtopping in Ericeira Harbour for Operational Purposes," *J. Mar. Sci. Eng.*, vol. 10, p. 1881, Dec. 2022, doi: 10.3390/jmse10121881.

AUTHORS

Anika Manz

Anika Manz is an early-career Marine Scientist with multidisciplinary background in Marine/Environmental Sciences and Communication. Her research activities have a focus on coastal risk assessment, numerical modeling and coastal flooding prediction systems. Currently, is particularly interested in climate adaptation technologies and disaster risk management in a coastal context. She holds a Bachelor's degree in Technical Journalism and Environmental Sciences and a Master's degree in Marine and Coastal Systems from the University of Algarve, Portugal. During her dissertation she worked on the To-SEAlert project (Ref. PTDC/EAMOCE/31207/2017), where she applied a numerical model in order to estimate wave overtopping at the harbour of Ericeira. After graduation, she received a FCT research fellowship for the EW-Coast project (Ref. ALGLISBOA-01-145-FEDER-028657) at the National Laboratory of Civil Engineering in Lisbon (LNEC), where she worked until recently on the implementation of an early warning system for coastal risks induced by storms. Her work was presented at several national and international conferences and published in research articles in several journals.

Ana Catarina Zózimo

Ana Catarina Zózimo is a Post-Doctoral researcher at the Portuguese National Laboratory for Civil Engineering and she is presently involved in two European Projects: C2IMPRESS and LIFE GARACHICO, both related to risks in coastal areas and ports. Her research has been focused on the processes acting on coastal areas, with a focus on maritime hydraulics and Geographical Information Systems. At present she is highly focused on wave-induced risks, and on developing early warning systems to enable authorities to act in advance and protect people and properties. She has already participated in the development of applications to research projects that involved teams from several institutions, in the organization of scientific meetings, fieldwork, and physical model tests. Between 2010 and 2018 she worked in the private sector in the areas of numerical modeling for detailed design projects. During her passage in the private sector, she obtained a wide experience in the coordination of projects and teams, liaison with clients, on the development of soft coastal protection works, and in the environmental impact assessment aspects of those projects.

Conceição Fortes

Conceição Fortes is Principal Investigator and Head of the Nucleus of Ports and Maritime Structures (NPE) Department of Hydraulics and Environment (DHA) of the National Laboratory of Civil Engineering (LNEC) in Portugal. She holds a PhD in Mechanical Engineering from Instituto Superior Técnico (University of Lisbon). She has carried out research in the field of coastal and port engineering, numerical and physical modeling of the propagation of sea waves in coastal and port areas, forecasting and warning systems for sea waves, overtopping, flooding and navigation in coastal and port areas and in inspection and analysis of the behavior of marine structures. She participated in 48 programmed research projects and 53 contract studies, promoted by national and international entities. Additionally, she participated in the organization of 16 national and international conferences and has been responsible for 15 training courses, teaching various modules. She also has experience in the supervision of more than 100 undergraduate; master's degrees and PhD students and postdoc researchers.

Liliana Pinheiro

Liliana Pinheiro is Assistant Researcher at the Ports and Maritime Structures unit (NPE) of the Hydraulics and Environment Department (DHA) of the National Laboratory of Civil Engineering (LNEC). She holds a PhD in Mechanical Engineering from Instituto Superior Técnico (University of Lisbon). She has carried out research in the fields of coastal and port engineering, namely using numerical and physical modelling for studies involving wave propagation, wave characterization; resonance; shelter and operability of port terminals; impact assessment of the construction of port infrastructures, moored ships, floating structures, stability and over-topping of coastal structures. She also participated in various field measurement campaigns. Her main interests are CFD modelling, numerical techniques, ship safety and port infrastructures management.

AUTHORS

Juan Luis Garzon

Juan Luis Garzon Hervas is an experienced post-doctoral researcher who works in the areas of Natural sciences with emphasis on Oceanography, Engineering and Technology. He completed his Doctor in 2018/05 at the George Mason University Volgenau School of Information Technology and Engineering. He not only has extensive knowledge in coastal risk studies and coastal dynamics, but is also, due to his background in civil engineering, highly proficient in the use of numerical models like XBEACH, ADCIRC, DELFT3D, MIKE21, SWAN, SWASH and Surface-water Modeling System (SMS), HEC-RAS, OPTIMOOR and High-Performance Computer environments.. He is furthermore skilled in Geographical Information Systems such as ArcGIS and Google Earth Engine. His scientific production accounts for 30 publications and 19 presentations in national and international conferences. Additionally, he is scientific advisor of the Colab +Atlantic partner for the modeling aspects of the EOatSEE project. He also has experience in the supervision of master and PhD students.

The Stiffness Phenomena for the Epidemiological SIR Model: a Numerical Approach

Marline Ilha da Silva
Federal Institute of Education of Rio Grande do Sul
Porto Alegre, Brazil
marline.ilhadasilva@gmail.com
ORCID: 0000-0002-0236-1227

Joice Chaves Marques
Inst. of Mathematics, Statistics and Physics
Federal Univ. of Rio Grande
Rio Grande, Brazil
joicec.marques@hotmail.com
ORCID: 0000-0003-2137-2164

Adelaida Otazu Conza
Faculty of Mathematical Physics
National University of the Altiplano
Puno, Peru
aotazu@unap.edu.pe
ORCID: 0000-0003-4793-0400

Adriano De Cezaro
Inst. of Mathematics, Statistics and Physics
Federal Univ. of Rio Grande
Rio Grande, Brazil
decezaromtm@gmail.com
ORCID: 0000-0001-8431-9120

Ana Carla Ferreira Nicola Gomes
Inst. of Mathematics, Statistics and Physics
Federal Univ. of Rio Grande
Rio Grande, Brazil
anagomes.mat@gmail.com
ORCID: 0000-0003-2815-1612

M. da Silva, J. Chaves Marques, A. Otazu Conza ,A. De Cezaro, and A. Ferreira Nicola Gomes
"The Stiffness Phenomena for the Epidemiological SIR Model: a Numerical Approach",
Latin-American Journal of Computing (LAJC), vol. 10, no. 2, 2023.

The Stiffness Phenomena for the Epidemiological SIR Model: a Numerical Approach

Marline Ilha da Silva
Federal Institute of Education of Rio Grande do Sul
Porto Alegre, Brazil
marline.ilhadasilva@gmail.com
ORCID: 0000-0002-0236-1227

Joice Chaves Marques
Inst. of Mathematics, Statistics and Physics Federal Univ. of Rio Grande
Rio Grande, Brazil
joicec.marques@hotmail.com
ORCID: 0000-0003-2137-2164

Adelaida Otazu Conza
Faculty of Mathematical Physics National University of the Altiplano
Puno, Peru
aotazu@unap.edu.pe
ORCID: 0000-0003-4793-0400

Adriano De Cezaro
Inst. of Mathematics, Statistics and Physics Federal Univ. of Rio Grande
Rio Grande, Brazil
decezaromtm@gmail.com
ORCID: 0000-0001-8431-9120

Ana Carla Ferreira Nicola Gomes
Inst. of Mathematics, Statistics and Physics Federal Univ. of Rio Grande
Rio Grande, Brazil
anagomes.mat@gmail.com
ORCID: 0000-0003-2815-1612

Abstract—Mathematical models are among the most successful strategies for predicting the dynamics of a disease spreading in a population. Among them, the so-called compartmental models, where the total population is proportionally divided into compartments, are widely used. The SIR model (Susceptible-Infected-Recovered) is one of them, where the dynamics between the compartments follows a system of nonlinear differential equations. As a result of the non-linearity of the dynamics, it has no analytical solution. Therefore, some numerical methods must be used to obtain an approximate solution. In this contribution, we present simulated scenarios for the SIR model showing its stiffness, a phenomenon that implies the necessity of a small step size choice in the numerical approximation. The numerical results show that the stiffness phenomenon increases with higher transmission rates β and lower birth and mortality rates μ. We compare the numerical solutions and errors for the SIR model using explicit Euler, Runge Kutta, and the semi-implicit Rosenbrock methods and analyze the numerical implications of the stiffness on them. We conclude that any accurate numerical solution of the SIR model will depend on an appropriately chosen numerical method and the time step, in terms of the values of the parameters β, μ.

Keywords— *Stiffness, SIR model, Numerical Methods*

I. INTRODUCTION

Since the pioneering work of Bernoulli [1], mathematical models have proved to be a fundamental tool for predicting the dynamics of infectious diseases. In particular, the recent changes in the UK's strategies regarding the COVID-19 pandemic [2] strongly collaborate to reaffirm such a claim. It turns out that an enormous number of mathematical models and simulating scenarios were recently proposed and analyzed for the COVID-19 outbreak, making it hard to attempt a complete literature overview. Nevertheless, at the heart of many of these proposed models are SIR-like compartmental models, originally proposed by Kermack & Mckendrick [3]. In other words, unless some compartment clustering (summarizing individuals in distinct compartments) is used, such proposed models assume that at any time $t \geq 0$ of the underlying diseases, the total population

$N(t) = S(t) + I(t) + R(t)$ is divided into compartments of susceptible $S(t)$, infected or infectious $I(t)$ and recovered or removed $R(t)$. Using the law of mass action, Kermack & Mckendrick [3] concludes that the diseases must follow the SIR nonlinear dynamics:

$$S'(t) = -\beta S(t) I(t) + \mu(N(t) - S(t))$$
$$I'(t) = \beta S(t) I(t) - (\gamma + \mu) I(t)$$
$$R'(t) = \gamma I(t) - \mu R(t), \qquad (1)$$

where $' := \frac{d}{dt}$, β is a disease transmission rate, μ is birth and mortality rates (that for simplicity we assume to be the same), γ is the inverse of the mean infectious period. We assume that all the parameters are time-independent.

In the dynamics (1), the following initial conditions are considered (IC)

$$S(0) = 1 - I(0), I(0) \geq 0, R(0) = 0, \qquad (2)$$

characterizing the model as initial value problems (IVP) for nonlinear systems of ordinary differential equations (ODE's).

Given the non-linearity, SIR model (1) - (2) does not have an explicit solution. As a result, any attempt to predict disease dynamics must be obtained from some approximation of the solution provided by numerical methods [4]. This necessity of using numerical methods drives the main question of this contribution: Are there some parameter choice scenarios that characterizes the SIR model to be stiff?

The phenomenon of stiffness in a (IVP) means that the numerical solutions are unstable and/or its accuracy is largely affected using any explicit numerical methods. It imposes the need for a very small time step to approximate the solution and, consequently, becomes computationally expensive.

In Section II, we revisit some well-known properties of the solution of the (IVP) of the SIR model. Such properties

will help to justify the numerical analysis that follows. In Section III, we present a definition of stiffness. Moreover, we present and compare the obtained results for distinct scenarios of parameter choices for the model. In Section IV, we show the consequences of the stiffness phenomena in the numerical solution of the SIR model using explicit and implicit numerical approximations. The main contribution of this manuscript is the conclusion that the SIR model is indeed stiff, for large transmission rates β. The analysis of the error in the numerical solutions allows us to recommend the use of appropriate numerical methods as well as the time-step size. In Section V, we formulate the final conclusions.

II. SOME SIR MODEL PROPERTIES

In this section, we revisit some of the well-known SIR model properties reformulated from [5], that will be used to justify the numerical analysis that follows.

Theorem 1. Let the assumptions for the SIR model (1) with initial conditions (2) hold true. Then, the (IVP) (1) - (2) corresponding to the SIR model have a unique differentiable solution $Y(t) = (S(t), I(t), R(t))^T$. Since the initial conditions (2) for are non-negative, each of the coordinates of the solution $Y(t)$ remains non-negative for all $t \geq 0$.

Note that, summing all the equations in models (1), we conclude that the total population is constant. To keep things simple, we will assume that N is normalized so that $N(t) = 1$, for all $t \geq 0$. It follows from the first equation in that $S(t)$ is decreasing. Furthermore, we get from Theorem 1 that

$$S^\infty := \lim_{t \to \infty} S(t) \geq 0 \qquad (3)$$

As we will see in Section IV, the stiffness phenomena present in the SIR model imply that numerical solutions obtained from an explicit numerical scheme might not satisfy Theorem 1 and equation (3) in particular.

III. NUMERICAL METHODS AND STIFFNESS PHENOMENA FOR SIR MODEL

Let $Y(t)$ be the unique solution of the SIR model (1) - (2) as shown in Theorem 1, whose coordinates will be denoted by $Y^i(t)$, for $i = 1,2,3$ respectively. According to [4], the step of a numerical method to obtain the approximation Y_n^i for the exact solution $Y^i(t_n)$ of the (IVP), for $t_n \in [0, T]$, can be written, in general, as follows

$$\sum_{j=0}^{k} \alpha_j Y_{n-j}^i = h_n \psi_F(h_n, t_n, \cdots, t_{n-k}, Y_n^i, \cdots, Y_{n-k}^i),$$

where $k \geq 1$ is the number of preview steps used to compute Y_n^i. The values α_j, for $j = 0, \cdots, k$ are numerical method-specific constants, h_n is the method step-size. The

function ψ_F is defined in terms of evaluating the right-hand side $F(t, Y(t))$ of the system of differential equations (1).

In general terms, we can classify the numerical methods as: Single-step if $k = 1$, or multi-step if $k > 1$. Linear if ψ_F is linear in the evaluation of $F(t, Y(t))$ and non-linear otherwise. Implicit if ψ_F depends on Y_n and explicit otherwise.

In the numerical simulations for the SIR model (1) - (2) that follows, we will adopt the following methods: A) the explicit, single-step Euler method; B) the explicit, single-step Runge-Kutta method; C) the semi-implicit, fourth order, four-stage Rosenbrock method, e.g, [4].

A. The stiffness phenomena

The phenomena of stiffness in solving (IVP) appeared at the beginning of the 20th century. It was [6] one of the first to notice some implicit numerical methods perform better than explicit ones for stiff (IVP). This is because the implicit methods have an unlimited stability region that covers the entire half-plane complex with a negative real part or at least an unlimited part of it, e.g. [4].

A well-accepted definition of the phenomena of stiffness follows:

Definition 1. Let $\lambda_j(t) \in \mathbb{C}$, for $j = 1, \cdots, n$ the eigenvalues of the Jacobian matrix $J(F(t, Y(t)))$, where $F(t, Y(t))$ is the right-hand side of the (IVP).

The (IVP) is called stiff in some interval I of the real line if $Re(\lambda_j(t)) < 0$ for all $j = 1, \cdots, n$ and stiffness ratio

$$\xi := \frac{\max_j |Re(\lambda_j(t))|}{\min_j |Re(\lambda_j(t))|} \gg 1, \ \forall \, t \in I$$

If the (IVP) is stiff, then certain numerical methods for solving the equation become numerically unstable unless the step size is taken to be extremely small. This is the case for most explicit numerical schemes. See [4] for some examples.

B. The stiffness phenomena for SIR model

The Jacobian matrix for model (1) for an arbitrary point is given by

$$J(S(t), I(t), R(t)) = \begin{pmatrix} -(\mu + \beta I(t)) & -\beta S(t) & 0 \\ \beta I(t) & -(\gamma + \mu) + \beta S(t) & 0 \\ 0 & \gamma & -\mu \end{pmatrix}.$$

Then, the eigenvalues λ_j, $j = 1, 2, 3$ of the Jacobian matrix are given by:
$$\lambda_1 = -\mu$$
$$\lambda_2(t) = -\frac{1}{2} \times [[(\mu + \beta) + (\gamma + \mu) - \beta S(t)] + \sqrt{[(\mu + \beta I(t)) - (\gamma + \mu - \beta S(t))]^2 - 4\beta^2 S(t) I(t)}]$$
$$\lambda_3(t) = -\frac{1}{2} \times [[(\mu + \beta I(t)) + (\gamma + \mu) - \beta S(t)] - \sqrt{[(\mu + \beta I(t)) - (\gamma + \mu - \beta S(t))]^2 - 4\beta^2 S(t) I(t)}]$$

Below, the stiffness ratio for the (IVP) SIR model (1) - (2) is numerically investigated. Table I displays various

LATIN-AMERICAN JOURNAL OF COMPUTING (LAJC), Vol X, Issue 2, July 2023

M. da Silva, J. Chaves Marques, A. Otazu Conza ,A. De Cezaro, and A. Ferreira Nicola Gomes
"The Stiffness Phenomena for the Epidemiological SIR Model: a Numerical Approach",
Latin-American Journal of Computing (LAJC), vol. 10, no. 2, 2023.

values of the stiffness ratio ξ (see Definition 1) as a function of β and μ. The numerical results presented in Table I suggest that the SIR model's rigidity becomes increasingly greater as we increase the β and/or decrease the μ.

TABLE I. STIFFNESS RATIO ξ FOR SIR MODEL, AS A FUNCTION OF β AND μ.

β	μ=0.01	μ=0.001	μ=0.0001
0.5	ξ=12	ξ=131	ξ=1354
1.5	ξ=39	ξ=392	ξ=3923
10	ξ=808	ξ=8090	ξ=80908
12	ξ=986	ξ=9870	ξ=98708
18	ξ=1442	ξ=14430	ξ=144308
25	ξ=1766	ξ=17666	ξ=176668

Before delving into the effect of the stiffness ratio on numerical simulations of the SIR model (1), we should consider the epidemiological implications of the parameters μ and β as shown in Table I.

Remark 1. Small values of μ mean that the birth and mortality rates are very low, in proportion to the total population, during the disease duration. It is a typical effect for a short time simulation. Large values of the transmission rate β have a more debatable epidemiological meaning. However, there are highly contagious diseases such as measles, pertussis, and tuberculosis that are already documented in the literature [7, 8]. Furthermore, many diseases transmission depends on population density (high for high-density populations) and environment (for example, for respiratory transmitted diseases, a crowded and closed environment implies higher transmission rates) [9]. To put it another way, a disease that has not yet been reported may have a higher transmission rate than those already reported.

IV. NUMERICAL RESULTS

In this section, we present numerical simulated results and show the implications of the stiffness ratio (see the stiff ration in Table I on the numerical approximated solutions for the SIR model. We present the simulations using e explicit Euler method, the two-stage and second-order Runge-Kutta method (RK22), the four-stage and fourth-order Runge-Kutta method (RK44) and Rosenbrock method [4]. In the simulation, the step-size $h = 0.1$ is used for all the methods except for the Rosenbrock method, for which the adaptive step-size is used [4]. The initial conditions $S_0 = 0.9$, $I_0 = 0.1$ and $R_0 = 0$ are used and the parameter $\gamma = 0.35$ is kept fixed. The above mentioned methods are implemented in *Fortran 90* with a double precision, GNU Fortran Compiler (Ubuntu 18.04.5 LTS operational system 64 bits) and running in a processor Intel® Core(TM)i5 − $5200U$ CPU@2.20GHz × 4.

(a) Simulated scenarios using the Euler method.

(b) Simulated scenarios using the RK22 method.

(c) Simulated scenarios using the RK44 method.

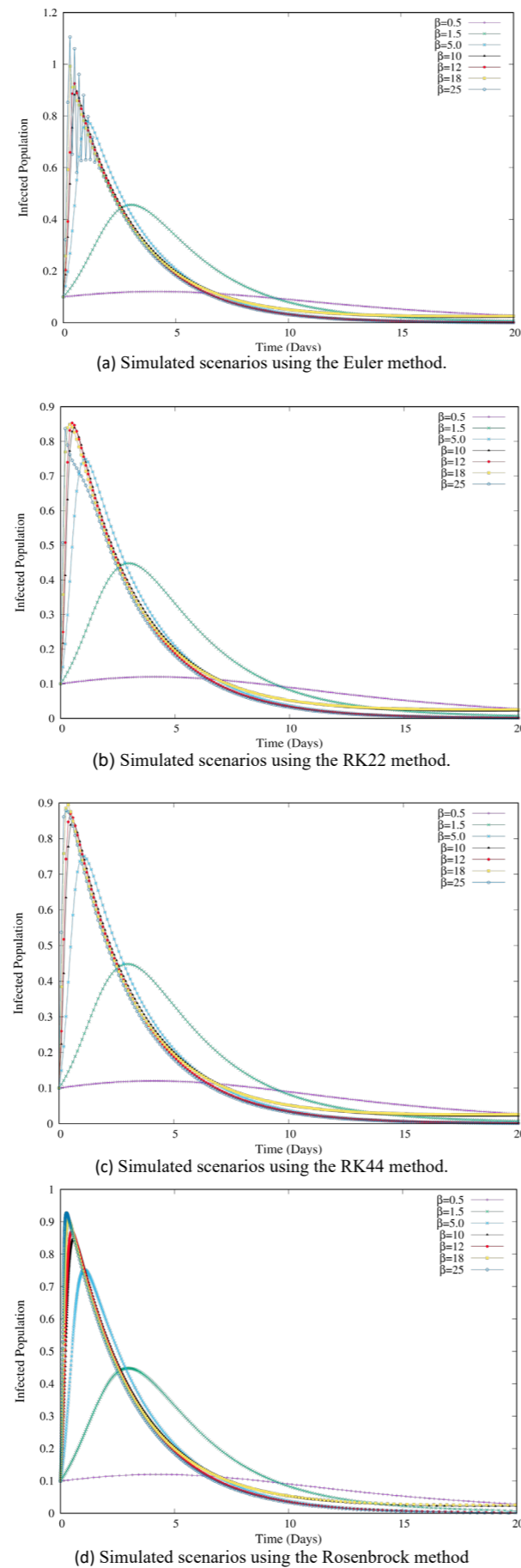(d) Simulated scenarios using the Rosenbrock method

Fig. 1. Simulated scenarios for the infected populations $I(t)$.

In Fig. 1, we show the simulated scenarios of the infected population, for choices of $\mu = 0.001$ and values of β=0.5, 1.5, 5.0, 10, 12, 18, 25, respectively. In the simulation with the Rosenbrock method, the adaptive step-size, typically of the method, is used. The simulations for the remaining methods use the step-size $h = 0.1$.

For the simulated scenario with $\beta = 25$, the first and most obvious consequences of the stiffness phenomenon can be seen. In this particular scenario, the approximate solution using the Euler method oscillates as shown in Fig. 1(a). The oscillations disappear in the numerical solutions using the RK22, RK44 and Rosenbrock methods, as can be observed in Fig. 1(b), Fig. 1(c) and Fig. 1(d).

(a) Susceptible population $S(t)$.

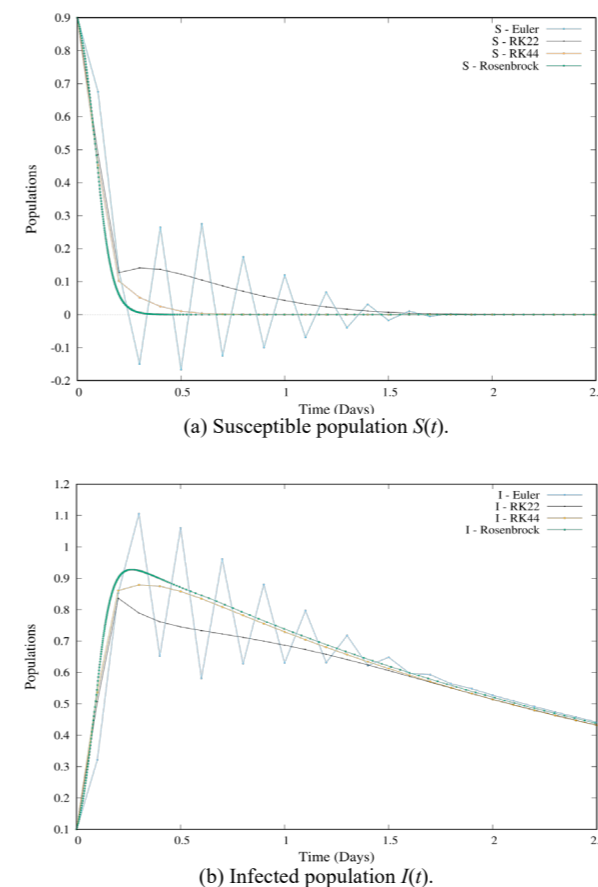(b) Infected population $I(t)$.

Fig. 2. Simulated scenarios using the numerical methods for $\beta = 25$.

A zoom on the numerically simulated scenario for $\beta = 25$ of the susceptible and infected is depicted in Fig. 2 (a) and Fig. 2(b), respectively, using all the numerical methods under investigation. It turns out that the oscillations of the numerical solutions obtained by the explicit Euler method produce negative values for the susceptible (see Fig. 2 (a)) and values larger than 1 for the infected population (see Fig. 2 (b)), which contradicts Theorem 1. Moreover, the simulated scenarios using the RK22 and RK44 methods present non-smooth solutions and hence also contradict Theorem 1. It can be observed in the simulated results that only the Rosenbrock method, the method designed for stiff problems [4], presents an approximate solution that satisfies Theorem 1.

The remaining question addressed in this contribution is whether the stiffness phenomenon for the SIR model appears only for very large β. The simulated solution for the susceptible and infected population, with the choice of $\beta = 12$, is depicted in Fig. 3(a) and Fig. 3(b), using the Euler method with step-size $h = 0.1$ and the Rosenbrock method with adaptive step-size. It can seem that the numerical solution using the Euler method is not smooth near the peak of the infection and negative values for the susceptible are obtained (observe the zoom in Fig. 3(a)), contradicting Theorem 1. The numerical solution using the Rosenbrock method demonstrates the adaptation of the step size near the infection peak is much smaller than $h = 0.1$ (see Fig. 3(a)).

(a) Susceptible population.

(b) Infected population.
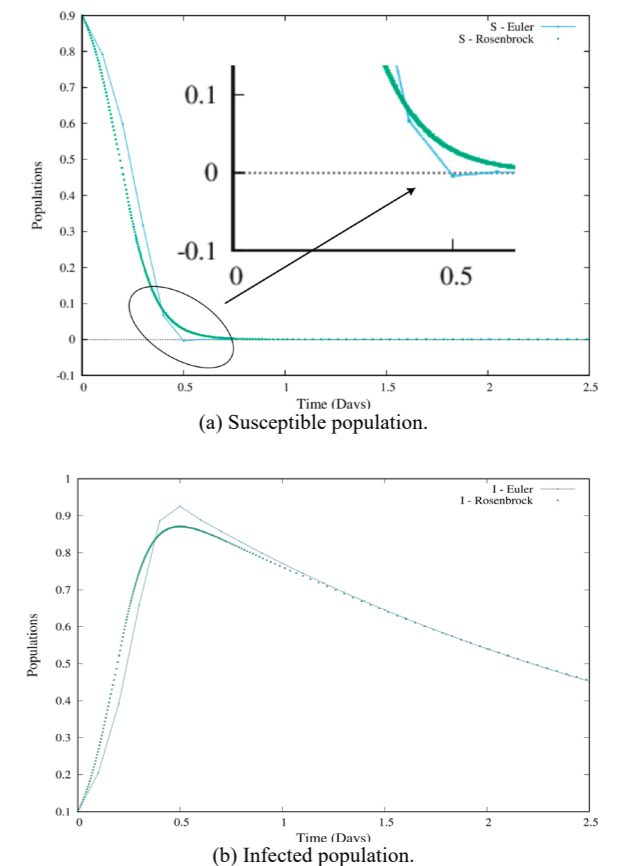
Fig. 3. Simulated scenarios using the numerical methods of Euler and Rosenbrock for $\beta = 12$.

In Fig. 4(a), we show the values for the step-sizes used by the Rosenbrock method with adaptive step for the simulated scenarios with $\beta = 12$. It is worth mentioning that a small step-size is needed in the regions close to the peak of infection; that coincides with the region of the large discrepancies between the two methods presented in (see Fig. 3). In Fig. 4(b), we depicted the numerical solutions for the susceptible and infected populations using the Euler and Rosenbrock methods with the smallest step-size $h = 0.0027$ adopted by the Rosenbrock method. As a result of using a very small step-size, the Euler method shows a more accurate numerical solution. Indeed, it is a consequence of the stiffness of the SIR model.

M. da Silva, J. Chaves Marques, A. Otazu Conza ,A. De Cezaro, and A. Ferreira Nicola Gomes
"The Stiffness Phenomena for the Epidemiological SIR Model: a Numerical Approach",
Latin-American Journal of Computing (LAJC), vol. 10, no. 2, 2023.
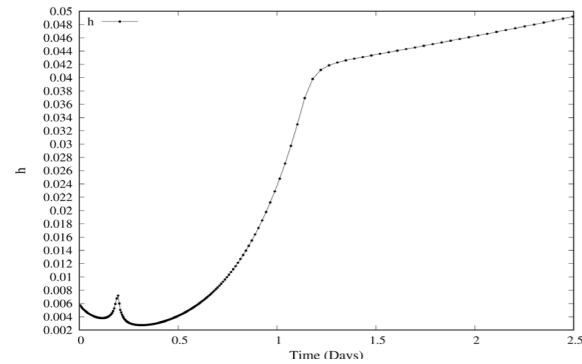
(a) Adaptive step-size h used by the Rosenbrock method.
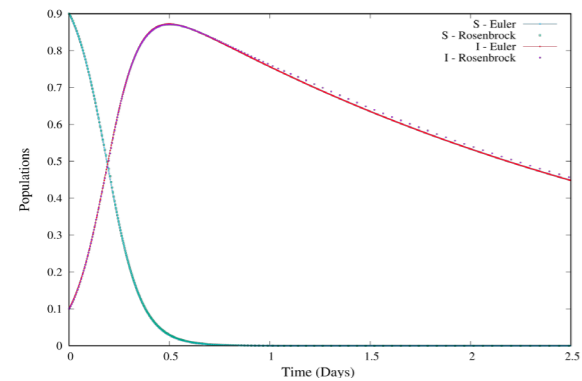
(b) Numerical solutions obtained for of $S(t)$ and $I(t)$ by the Euler and Rosenbrock methods using the step-size $h = 0.0027$ for $\beta = 12$.

Fig. 4. h variable (a); Simulated solutions of $S(t)$ and $I(t)$ using the Euler method with $h = 0.0027$ and Rosenbrock method (b).

Table II and Table III show the difference in the maximum and quadratic norm of the simulated infected population using the methods discussed in this contribution for different scenarios of β.

The difference between the numerical solutions of the infected population using the Euler and Rosenbrock methods with step-size $h = 0.1$ is depicted in Fig. 5 for some scenarios of choice for β. The absolute value of the difference is monotonically increases with β, as shown in the second column of Table II. The difference is approximately 10% in absolute value for $\beta = 10$, 20% in absolute values for $\beta = 18$, and 40% in absolute values for $\beta = 25$.

The difference between the numerical solutions of the infected population using the RK44 and Rosenbrock methods with step-size $h = 0.1$ is depicted in Fig. 6 for some scenarios of choices of β. As it can be seen from the results in the fourth column of Table II, the difference is significant only for $\beta = 25$ (see also Fig. 5(d)).

Based on the results in Fig. 5, Fig. 6 and the one in the Table II and Table III, we can conclude that as the stiffness of the SIR model increases (as β increases), the absolute difference between the Euler or RK44 and Rosenbrock methods becomes concentrated near the infection's peak. The results show that the stiffness of the SIR model suggests using a small numerical step-size or a method designed for solving stiff problems, such as the Rosenbrock method.

TABLE II. ABSOLUTE DIFFERENCE IN THE MAXIMUM NORM (E_∞), OBTAINED BY COMPARE THE NUMERICAL SOLUTION OF THE INFECTED POPULATIONS USING EULER, RK22, RK44 AND ROSENBROCK WITH STEP-SIZE $h = 0.1$ FOR DISTINCT SCENARIOS OF CHOICES OF β, WHERE $E_\infty = \max\limits_{1 \leq i \leq n_p} (|e_i|)$, e_i IS THE DIFFERENCE BETWEEN THE NUMERICAL SOLUTION OBTAINED WITH TWO METHODS AND n_p IS THE NUMBER OF MESH POINTS.

β	EUL-RK44	ROSEN-EUL	ROSEN-RK22	ROSEN-RK44
0.5	6.31629999E-004	6.32139999E-004	3.10000000E-006	8.40000000E-007
1.5	9.31865999E-003	9.37654999E-003	6.65800000E-005	8.13800000E-005
5.0	4.31432800E-002	4.45318200E-002	3.14857000E-003	1.53705999E-003
10	9.75375600E-002	0.1046652200000	1.60849599E-002	7.12765999E-003
12	0.1254940800000	0.1386138800000	2.24853200E-002	1.31198000E-002
18	0.1652883499999	0.1921446000000	6.42736900E-002	3.78952900E-002
25	0.25355632000	0.3798633000000	0.1938273099999	0.16452352999999

TABLE III. DIFFERENCE IN THE QUADRATIC NORM (E_2) OBTAINED BY COMPARE THE NUMERICAL SOLUTION OF THE INFECTED POPULATIONS USING EULER, RK22, RK44 AND ROSENBROCK WITH STEP-SIZE $h = 0.1$ FOR DISTINCT SCENARIOS OF CHOICES OF β, WHERE $E_2 = \sqrt{\sum_{i=1}^{n_p}(e_i)^2}$, e_i IS THE DIFFERENCE BETWEEN THE NUMERICAL SOLUTION OBTAINED WITH TWO METHODS AND n_p IS THE NUMBER OF MESH POINTS.

B	EUL-RK44	ROSEN-EUL	ROSEN-RK22	ROSEN-RK44
0.5	5.19327356E-003	5.19632985E-003	2.62110358E-005	7.58340293E-006
1.5	4.56074598E-002	4.58760091E-002	3.41815002E-004	4.92608905E-004
5.0	0.1091601723987	0.1142371665391	9.29380985E-003	7.36393037E-003
10	0.1660532290951	0.1817178386566	3.18795925E-002	2.08116287E-002
12	0.1850148159726	0.2059415688449	4.37253865E-002	2.66299399E-002
18	0.2434880862085	0.2855538441138	0.1073111915718	5.60055913E-002
25	0.5861619984467	0.6758640423753	0.3019573642769	0.2053197286638

(a) β = 0.5

(c) β = 18

(b) β = 1.5

(d) β = 25

Fig. 5. Difference between the numerical solution of the infected population using Euler and Rosenbrock methods with step-size $h = 0.1$. Simulated scenarios with distinct choices of β.
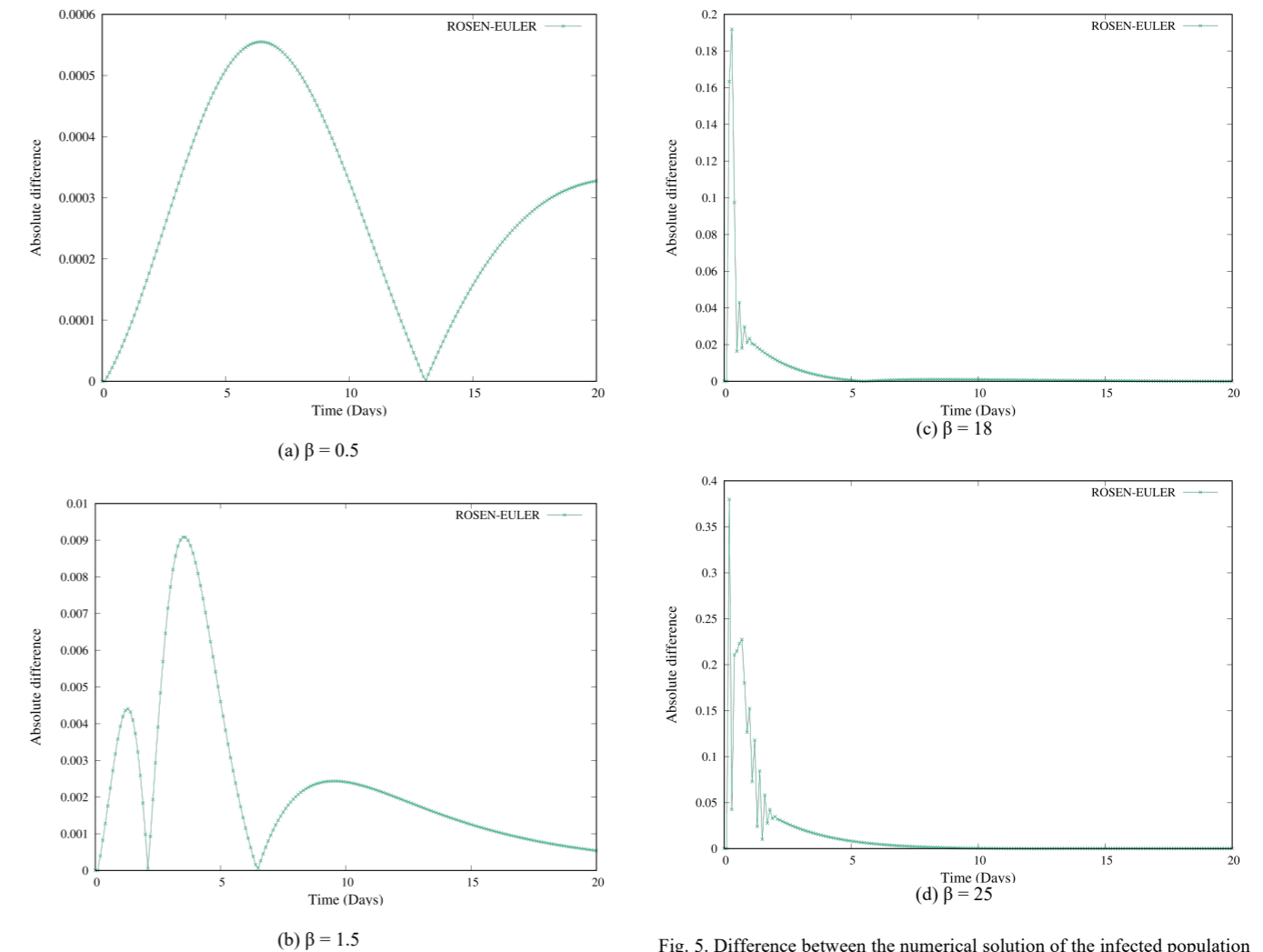
(a) β = 0.5

(b) β = 1.5
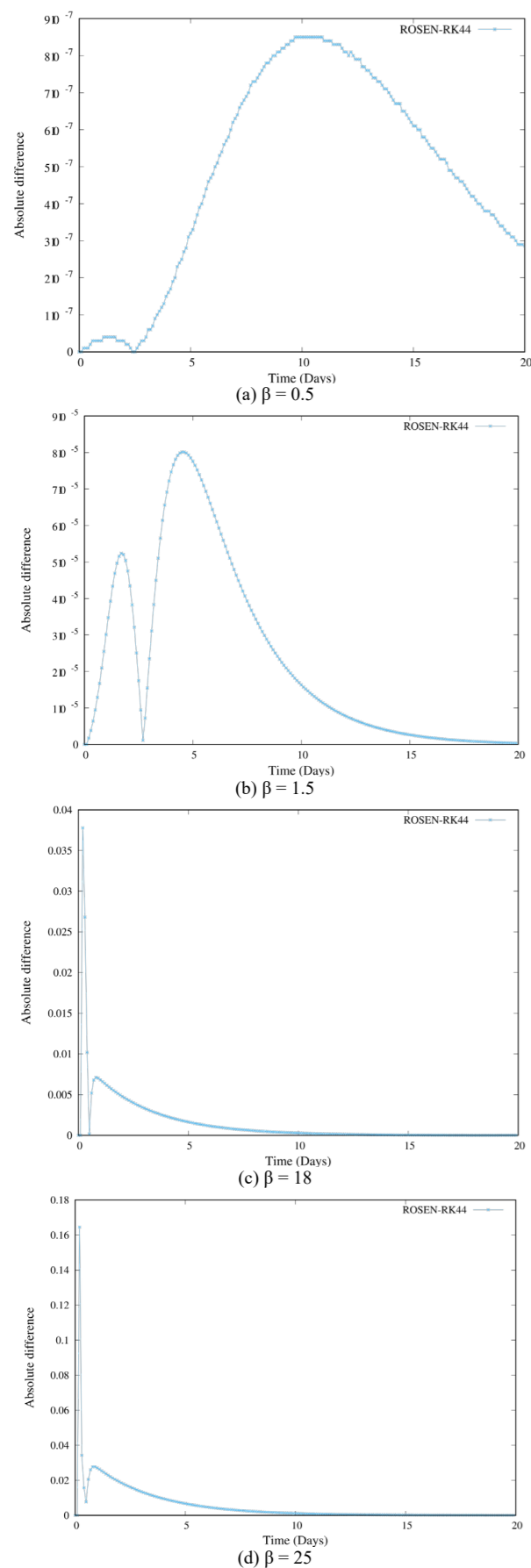

(c) β = 18

(d) β = 25

Fig. 6. Difference between the numerical solution of the infected population using RK44 and Rosenbrock methods with step-size h = 0.1. Simulated scenarios with distinct choices of β.

V. CONCLUSIONS

In this work, we numerically investigate the stiffness phenomena for the epidemiological SIR model. The simulated scenarios presented show that the stiffness ratio of the SIR model becomes more pronounced as the disease contagion rate increases or the rate of birth/mortality approaches zero. However, the numerical findings indicate that the explicit numerical method have more difficulties to obtain a numerical solution satisfying Theorem 1 as β increases. In particular, the stiffness phenomena imply that the numerical solution using explicit methods, such as Euler and the RK, does not agree with the theoretical results on Theorem 1, while the semi-implicit Rosenbrock method does agree with the theoretical results. The analysis of the maximum and quadratic difference between the analyzed explicit methods and the Rosenbrock method becomes large near the peak of the infection. As a result, the explicit methods overestimate the peak of infection.

We also demonstrate how to use the Rosenbrock method to determine an optimal step-size in terms of β to use in the explicit numerical method, resulting in a more accurate numerical solution for the SIR model. This step-size can be used in explicit methods, e.g., the Euler's method, which is a good alternative to reduce the computational cost.

The results obtained in this contribution collaborate with the following conjecture regarding the use of explicit numerical methods for the SIR model: For a given β choose h such that $\beta h < 0.1$. It will be investigated in detail in future contributions.

REFERENCES

[1] D. Bernoulli, "Essai D'une Nouvelle Analyse de la Mortalité Causée par la Petite Vérole, et Désavantages de L'inoculation Pour la Prévenir, Histoire de l'Acad., Roy. Sci., Paris, pp. 1-45, 1760.

[2] N. M. Ferguson, D. Laydon, G. Nedjati-Gilani and et al., "Impact of Non-pharmaceutical Interventions (NPIs) to Reduce COVID-19 Mortality and Healthcare Demand", Imperial College COVID-19 Response Team, London, pp. 1-20, 2020.

[3] W.O. Kermack, and A. G. Mckendrick, "A Contribution to the Mathematical Theory of Epidemics", Proceedings of the Royal Society of London, London, vol. 115, pp. 700-721, 1927.

[4] J. D. Lambert, "Numerical Methods for Ordinary Differential Systems: The Initial Value Problem", 1st ed., New York: Wiley, 1991.

[5] H. W. Hethcote, "The Mathematics of Infectious Diseases", SIAM review, vol. 42, pp. 599-653, 2000.

[6] C. F. Curtiss, and J. O. Hirschfelder, "Integration of Stiff Equations", Proceedings of the National Academy of Sciences of the United States of America, vol. 38, pp. 235–243, 1952.

[7] J. Kumate, "Infectious Diseases in the 21st Century", Archives of Medical Research, vol. 28, pp. 155-161, 1997.

[8] I. F. Souza, "Queda nas Taxas de Cobertura Vacinal e Recrudescimento do Sarampo no Brasil: Revisão de Literatura. 2021", Anais. Bauru: Faculdade de Odontologia de Bauru, Universidade de São Paulo. Available: https://repositorio.usp.br/directbitstream/41cdd6d5-ca58-48b8-9b35-c5c2000c447b/3083766.pdf [Accessed: Aug. 05, 2022], 2021.

[9] J. C. Marques, A. De Cezaro, and M. J. Lazo, "A SIR Model with Spatially Distributed Multiple Populations Interactions for Disease Dissemination". Trends in Computational and Applied Mathematics - SBMAC, vol. 23, pp. 143-154, 2022.

AUTHORS

Marline Ilha da Silva

Brazilian researcher, born in Santa Maria, city of the Rio Grande do Sul. She has a degree in Mathematics from the Federal University of Santa Maria(UFSM). Master in Applied Mathematics from Institute of Mathematics and Statistics of the University of São Paulo(USP). PhD in Applied Mathematics from Federal University of Rio Grande do Sul(UFRGS). During these years of study, she researched in the areas of the areas of Fluid Dynamics, Numerical Analysis, Numerical Methods for Partial and Ordinary Differential Equations. She has experience with problems of rigid equations, among these problems, she developed a research work on analysis of rigid equations obtained from the modeling of the biogas production process. She is currently a professor at the Federal Institute of Education of Rio Grande do Sul(IFRS) and teaches Mathematics for technical courses, and Numerical Calculus and Linear Algebra for the Industrial Electronics course.

Joice Chaves Marques

She specializes in Applied Mathematics with an emphasis on Biomathematics. Graduated in Mathematics (Full Degree) and Master in Applied Mathematics at the Federal University of Santa Maria. She completed her PhD in Applied Mathematics at the Federal University of Rio Grande do Sul. She has already been an exchange student participating in the project "International Insertion of Biomathematics of PPGMat/UFSM" developed in partnership with the University of Osnabrück in Germany. In the period from 07/2020 to 07/2021, carried out a Post Doctorate in Computational Modeling at the Federal University of Rio Grande (FURG) as part of the executing team of the project "Creation of digital solutions for control, monitoring, and forecasting the spread of COVID-19" which enabled predictions of the number of infected people for the state of Rio Grande do Sul. The results of this project were of great importance and were reported in local newspapers, as can be seen at https://www.sbt.com.br/riograndedosul/jornalismo/sbt-rio-grande-2-edicao#videos and https://www.furg.br/coronavirus-noticias/cientistas-da-furg-criam-sistema-para-estimar-numero-de-infectados-no-rs. In her work, she used spatially structured models via the Linked Maps Network. She is currently an Adjunct Professor at the Federal University of Rio Grande and teaches Computational Numerical Calculus for Engineering courses.

Adelaida Otazu Conza

Undergraduate teacher at the Faculty of Mathematical Physical Sciences of the National University of the Altiplano (UNAP) in the city of Puno-Peru. She completed undergraduate studies at the National University of the Altiplano, obtaining the title of Bachelor of Physical Mathematical Sciences. Postgraduate studies, Masters and Doctorate were carried out in Applied Mathematics by the Federal University of Rio Grande do Sul (UFRGS) Brazil. In pregado she initiates an investigation in Fractals. In the master's degree, she worked in the area of Fluid Dynamics related to the modeling and simulation of the dispersion of a pollutant in water. In her PhD, she researches in the area of Combustion, in modeling and simulation of Methyl Formate biofuel and for Methyl Decanoate biodiesel, which involves numerically solving various systems of partial differential equations, systems of ordinary differential equations, stiff and coupled. She is currently doing research in fluid dynamics, beginning in the area of biomathematics.

Adriano De Cezaro

Graduated in Mathematics from the Federal University of Rio Grande in 2003, Master in Mathematics and Scientific Computing from the Federal University of Santa Catarina in 2006 and PhD in Mathematics from the National Institute of Pure and Applied Mathematics Association in 2010. Since 2008 he is Professor at the Federal University of Rio Grande. He has experience in Applied Mathematics, with emphasis on Inverse Problems where the main proposal is to study parameter identification problems in tomography models, differential equation models and propose regularization strategies for such inverse problems, as for example, iterative and continuous regularization methods, level set methods for inverse problems. He is also interested in modeling dynamic systems in biophysical models, with applications in disease dispersion and biological rhythms.

AUTHORS

Ana Carla Ferreira

Brazilian researcher, born in Alegrete, city of the Rio Grande do Sul. PhD student in Computational Modeling at the Federal University of Rio Grande (FURG). Master in Computational Modeling at the Federal University of Rio Grande (FURG), presenting the work entitled The Fractional compartmental SIRC model, as can be seen at https://repositorio.furg.br/handle/1/7857. Graduated in Mathematics from the Federal Institute of Education, Science and Technology Farroupilha (IFFar). She is a teacher of basic education at Colégio Salesiano Leão XIII, in the city of Rio Grande. She works as a collaborator in the Study Group on Educational Policies and Management (GEPGE), linked to IFFar, in the Project Conselhoedu: Development of a platform for training and participatory management of Education Councils. She participates in the Gamma Research Group at FURG. She is interested in Applied Mathematics with an emphasis on Epidemiological Models working with Fractional Order Calculus with differential equation models.

A Fractional SIRC model for the spread of diseases in two interacting populations

Ana Carolina Maurmann
Inst. Mathematics, Statistics and Physics
Federal University of Rio Grande
Rio Grande, Brazil
ana.carolina.maurmann@hotmail.com
ORCID: 0009-0008-9877-1415

Fabiana Tracessini De Cezaro
Inst. Mathematics, Statistics and Physics
Federal University of Rio Grande
Rio Grande, Brazil
fabi.travessini@gmail.com
ORCID: 0000-0001-9401-5315

Adriano De Cezaro
Inst. Mathematics, Statistics and Physics
Federal University of Rio Grande
Rio Grande, Brazil
decezaromtm@gmail.com
ORCID: 0000-0001-8431-9120

A FRACTIONAL SIRC MODEL FOR THE SPREAD OF DISEASES IN TWO INTERACTING POPULATIONS

Ana Carolina Maurmann
Inst. Mathematics, Statistics and Physics
Federal University of Rio Grande
Rio Grande, Brazil
ana.carolina.maurmann@hotmail.com
ORCID: 0009-0008-9877-1415

Fabiana Tracessini De Cezaro
Inst. Mathematics, Statistics and Physics
Federal University of Rio Grande
Rio Grande, Brazil
fabi.travessini@gmail.com
ORCID: 0000-0001-9401-5315

Adriano De Cezaro
Inst. Mathematics, Statistics and Physics
Federal University of Rio Grande
Rio Grande, Brazil
decezaromtm@gmail.com
ORCID: 0000-0001-8431-9120

Abstract—In this contribution we address the following question: what is the behavior of a disease spreading between two distinct populations that interact, under the premise that both populations have only partial immunity to circulating stains of the disease? Our approach consists of proposing and analyzing a multi-fractional Susceptible (S), Infected (I), Recovered (R) and Cross-immune (C) compartmental model, assuming that the dynamics between the compartments of the same population is governed by a fractional derivative, while the interaction between distinct populations is characterized by the proportion of interaction between susceptible and infected individuals of both populations. We prove the well-posedness of the proposed dynamics, which is complemented with simulated scenarios showing the effects of fractional order derivatives (memory) on the dynamics.

Keywords— *Mathematical modeling, Diseases spreading, Immunological memory, Population interaction*

I. INTRODUCTION

The astonishing spread of infection diseases in recent years (e.g., influenza and the COVID-19 pandemic) is among the main concerns of human civilization because they represent one of the main causes of population mortality, e.g., [13]. The track of the recent pandemics shows that one important mechanism for their global spread is the interaction between distinct populations. Furthermore, many infection diseases are capable of gene recombination with those of currently circulating strains, giving rise to new viral sub-types capable of escaping (partially) the immune system defenses of previously infected or vaccinated hosts, conferring only a partial immunity (cross-immunity) of the population, See, [1,10] and references therein.

Many mathematical models have been proposed to describe the dynamics of diseases and their mutations in the population (see [4] for a review). A typical approach uses multiple SIR, connected via some cross-immunity parameters, to model the interactions between individuals that are (or have been) infected by different viral strains, e.g., [2]. The analysis of these models has shown that multiple strains of certain diseases can persist in the human population and that their prevalence can exhibit self-sustained oscillations through time. In [12] the author suggested a model with immunity loss to incorporate re-infection by distinct strains.

In [9] the proposed model incorporates a 'temporary partial immunity' for the R compartment to handle the virus mutation. In [3], a new compartment (C), for cross-immune individuals (individuals that are not fully susceptible (S) or recovered (R)) is introduced. Individuals in this new compartment have their immune responses boosted by exposition to mutated strains. This model is called SIRC. In [7,8], a fractional and multi-fractional dynamics for the SIRC model (called (F)-SIRC and (MF)-SIRC models, respectively) are proposed and analyzed. The authors show that the (MF)-SIRC model is capable of describing with better agreement data from the H1N1 influenza diseases. Moreover, the fractional dynamics allows for accounting for memory in the immune system (immunological memory).

In the approaches above cited, the interaction between populations is not considered. The main contributions of this manuscript are the proposal and the analysis of a multi-fractional SIRC model with two populations that interact ((MP)-FSIRC model). This method allows determining the effects of immunological memory in one sub-population (for example, acquired through vaccination) on disease propagation into a second sub-population, as well as the effects on disease dissemination and cross-immunity.

Outline: In Section II, we present the (MP)-FSIRC model with two populations that interact. We show the well-posedness of the proposed dynamic in Section III. In Section IV, we analyze numerically some simulated scenarios for the proposed model. In Section V, we formulate some conclusions and future directions.

II. MATHEMATICAL MODELING

We assume two distinct sub-populations exist, with the total number of individuals in each sub-population $N_j(t) = S_j(t) + I_j(t) + R_j(t) + C_j(t)$ distributed in the compartments of Susceptible (S_j), Infected or Infectious (I_j), Recovered or Removed (R_j) and Cross-immune (C_j), for $j = 1, 2$. Furthermore, there is an interaction between the individuals of the distinct populations. Such interactions allow susceptible individuals from sub-population i to become infected through contact with infected individuals from sub-population j for $i, j = 1, 2$ and $i \neq j$. The probability of the aforementioned fact happening is proportional to the contact between the distinct sub-populations and is given by $\beta_{ij}S_i(t)I_j(t)$, for $i, j = 1, 2$ and $i \neq j$. We also consider that each sub-population has some immunological memory and that such immunological memory is described by the fractional dynamics given by the Caputo fractional derivative operator $D^{\theta_j}(\cdot)$ of order $\theta_j \in]0, 1]$ (see [5] for the definition of the Caputo derivative and its memory-enhancing effect).

In other words, the disease dynamics follows the multi-fractional coupled system (MP)-FSIRC, given by:

$$
\begin{aligned}
D^{\theta_j} S_j(t) &= \mu_j(N_j - S_j(t)) - \beta_{jj}S_j(t)I_j(t) \\
&\quad - \beta_{ij}S_j(t)I_i(t) + \gamma_j C_j(t) \\
D^{\theta_j} I_j(t) &= \beta_{jj}S_j(t)I_j(t) + \beta_{ji}S_j(t)I_i(t) \\
&\quad + \sigma_j \beta_{jj}C_j(t)I_j(t) - (\mu_j + \alpha_j)I_j(t) \\
D^{\theta_j} R_j(t) &= ((1 - \sigma_j)\beta_{jj}C_j(t) + \alpha_j)I_j(t) \\
&\quad - (\mu_j + \delta_j)R_j(t) \\
D^{\theta_j} C_j(t) &= \delta_j R_j(t) - \beta_{jj}C_j(t)I_j(t) - (\mu_j + \gamma_j)C_j,
\end{aligned}
\tag{1}
$$

and initial conditions

$$
S_j(0) \geq 0, I_j(0) \geq 0, R_j(0) \geq 0, C_j(0) \geq 0,
\tag{2}
$$

for $i, j = 1, 2$ and $j \neq i$. All the parameters in the model (MP)-FSIRC (1) are assumed to be constant. The parameters α_j, δ_j and γ_j are the average inverses of the time spent by individuals in the three compartments I_j, R_j, and C_j, respectively. The birth and mortality rates is given by μ_j. The average reinfection probability of an individual in C_j is σ_j. For $i, j = 1, 2$, respectively, β_{ij} represents the infection rate between individuals in the same population if $i = j$, whereas represents the infection rate between distinct populations in case of $i \neq j$.

$$
\begin{aligned}
&\mu_1(N_1(t) - S_1(t)) - \beta_{11}S_1(t)I_1(t) - \beta_{12}S_1(t)I_2(t) \\
&+ \gamma_1 C_1(t) \leq \mu_1(|N_1(t)| + |S_1(t)|) + \beta_{11}|S_1(t)||I_1(t)| \\
&+ \beta_{12}|S_1(t)||I_2(t)| + \gamma_1|C_1(t)| \leq \mu_1 N(0) + \mu_1|S_1(t)| \\
&+ \beta_{11}N(0)|I_1(t)| + \beta_{12}N(0)|I_2(t)| + \gamma_1|C_1(t)| \leq \tilde{w}_1 \\
&+ \tilde{w}_2\|X(t)\|,
\end{aligned}
$$

III. WELL-POSEDNESS FOR THE (MP)-FSIRC MODEL

In this section, we show the existence of a unique continuous solution

$$
X(t) := (S_1(t), I_1(t), R_1(t), C_1(t), S_2(t), I_2(t), R_2(t), C_2(t))^T
$$

for $t \geq 0$ of the (MP)-FSIRC model (1) with initial conditions (2). We also show that such a solution is continuously dependent on the initial conditions, system parameters, and the fractional-order of the Caputo derivatives $\theta_j \in]0, 1]$, for $j = 1, 2$. We begin showing some preliminary results concerning the (MP)-FSIRC model (1).

Lemma 1: Let $N(t) = N_1(t) + N_2(t)$, where $N_j(t)$ is the total of individuals of sub-population $j = 1, 2$. Then $N(t)$ is constant for any $t \geq 0$.

Proof: It follows from the linearity of the fractional derivative (see [5]) that

$$
D^{\theta_j} N_j(t) = D^{\theta_j} S_j(t) + D^{\theta_j} I_j(t) + D^{\theta_j} R_j(t) + D^{\theta_j} C_j(t)
$$

for $j = 1, 2$. Summing up the right hand side of (MP)-FSIRC model (1), we have that $D^{\theta_j} N_j(t) = 0$, for any $j = 1, 2$. Hence $N_j(t)$ is constant, for $j = 1, 2$ (see e.g., [5]) and the assertion follows. ∎

Lemma 2: If a solution $X(t)$ of (MP)-FSIRC (1) model with initial conditions (2) exists, then it is uniformly bounded by $N(0)$. In particular all the coordinates of $X(t)$ are uniformly bounded.

Proof: Let $\|\cdot\|_1$ be the 1-norm in $\mathbb{R}^n$. It follows that $\|X(t)\|_1 \leq \|N(t)\|_1$, for any $t \geq 0$. Since $N(t)$ is constant (see Lemma 1), the assertion follows. ∎

Let the map $F: [0, \infty) \times \mathbb{R}^8 \to \mathbb{R}^8$ given by

$$
F(t, X(t)) := \begin{bmatrix} F_1(t, X(t)) \\ 0_{4x1} \end{bmatrix} + \begin{bmatrix} 0_{4x1} \\ F_2(t, X(t)) \end{bmatrix}, \text{ where}
$$

$0_{4x1} = (0, 0, 0, 0)^T$ and $F_j: [0, \infty) \times \mathbb{R}^8 \to \mathbb{R}^4$ are the right hand side of \eqref{sistema:P1}, for $i, j = 1, 2$, with $i \neq j$, respectively.

Proposition 1: Let the map $F(t, X(t))$ defined above. Then:
i. $F(t, X(t))$ is continuous for $t \geq 0$.
ii. There exist constants w_1 and w_2 such that $\|F(t, X(t))\| \leq w_1 + w_2\|X(t)\|$.
iii. $F(t, X(t))$ is Lipschitz continuous w.r.t. the second coordinate.

Proof: Item i) is derived from the fact that each coordinate of $F(t, X(t))$ is made up of the sum and product of continuous functions. Using Lemma 2, we can conclude that the first coordinate of $F(t, X(t))$ is such that

$$
\begin{aligned}
&\mu_1 N_1(t) - (\mu_1 + \beta_{11}I_1(t) + \beta_{12}I_2(t))S_1(t) + \gamma_1 C_1(t) \leq \\
&\mu_1|N_1(t)| + (\mu_1 + \beta_{11}|I_1(t)| + \beta_{12}|I_2(t)|)|S_1(t)| + \gamma_1|C_1(t)| \\
&\leq \mu_1 N(0) + \mu_1|S_1(t)| + \beta_{11}N(0)|I_1(t)| + \beta_{12}N(0)|I_2(t)| \\
&+ \gamma_1|C_1(t)| \leq \tilde{w}_1 + \tilde{w}_2\|X(t)\|,
\end{aligned}
$$

where $\tilde{w}_1 = \mu_1 N(0)$ and $\tilde{w}_2 = \max\{\mu_1, \beta_{11}N(0), \beta_{12}N(0), \gamma_1\}$.

With analogous arguments presented above for each coordinate of $F(t, X(t))$, the assertion on item~ii follows.

A. C. Marumann, F. Travessini De Cezaro, and A De Cezaro,
"A Fractional SIRC model for the spread of diseases in two interacting populations",
Latin-American Journal of Computing (LAJC), vol. 10, no. 2, 2023.

Applying the Mean Value Theorem, we get the existence of a $\nu \in [0,1]$ such that, for any $\xi(t) = X(t) + \nu \tilde{X}(t)$,

$$F(t, X(t)) - F(t, \tilde{X}(t)) = JF(t, \xi)(X(t) - \tilde{X}(t)), \quad (3)$$

where $JF(t, \cdot)$ is the Jacobian of the map $F(t, \cdot)$, given by

$$JF(t, X(t)) := \begin{bmatrix} JF_1(t, X(t)) \\ 0_{4\times 8} \end{bmatrix} + \begin{bmatrix} 0_{4\times 8} \\ JF_2(t, X(t)) \end{bmatrix}.$$

Here $0_{4\times 8}$ denotes the 4×8 null matrix. Since $JF_1(t, X(t)) = A_1 + A_2$ where A_1 and A_2 are given by

$$\begin{bmatrix} a_{11} & a_{12} & 0 & \gamma_1 & 0 & a_{16} & 0 & 0 \\ -a_{11} & a_{22} & 0 & 0 & 0 & 0 & 0 & 0 \\ 0 & a_{32} & \delta_1 & a_{34} & 0 & 0 & 0 & 0 \\ 0 & 0 & \delta_1 & a_{44} & 0 & 0 & 0 & 0 \end{bmatrix} \text{ and}$$

$$\begin{bmatrix} 0 & 0 & 0 & 0 & 0 & 0 & 0 & 0 \\ \mu_1 & 0 & 0 & \sigma_1\beta_{11}I_1 & 0 & \beta_{12}S_1 & 0 & 0 \\ 0 & & -\mu_1 & & 0 & 0 & 0 & 0 \\ 0 & -\beta_{11}C_1 & & & 0 & 0 & 0 & 0 \end{bmatrix},$$

respectively, for $a_{11} = -\mu_1 - \beta_{11}I_1 - \beta_{12}I_2$, $a_{12} = -\beta_{11}I_1$, $a_{16} = -\beta_{12}S_1$, $a_{22} = \beta_{11}S_1 + \sigma - \beta_{11}I_1 - (\mu_1 + \gamma_1)\beta_{11}C_1 - (\mu_1 + \alpha_1)$, $a_{32} = (1 - \sigma_1)\beta_{11}C_1 + \alpha_1$, $a_{34} = (1 - \sigma_1)\beta_{11}I_1$, $a_{44} = -\beta_{11}I_1 - (\mu_1 + \gamma_1)$. On the other hand, $JF_2(t, X(t))$ is given by

$$\begin{bmatrix} b_{11} & b_{12} & 0 & \gamma_2 & 0 & b_{16} & 0 & 0 \\ -b_{11} & b_{22} & 0 & 0 & 0 & 0 & 0 & 0 \\ 0 & b_{32} & \delta_2 & b_{34} & 0 & 0 & 0 & 0 \\ 0 & 0 & \delta_2 & b_{44} & 0 & 0 & 0 & 0 \end{bmatrix} +$$

$$\begin{bmatrix} 0 & 0 & 0 & 0 & 0 & 0 & 0 & 0 \\ \mu_2 & 0 & 0 & \sigma_2\beta_{22}I_2 & 0 & \beta_{21}S_2 & 0 & 0 \\ 0 & b_{32} & -\mu_2 & 0 & 0 & 0 & 0 & 0 \\ 0 & -\beta_{22}C_2 & 0 & 0 & 0 & 0 & 0 & 0 \end{bmatrix},$$

where $b_{11} = -\mu_2 - \beta_{22}I_2 - \beta_{22}I_1$, $b_{12} = -\beta_{22}I_2$, $b_{16} = -\beta_{21}S_2$, $b_{22} = \beta_{22}S_2 + \sigma_2\beta_{22}C_2 - (\mu_2 + \alpha_2)$, $b_{32} = (1 - \sigma_2)\beta_{22}C_2 + \alpha_2$, $b_{34} = (1 - \sigma_2)\beta_{22}I_2$, and $b_{44} = -\beta_{22}I_2 - (\mu_2 + \gamma_2)$.

Hence, it follows from Lemma 2 that each coordinate of $JF(t, X(t))$ is uniformly bounded. As a results, there exists $L > 0$ such that $\|JF(t, X(t))\| \le L$. Therefore, from (3) and the Cauchy-Schwarz inequality, the assertion iii) follows.∎

The theorem that follows is the main theoretical result of this contribution.

Theorem 1: Let the (MP)-FSIRC (1) and the corresponding initial conditions (2). Then:

[Existence and uniqueness] There is a unique continuous solution $X(t)$ for the (MP)-FSIRC model (1), for $t \in [0, \infty)$.

[Continuous dependence] The (MP)-FSIRC model (1) solution $X(t)$ is continuously dependent on the model

parameters and fractional derivatives $\theta_j \in]0, 1]$, for any $j = 1, 2$.

Proof: Integrating the (MP)-FSIRC model (1) with order θ_j for $j = 1, 2$ results in the model being equivalent to Volterra's system of equations

$$x_k(t) = \frac{1}{\Gamma(\theta_k)} \int_0^t (t-s)^{\theta_k - 1} f_k(s, x_1(s), ..., x_8(s)) ds \quad (4)$$
$$+ \sum_{l=1}^{8} x_k(0)\frac{t^l}{l!}$$

where f_k and x_k represents the k-coordinate of $F(t, X(t))$ with $\theta_k = \theta_1$, if $k = 1, \cdots, 4$ and $\theta_k = \theta_2$ if $k = 5, \cdots, 8$. Let $\theta = min\{\theta_1, \theta_2\}$. Then (4) can be rewritten as

$$x_k(t) = \frac{1}{\Gamma(\theta_j)} \int_0^t (t-s)^{\theta - 1} \hat{f}_k(s, x_1(s), ..., x_8(s)) ds \quad (5)$$
$$+ \sum_{l=1}^{8} x_k(0)\frac{t^l}{l!}$$

for $k = 1, 2, ..., 8$, where,

$$\hat{f}_k(s, x_1, ..., x_8) := \frac{\Gamma(\theta)}{\Gamma(\theta_j)}(t-s)^{\theta_j - \theta} f_k(s, x_1, ..., x_8).$$

Let $\hat{F} := (\hat{f}_1, ..., \hat{f}_8)^T$ be the expression of the vector map $F(t, X(t))$ with coordinates corresponding to $\hat{f}_k(t, X(t))$, for $k = 1, \cdots, 8$. We know from Proposition 1 itens-i)-iii) that $F(t, X(t))$ is continuous with respect to t and Lipschitz is continuous with respect to $X(t)$. A direct calculation reveals that $\hat{F}(t, X(t))$ also meets these requirements. Therefore, the Fixed Point Theorem (as used in the Picard theorem - see also Theorem 8.3 in [5]) can be applied to guarantee the existence of a unique continuous solution $X(t)$ for the (MP)-FSIRC (1) with initial conditions (2), in the interval $[0, T^*]$ for some $T^* > 0$. Moreover, Proposition 1, ii) implies that F is linearly increased. Therefore, the assumptions of Theorem 3.1 in [11] are satisfied. It implies that the solution $X(t)$ can be continuously extended to the positive real line. It concludes the assertion i). Furthermore, Proposition 1 implies that the assumptions of Theorem~6.20 - 6.22 in [5] hold true. Hence, item ii) follows. ∎

IV. SIMULATED SCENARIOS

In this section, we present some simulated scenarios for the (MP)-FSIRC (1). The numerical solution for the (MP)-FSIRC (1) calculated using a trapezoidal type method with a mesh size of $h = 10^{-3}$ of (5), proposed in [6]. Since the mesh-size corresponds to the time scale, we re-scale all the parameters accordingly. The simulations are run for a time corresponding to 120 days and for choices of the fractional derivatives of order $\theta_1, \theta_2 \in \{1, 0.8, 0.6\}$.

A. Scenario with Symmetric Sub-populations

In this section, we present distinct scenarios of the proposed dynamics for a symmetric population. It means that $N_1 = N_2 = 1$. The remaining parameters are given by $\mu_1 = \mu_2 = 0.0001$, $\beta_{11} = \beta_{22} = 1.2$, $\beta_{12} = \beta_{21} = \beta_{11}/10$, $\gamma_1 = \gamma_2 = 0.1$, $\alpha_1 = \alpha_2 = 0.1$, $\delta_1 = \delta_2 = 0.25$. The initial conditions are such that $X(0) = (0.9, 0.1, 0, 0, 1, 0, 0, 0)^T$,

implying that only the sub-population 1 is infected at $t = 0$, whereas the population 2 is infection-free.

Fig. 1. Dynamics of infection on the sub-population 1, in the scenario of symmetric populations

Fig. 2. Dynamics of cross-immune on the sub-population 1, in the scenario of symmetric populations
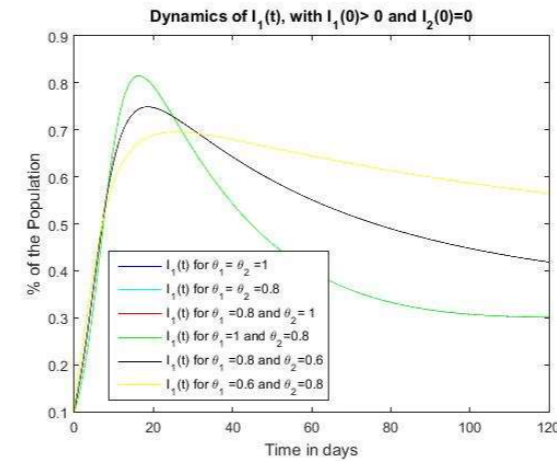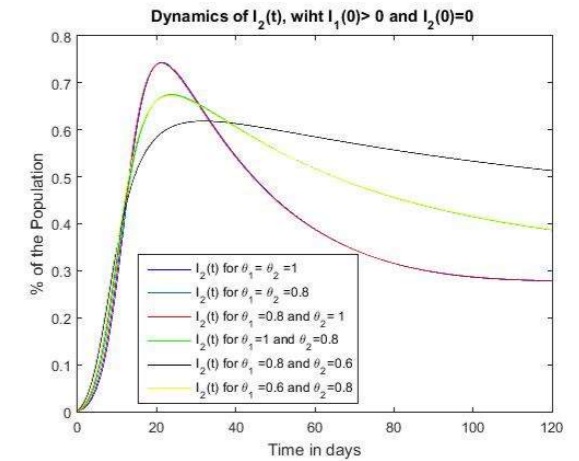

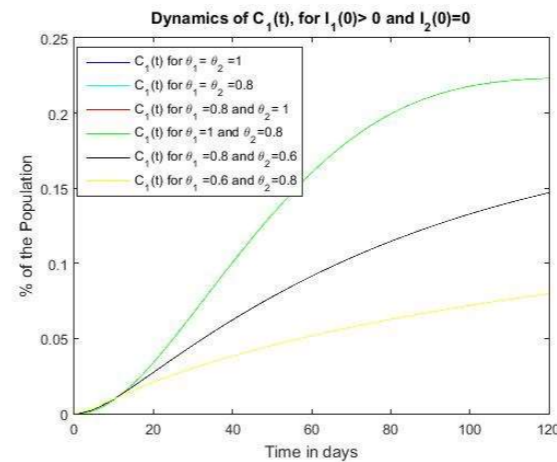Fig. 3. Dynamics of infection on the sub-population 2, in the scenario of symmetric populations

Fig. 4. Dynamics of cross-immune on the sub-population 2, in the scenario of symmetric populations
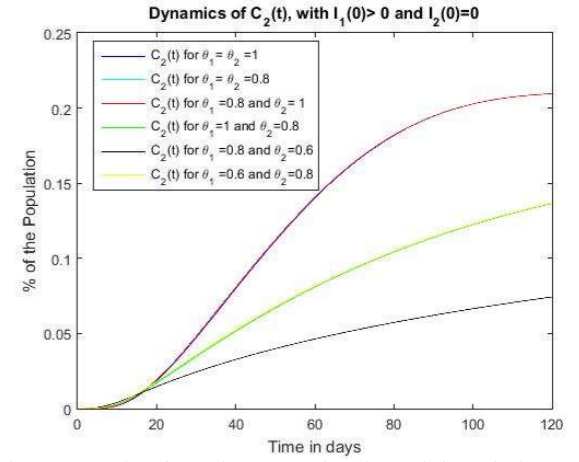

Fig. 5. Dynamics of infection on the total population, in the scenario of symmetric populations

Figures 1 and 2 show the dynamics of infection and cross-immunity for both sub-populations. Looking only at the simulated scenarios (the simulated scenarios in "black---", "cyan---" and "red---" are almost coincident, as well as the ones in "blue---" and "green---") for the sub-population 1, we conclude that the best strategy is the one in which the sub-population 1 has more immunological memory ($\theta_1 \le \theta_2$). The scenario with $\theta_1 = 0.6$ and $\theta_2 = 0.8$ (plotted "yellow---") has a minor peck of infection as well as a minor cross-immunity percentage, whereas $\theta_1 = 1$ (no immunological memory in the sub-population 1) has a higher peck of infection as well as a higher percentage of cross-immunity.

The simulated scenarios for sup-population 2, presented in Figures 3 and 4 lead to a similar conclusion as described above (the simulated scenarios in "blue---" and "red---" as well as the ones in "yellow---", "cyan---" and "green---" are nearly identical), where it can be seen that the relation $\theta_2 \le \theta_1$ corresponds to cases where the diseases have fewer infected
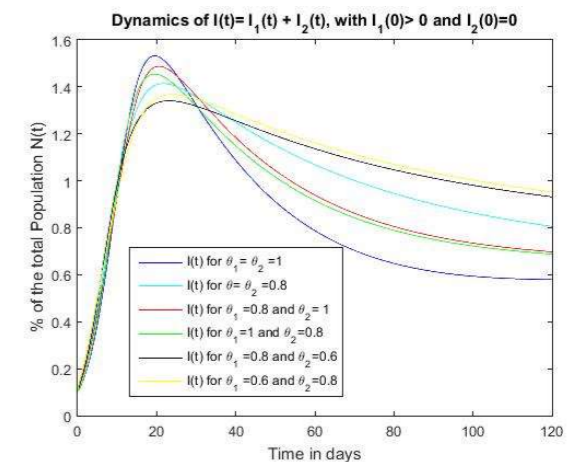
persons at the epidemiological peck and a lower percentage of cross-immunity.
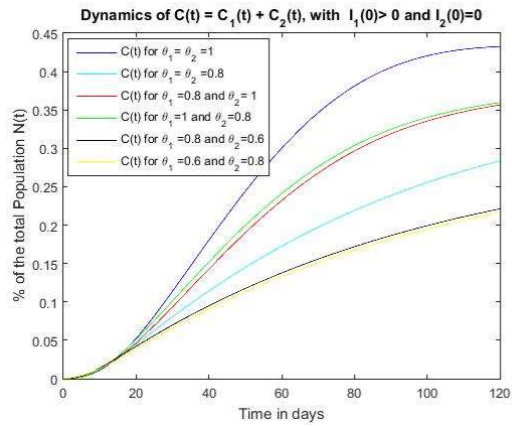
Fig. 6. Dynamics of cross-immune on the total population, in the scenario of symmetric populations

B. Scenario with Non-symmetric Sub-populations

In the following, we analyze some simulated scenarios of the proposed dynamics where the populations are non-symmetric. In the simulations, we use $N_1 = 10$ and $N_2 = 1$. The remaining parameters used are $\mu_1 = \mu_2 = 0.0001$, $\beta_{11} = 1.2$, $\beta_{22} = 0.7$, $\beta_{12} = \beta_{21} = \beta_{11}/10$, $\gamma_1 = \gamma_2 = 0.1$, $\alpha_1 = \alpha_2 = 0.1$, $\delta_1 = \delta_2 = 0.2$, for two scenarios of initial infections.

First scenario: The disease starting in sub-population 1: We first simulate the scenario where the sub-population has infected individuals, while sub-population 2 is free of infection at $t = 0$. It is equivalent to the initial condition $X(0) = (9.99, 0.01, 0, 0, 1, 0, 0, 0, 0)^T$.

Figures 7 to 10 show the dynamics of infection and cross-immunity for both sub-populations in this scenario (the simulated scenarios in "red---", "cyan---" and "yellow---" are almost coincident, as well as those in "blue---" and "green---".). Analyzing the results for the sub-population 1 in Figure 7 and 8, we conclude that the favorable scenario is the one with ($\theta_1 < 1$). The most favorable scenario is depicted in "black---", in which sub-population 2 has more immunological memory ($\theta_2 = 0.6$). However, we cannot conclude that ($\theta_2 \leq \theta_1$) is the best strategy because the ones with $\theta_1 = 1$ and $\theta_2 = 0.8$ (shown in "green---") are just as bad as the ones with no memory (shown in "blue---").

Fig. 7. Dynamics of infected of the sub-population 1, in the scenario with anti-symmetric populations. Diseases starting in the larges sub-population

Fig. 8. Dynamics of cross-immune of the sub-population 1, in the scenario with anti-symmetric populations. Diseases starting in the larges sub-population
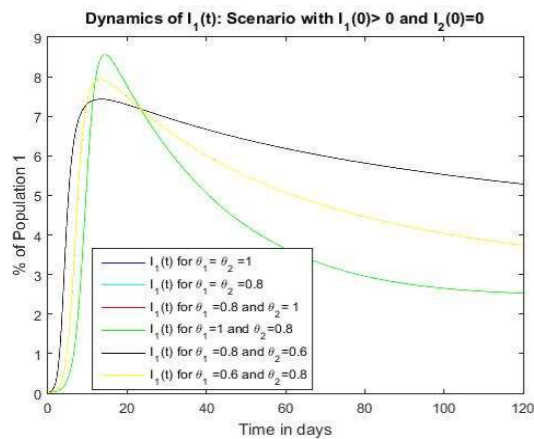

Fig. 9. Dynamics of infected of the sub-population 2, in the scenario with anti-symmetric populations. Diseases starting in the larges sub-population.
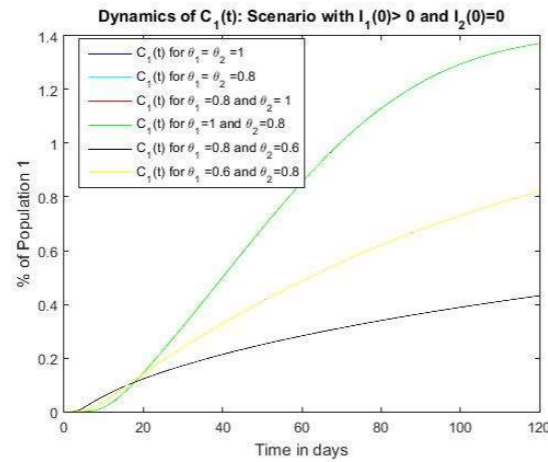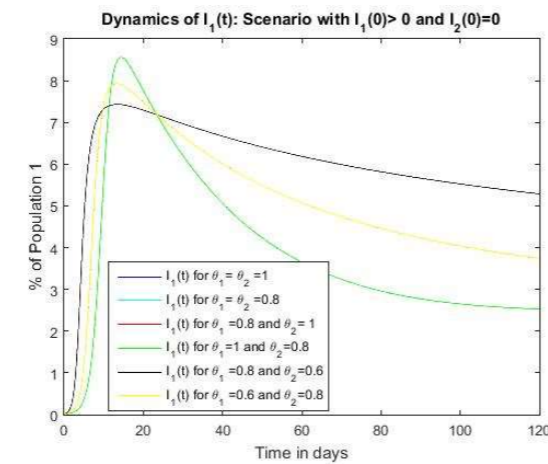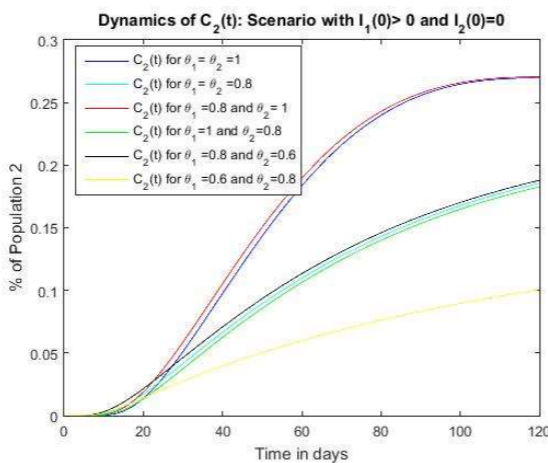

Fig. 10. Dynamics of cross-immune of the sub-population 1, in the scenario with anti-symmetric populations. Diseases starting in the larges sub-population

Fig. 11. Dynamics of the infected population, in the scenario with anti-symmetric populations. Diseases starting in the larges sub-population
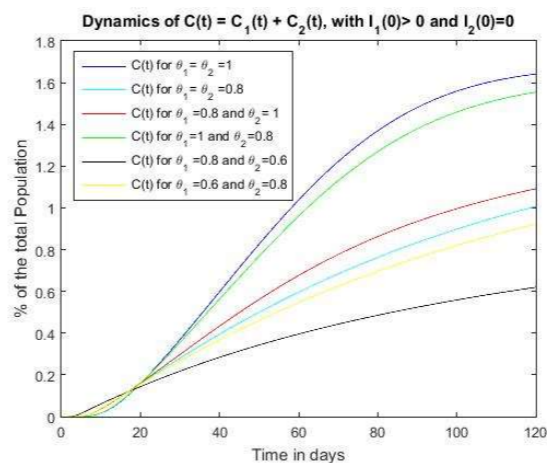
Fig. 12. Dynamics of cross-immune population, in the scenario with anti-symmetric populations. Diseases starting in the larges sub-population.

The analysis of the dynamics of the total population depicted in Figures 11 and 12 shows that the scenarios are favorable if both populations have some memory with $\theta_2 \leq \theta_1$. Otherwise, if $\theta_1 = 1$ (no memory for the sub-population 1), then even if the sub-population 2 has some memory, it is not enough to diminish the effects of the disease (depicted in "green---"). This scenario shows that the strategy is to guarantee immunological memory for both sub-populations, giving more importance to the smallest sub-population. Hence, the simulated scenarios suggest that any vaccination campaing any vaccination campaign should start, if possible, as in the symmetric case, in the sub-population that is disease-free.

Second scenario: The disease starting in sub-population 2: We assume that sub-population 2 has infected individuals while sub-population 1 is free of infection at $t = 0$. This scenario corresponds to the initial condition $X(0) = (10, 0, 0, 1, 0.01, 0, 0)^T$.

Figures 13 to 16 show the dynamics of infection and cross-immunity for both sub-populations in this scenario (the simulated scenarios in "red---", "cyan---" and "yellow---" are almost coincident, as well as those in "blue---" and "green---".). The results for the sub-population 1 in Figure 16 show a favorable scenario if ($\theta_1 < 1$) while for the sub-population 2 is the one with ($\theta_1 = 0.6$) depicted in "yellow---".
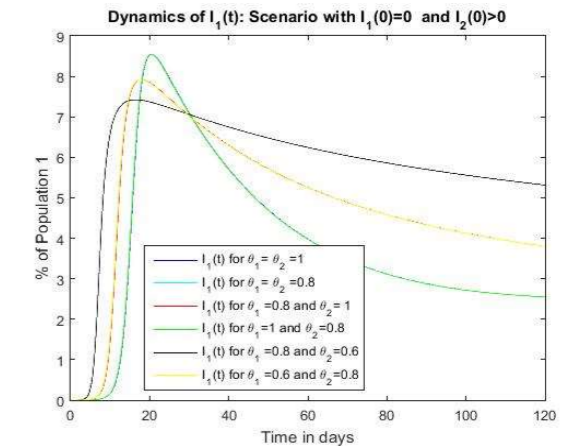
Fig. 13. Dynamics of infected of sub-population 1, in the scenario with anti-symmetric populations. Diseases starting in the smallest sub-population
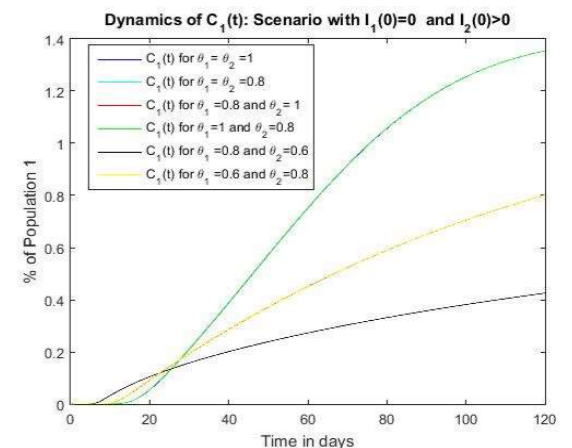
Fig. 14. Dynamics of cross-immune of sub-population 1, in the scenario with anti-symmetric populations. Diseases starting in the smallest sub-population
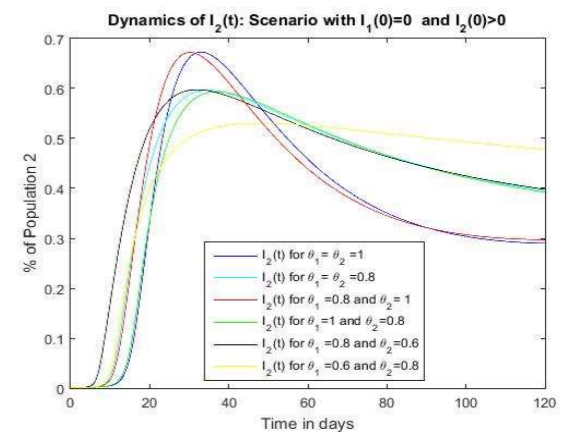
Fig. 15. Dynamics of infected of sub-population 2, in the scenario with anti-symmetric populations. Diseases starting in the smallest sub-population

Fig. 16. Dynamics of cross-immune of sub-population 2, in the scenario with anti-symmetric populations. Diseases starting in the smallest sub-population
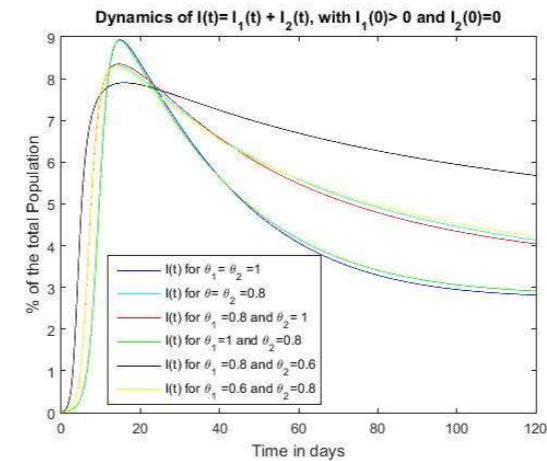

Fig. 17. Dynamics of infected of the total population, in the scenario with anti-symmetric populations. Diseases starting in the smallest sub-population

Fig. 18. Dynamics of of the total population, in the scenario with anti-symmetric populations. Diseases starting in the smallest sub-population
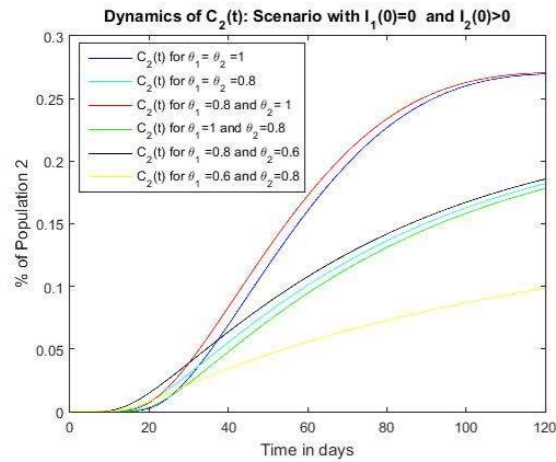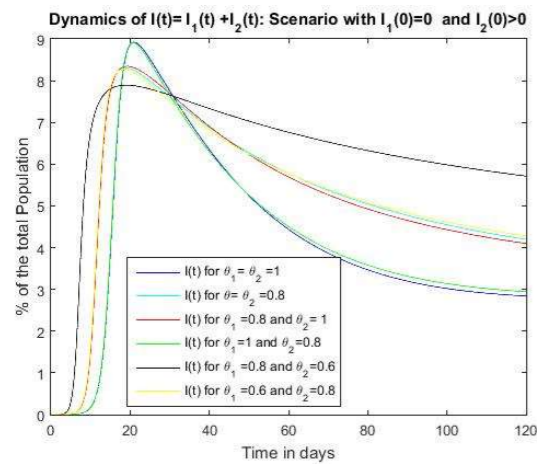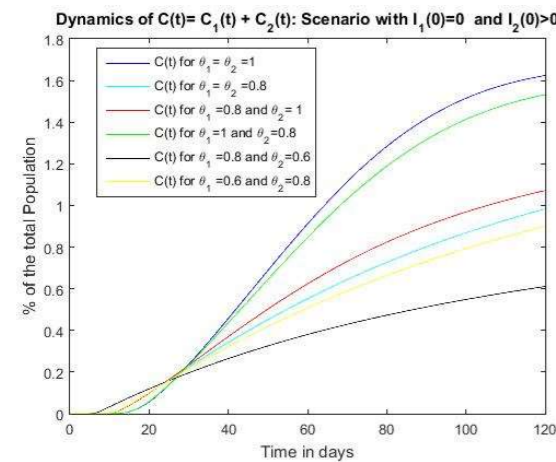
On the other hand, the simulated scenarios for the total population depicted in Figure 17 and 18 show that the

scenarios are favorable for lower values of $\theta_1 + \theta_2$, with $\theta_1 < 1$. This scenario shows that the strategy is to guarantee immunological memory for the sub-populations jointly, giving more importance to the biggest sub-population. This means that, in such a scenario, any vaccination campaign should start for the sub-population that is disease-free, as before.

V. CONCLUSIONS

We propose a multi-fractional derivative dynamics for the SIRC model for disease dissemination as an alternative to describe the existence of immunological memory in a setting with two populations that interact, called (MP)-FSIRC. We prove the well-posedness of the proposed (MP)-FSIRC-model and also present distinct simulated scenarios for the fractional derivative as well as for the sub-population sizes and disease prevalence at $t = 0$. The numerical results show that the existence of immunological memory in both sub-populations (described by the fractional dynamics), in general, presents a favorable epidemiological situation, with smaller infection pecks and less cross-immunity. The most favorable epidemiological scenarios are those in which the disease-free sub-population at $t = 0$ has greater immunological memory, as discussed in Section IV. It turns out that any vaccination campaign should start, if possible, with the sub-population that is disease-free.

The theoretical questions of existence and stability for stationary points as well as simulated scenarios with other choices for the model parameters and fractional order derivatives will be addressed by the authors in future contributions.

REFERENCES

[1] B. Adams and A. Sasaki, "Antigenic distance and cross-immunity, invariability and coexistence of pathogen strains in an epidemiological model with discrete antigenic space". Theoretical population biology, 76, 157-167, 2009.

[2] V. Andreasen, J. Lin, and S. Levin, "The dynamics of co-circulating influenza strains conferring partial cross-immunity". Journal of mathematical biology, 35, 825-842, 1997.

[3] R. Casagrandi, et al., "The SIRC model and influenza A". Mathematical biosciences, 200, 152-169, 2006.

[4] O. Diekmann, J. A. J. Metz, and J. A. P Heesterbeek, "The legacy of Kermack and McKendrick,", in Epidemic Models: Their Structure and Relation to Data, Mollison, D. E. (ed.), Cambridge University Press, Cambridge, 1995.

[5] K. Diethelm, "The analysis of fractional differential equations: An application-oriented exposition using differential operators of Caputo type", Springer Science \& Business Media, Braunschweig, 2010.

[6] R. Garrappa, "Trapezoidal methods for fractional differential equations: Theoretical and computational aspects". Mathematics and Computers in Simulation, 110, 96-112, 2015.

[7] A. C. F. N. Gomes, and A. De Cezaro, "Um estudo sobre a memória epidemiológica: modelo SIRC fracionário". C.Q.D. – Revista Eletrônica Paulista de Matemática, 10, 194-210, 2017.

[8] A. C. F. N. Gomes, and A. De Cezaro, "On a multi-order fractional SIRC model for Influenza". C.Q.D. – Revista Eletrônica Paulista de Matemática, 22, 1-15, 2022.

[9] M. G. M. Gomes, L.J. White, and G. F. Medley, "Infection, reinfection, and vaccination under suboptimal immune protection: epidemiological perspectives". Journal of theoretical biology, 228, 539- 549, 2004.

[10] K. Kuszewski, and L. Brydak,, "The epidemiology and history of influenza". Biomedicine and pharmacotherapy, 54, 188- 195, 2000.

[11] W. Lin, "Global existence theory and chaos control of fractional differential equations". J.Math. Anal. Appl, 1, 332, 709-726, 2007.

[12] C. M. Pease, "An evolutionary epidemiological mechanism, with applications to type A influenza". Theoretical population biology, 31, 422- 452, 1987.

[13] J. Piret, and G. Boivin, "Pandemics Throughout History". Frontiers in Microbiology, 11, 1-16, 2021.

AUTHORS

Ana Maurmann

Graduated in Applied Mathematics from the Federal University of Rio Grande in 2021. Since 2022 she is a candidate of a Master in Applied Mathematics at the Federal University of Rio Grande do Sul. She has experience in Applied Mathematics, with emphasis in applied fractional dynamics or applied dynamical systems with fractional derivatives applied to the dynamics of virus infections and numerical methodos for applied fractional dynamical systems.

Fabiana Tracessini

Graduated in Mathematics from the Federal University of Santa Catarina in 2004, Master in Mathematics and Scientific Computing from the Federal University of Santa Catarina in 2007 and PhD in Mathematics from the Federal University of Rio de Janeiro in 2011. Since 2008 she is Professor at the Federal University of Rio Grande. He has experience in Applied Mathematics, with emphasis on Partial Differential Equations and Inverse Problems, working with Parabolic and Hyperbolic Partial Differential Equations (existence, uniqueness, continuous dependence, decay and stability), Spectral Numerical Methods (analysis of convergence and stability rates), and parameter identification problems in tomography models. She is also interested in modeling dynamic systems in biophysical models, with applications in disease dispersion and biological rhythms.

Adriano De Cezaro

Graduated in Mathematics from the Federal University of Rio Grande in 2003, Master in Mathematics and Scientific Computing from the Federal University of Santa Catarina in 2006 and PhD in Mathematics from the National Institute of Pure and Applied Mathematics Association in 2010. Since 2008 he is Professor at the Federal University of Rio Grande. He has experience in Applied Mathematics, with emphasis on Inverse Problems where the main proposal is to study parameter identification problems in tomography models, differential equation models and propose regularization strategies for such inverse problems, as for example, iterative and continuous regularization methods, level set methods for inverse problems. He is also interested in modeling dynamic systems in biophysical models, with applications in disease dispersion and biological rhythms.

*Estimation of parameters
and state variables in an
alcoholic fermentation
process in a fed-batch
bioreactor*

Lucas Araújo Guimarães
Faculty of Biotechnology
Federal University of Pará
Belém, PA, 66075–110, Brazil
guimaraesaraujolucas@gmail.com
ORCID: 0000-0002-7168-3844

Simone de Aviz Cardoso
Faculty of Biotechnology
Federal University of Pará
Belém, PA, 66075–110, Brazil
simoneaviz@ufpa.br
ORCID: 0000-0002-9676-2987

Diego Cardoso Estumano
Faculty of Biotechnology
Federal University of Pará
Belém, PA, 66075–110, Brazil
dcestumano@ufpa.br
ORCID: 0000-0003-4318-4455

Bruno Marques Viegas
Faculty of Biotechnology
Federal University of Pará
Belém, PA, 66075–110, Brazil
viegasmbruno@gmail.com
ORCID: 0000-0002-2768-652X

Estimation of parameters and state variables in an alcoholic fermentation process in a fed-batch bioreactor

Lucas Araújo Guimarães
Faculty of Biotechnology
Federal University of Pará
Belém, PA, 66075–110, Brazil
guimaraesaraujolucas@gmail.com
ORCID: 0000-0002-7168-3844

Simone de Aviz Cardoso
Faculty of Biotechnology
Federal University of Pará
Belém, PA, 66075–110, Brazil
simoneaviz@ufpa.br
ORCID: 0000-0002-9676-2987

Diego Cardoso Estumano
Faculty of Biotechnology
Federal University of Pará
Belém, PA, 66075–110, Brazil
dcestumano@ufpa.br
ORCID: 0000-0003-4318-4455

Bruno Marques Viegas
Faculty of Biotechnology
Federal University of Pará
Belém, PA, 66075–110, Brazil
viegasmbruno@gmail.com
ORCID: 0000-0002-2768-652X

Abstract — Energy consumption in the world is based on two types of sources: fossil fuels and renewable energy. In this case, bioethanol presents itself as an alternative resource to fossil fuels, whose production can occur through specific processes called alcoholic fermentation. In parallel, the growing demand for energy has resulted in the development of even more efficient systems and technologies. In this work, mathematical modeling and simulation was performed to represent the kinetics of alcoholic fermentation in a fed-batch bioreactor. The modeling was developed taking into account the microbial inhibition caused by the presence of excess substrate and product through the Tosetto and Hoppe-Hansford models. In the simulation, Bayesian statistics was used as a tool to estimate the kinetic parameters and the state variables of the bioprocess. The estimates were obtained through the use of a particle filter proposed by Liu and West, with 500 particles and experimental measurements from the literature, whose approach presented 99% accuracy and proved to be effective for describing alcoholic fermentation.

Keywords— *particle filter, bioreactor, kinetic parameters, alcoholic fermentation, mathematical modeling*

I. INTRODUCTION

Bioethanol is a predominant ethanol strand derived from agricultural materials specifically carbohydrates, such as starch (corn grain) and sucrose (sugarcane), and lignocellulosic biomass. Furthermore, the disposal of feedstock in bioprocesses is a characteristic of bioethanol production [1].

By definition, bioprocesses makes the use of microbial, animal and plant cells, and cellular components such as enzymes. Common or innovative products can be originated and harmful waste can be disposed of through by this way. Bioprocessing is an essential part of industries such as food, chemicals, and pharmaceuticals [2].

Bioethanol is produced through a class of bioprocesses called fermentation processes. In turn, a fermentation system is composed of components such as the living cells of a microorganism (or biomass), the products of metabolism (or metabolites) and nutrients (or substrates) that are arranged in the fermentation medium [3].

These processes differ in the form of operation, such as the mode of substrate addition, product withdrawal, etc. In general, the operation regime of the process is divided into: discontinuous (batch), fed discontinuous (fed-batch) and continuous [4].

In processes involving alcoholic fermentation, fed-batch operation is used in about 75% of Brazilian distilleries, one of the main producing sources in the world, while the remaining 25% operate in continuous mode, using mainly *Saccharomyces cerevisiae* yeast as the ethanol-producing microorganism and agricultural materials as substrate. The operation is conducted at temperatures between 32 and 35 °C. The characteristics of the feed flow, which can last from 4 to 6 hours, are important for the maintenance of the process [5].

The fed-batch alcoholic fermentation consists of an initial stage where the process is discontinuous fed followed by another stage entirely of discontinuous process. The operation regime of the first stage starts with the feeding of a yeast suspension, called inoculum, occupying about 30% of the usable volume of the fermentation vessel, called bioreactor or fermenter. Then, the vessel receives the gradual addition of must, usually a liquid solution consisting of sugarcane juice or molasses diluted with sugarcane juice or water. Afterwards, the process is sequenced in batches until the total consumption of substrate [6].

Studying ways to optimize the fermentation process in order to obtain the maximum yield product is not an easy task. This fact is mainly due to the difficulty in obtaining measurements of the variables that are important in monitoring and controlling the process. To get around these difficulties, an alternative is to perform indirect measurements through appropriate mathematical models that describe the dynamic behavior of fermentation, including taking into account the action of chemical, physical and biological phenomena [7, 8]. In turn, the kinetics of the fermentative process consists primarily in the analysis of the evolution of the concentration values of one or more components of the system, as a function of fermentation time [3].

In this context, the application of the particle filter technique with the algorithm of Liu and West (2001) will be evaluated to perform the estimates of the state variables (substrate concentration, cell, product and volume) and the parameters of the alcoholic fermentation process, considering the already known mathematical modeling of the process [9].

II. METHODOLOGY

A. Mathematical modeling of alcoholic fermentation

The mathematical modeling considered for this study is phenomenological, unstructured, non-segregated modeling. Phenomenological models consist of a set of mathematical relationships, such as mass balance or conservation equations, among the variables of interest in the system under study. The unstructured aspect is observable when the cellular material is represented by a single variable, usually cell mass, without considering variations of intracellular components. While the non-segregated characteristic concerns the cell population considered homogeneous, that is, all the cells present the same behavior [4].

Due to mass conservation balances, phenomenological mathematical models of fermentative processes can be constituted by Ordinary Differential Equations (ODEs) suitable for representing the dynamic of homogeneous systems [10], as presented in (1–4).

$$\frac{dV}{dt} = F \qquad (1)$$

$$\frac{dC_X}{dt} = \left(\mu_X - \frac{F}{V} \right) C_X \qquad (2)$$

$$\frac{dC_S}{dt} = \frac{1}{Y_{X/S}} \mu_X C_X + \frac{F}{V} \left(C_{SF} - C_S \right) \qquad (3)$$

$$\frac{dC_P}{dt} = \frac{Y_{P/S}}{Y_{X/S}} \mu_X C_X - \frac{F}{V} C_P \qquad (4)$$

In the ODEs system, V is the volume of medium in the bioreactor in L, C_X is the cell concentration in g.L^{-1}, C_P is the product concentration in g.L^{-1}, C_{SF} is the substrate concentration in g.L^{-1}, C_{SF} is the substrate concentration at feed in g.L^{-1}, F is the substrate flow rate in L.h^{-1}, μ_X is the specific cell growth velocity in h^{-1}, $Y_{P/S}$ is the product yield relative to substrate in g$_{Cx}$.g$_{Cs}$$^{-1}$ and $Y_{X/S}$ is the cell yield relative to substrate in g$_{Cp}$.g$_{Cs}$$^{-1}$

B. Modeling the specific speed of cell growth

Originally, the modeling of μ_X relies on basic theories of biochemistry. The concept of enzyme kinetics is, by analogy, extended to the microorganism, since it contains a considerable number of enzymes that catalyze the reactions of its metabolism. Thus, it is also assumed that the equations describing the inhibition mechanisms (competitive, noncompetitive, mixed, and acompetitive inhibition) of these agents on a single pure enzyme, are similarly manifested in the microorganism [11]. However, the traditional classification of models for the μ_X parameter is based on the inhibitory agent and can be divided into five groups: those free of inhibition; those that consider inhibition by the substrate, product, or even by the cells themselves; and hybrids that unite the previous inhibition models; as presented in Table I adapted from [1]. The kinetic models for μ_X evaluated in this work are by Tosetto (2002) [12] and Hoppe–Hansford (1982) [13].

Tosetto's model, shown in (15), also propagated as the modified Ghose (1979) model or Andrews/Levenspiel model, is characterized by considering exponential inhibition by substrate and linear inhibition by product [14]. The Hoppe-Hansford model, shown in (12), considers only linear inhibition by the product.

C. Bayesian Statistic

Bayesian statistics is based on Bayes' theorem on three main steps: using accessible knowledge about a given parameter in a model through the a priori probability distribution; assigning the likelihood function using the parameter information available in the observed data; combining both the a priori probability distribution and the likelihood function into the form of a posteriori probability distribution. The a posteriori probability distribution, as in (19), represents the updated knowledge [15].

$$\pi(P \mid Y) = \frac{\pi(Y \mid P)\pi(P)}{\pi(Y)} \qquad (19)$$

Equation (19) is in terms of P, which can represent unknown parameters and Y which can denote state variables. The function $\pi(P)$ is the a priori probability density, expressing the information of P prior to the measurement of Y; $\pi(Y|P)$ is the likelihood function, expressing the observed probability density of Y knowing P; $\pi(P|Y)$ is the a posteriori probability density function, i.e., the probability density of P given the prior information and the measured value of Y; $\pi(Y)$ is a normalization constant [16–18].

$$\pi(P \mid Y) = \alpha \times \pi(Y \mid P) \times \pi(P) \qquad (20)$$

Equation (19) can also be represented by (20), since $\pi(Y)$ represents a normalization constant. Thus, the a posteriori probability density function can be written as being proportional to the product of the likelihood function and the a priori probability density.

L. A. Guimarães, S. de Aviz Cardoso, D. C. Estumano, and B. M. Viegas,
"Estimation of parameters and state variables in an alcoholic fermentation process in a fed-batch bioreactor",
Latin-American Journal of Computing (LAJC), vol. 10, no. 2, 2023.

TABLE I.   KINETIC MODELS FOR SPECIFIC SPEED OF CELL GROWTH

Classification	Author(s)	Model[a]	
No Inhibition	Monod (1942)	$\mu_X = \mu_{X,max} \dfrac{C_S}{K_S + C_S}$	(5)
	Moser (1958)	$\mu_X = \mu_{X,max} \dfrac{C_S^u}{K_S + C_S}$	(6)
	Contois (1959)	$\mu_X = \mu_{X,max} \dfrac{C_S}{K_S \times C_X + C_S}$	(7)
Substrate inhibition	Andrews (1968)	$\mu_X = \mu_{X,max} \dfrac{C_S}{K_S + C_S + \dfrac{C_S^2}{K_{IS}}}$	(8)
	Wu (1988)	$\mu_X = \mu_{X,max} \dfrac{C_S}{K_S + C_S + \dfrac{C_S^v}{K_{IS}}}$	(9)
Product Inhibition	Aiba – Shoda – Nagatani (1968)	$\mu_X = \mu_{X,max} \dfrac{C_S}{K_S + C_S} e^{(-K_{IP} \times C_P)}$	(10)
	Levenspiel (1980)	$\mu_X = \mu_{X,max} \dfrac{C_S}{K_S + C_S} \left(1 - \dfrac{C_p}{C_{P_{max}}}\right)^n$	(11)
	Hoppe – Hansford (1982)	$\mu_X = \mu_{X,max} \dfrac{C_S}{K_S + C_S} \dfrac{K_{IP}}{K_{IP} + C_P}$	(12)
Cellular Inhibition	Lee – Pollard – Coulman (1983)	$\mu_X = \mu_{X,máx} \dfrac{C_S}{K_S + C_S} \left(1 - \dfrac{C_X}{C_{X_{max}}}\right)^m$	(13)
Hybrid Inhibition	Ghose – Thyagi (1979)	$\mu_X = \mu_{X,max} \dfrac{C_S}{K_S + C_S + \dfrac{C_S^2}{K_S}} \left(1 - \dfrac{C_p}{C_{P_{max}}}\right)$	(14)
	Tosetto	$\mu_X = \mu_{X,max} \dfrac{C_S}{K_S + C_S + \dfrac{C_S^2}{K_S}} \left(1 - \dfrac{C_p}{C_{P_{max}}}\right)^n$	(15)
	Levenspiel/Lee – Pollard – Coulman	$\mu_X = \mu_{X,max} \dfrac{C_S}{K_S + C_S} \left(1 - \dfrac{C_p}{C_{P_{máx}}}\right)^n \left(1 - \dfrac{C_X}{C_{X_{max}}}\right)^m$	(16)
	Andrews/Lee – Pollard – Coulman	$\mu_X = \mu_{X,max} \dfrac{C_S}{K_S + C_S + \dfrac{C_S^2}{K_S}} \left(1 - \dfrac{C_X}{C_{X_{max}}}\right)^m$	(17)
	Andrews/Lee – Pollard – Coulman/Levenspiel	$\mu_X = \mu_{X,max} \dfrac{C_S}{K_S + C_S + \dfrac{C_S^2}{K_S}} \left(1 - \dfrac{C_X}{C_{X_{max}}}\right)^m \left(1 - \dfrac{C_p}{C_{P_{max}}}\right)^n$	(18)

[a.] Kinetic parameters: K_S is the saturation constant, K_{IS} is the substrate inhibition constate, $C_{Pmáx}$ is the product concentration when cell growth ceases, n is the power of the product inhibition term, u is adimensionless parameter of the model, v is a dimensionless parameter of the model, K_{IP} is the product inhibition constant and m is a dimensionless parameter of the model.

In possession of this, a specific strategy that makes it possible to obtain inference by simulation is through the use of Sequential Monte Carlo Methods (SMCs), commonly referred to as particle filters. It provides a computational approximation for the a posteriori distribution, which may be in terms of random samples (particles) and associated weights, being able to predict an unknown variable from a data set [19, 20]. From this perspective, Bayesian filters of the particle filter class are probabilistic methods that rely on a recursive algorithm for estimating and updating dynamic states of a system from models, knowledge bases, and others [21].

Particle filter methods are used in order to produce sequential estimates of the desired dynamic variables. The sequential estimation is done through interleaved prediction and data update steps. This is accomplished in such a way that the error is minimized statistically. Particle filters are traditionally applied with the following algorithms: Sampling Importance Resampling (SIR), Auxiliary Sampling Importance Resampling (ASIR) and Liu and West [20].

In general, simulation methods based on Bayesian sequential analysis of dynamic models initially arise with the proposal to sample the state variables over time using fixed parameters. In such a case, particle "friction" situations are present in resampling-based methods and "weight degeneracy" situations are seen in reweighting–based methods. However, these occurrences are handled by formulating a synthetic method of generating new sample points for parameters by targeting "artificial evolution", in which the non-dependence of parameters with time is still considered [9].

Additionally, the phenomenon of degeneracy occurs because many particles have insignificant weights. More computational effort is required so that particles with small weights can be advanced in time in the same way as large particles. The problem can be minimized by increasing the number of particles, and more efficiently, the resampling technique can be applied in order to select the best particles. The SIR and ASIR algorithms contain resampling steps [9, 20].

Although resampling reduces the effects of degeneracy this can lead to a loss of diversity and the resulting sample may contain a large amount of repeated particles, causing the sample to be impoverished. This is a serious situation in state evolution models with small noises. In this case, the "collapse", or "friction", of all particles into a single particle occurs, especially when there are small time intervals. The ASIR method is qualified to solve this problem [9, 20].

Still, Liu and West present an innovation to use the ASIR algorithm proposing to show how to estimate, besides the state variables, the parameters of the model. Similarly to the state variables, the parameters are updated, or evolved, at each time and this procedure is performed through a combination between the average for all particles and the parameter value for each particle [20].

In the Bayesian view, filter-based sequential simulation using an Auxiliary Particle Filter (APF) that incorporates state variables and parameters has excellent equivalence to Markov chain Monte Carlo (MCMC) analysis. Liu and West demonstrated this by applying and comparing them from a dynamic factor financial model, inherent in the banking industry, to obtain perspectives on a time scale beyond the data set. In this respect, the feasibility of sequential simulation-based filtering induced approximation errors that indicated a tendency to increase over time. In other words, in an analysis it would be convenient to restrict oneself to short time scales because observing a very long horizon increased the possibility of being unrealistic. As a solution, it was proposed to use a longer historical stretch of data and, mainly, it was suggested that methods should always be combined with some form of periodic recalibration based on off-line analysis [9].

D. Simulation of alcoholic fermentation

The analysis of the experimental data aimed to evaluate the kinetic behavior of the state variables and parameters defined in (21–23).

$$X = [C_X, C_S, C_P, V] \qquad (21)$$

$$P_{Tosetto} = f(F, \mu_{max}, K_S, K_{IP}, Y_{X/S}, Y_{P/S}) \qquad (22)$$

$$P_{Hoppe-Hansford} = f(F, \mu_{max}, K_S, K_{IS}, Y_{X/S}, Y_{P/S}, n, C_{P_{max}}) \qquad (23)$$

The case study estimates of the state variables and parameters were designed using the mathematical modeling of the fermentation simultaneously with the data acquired from the experimental measurements of Borges (2008) [22]. More precisely, they were performed based on the fed-batch fermentation operation in three experimental conditions, named in this paper as FB1, FB2 and FB3. The design parameters and initial conditions are presented in Tables II and III, respectively. Where, t is the fermentation time and t_F is the feeding time, both in hours (h).

The measurements of the state variables are in Table IV–VI, and the already estimated parameter values are shown in Table VII. The values of the experimental measurements, obtained by using a temperature (T) of 32°C, of C_X, C_S, C_P (g.L^{-1}) and V (L) over time (h). In the experimental conditions, C_X is the dry biomass of *Saccharomyces cerevisiae* yeast, C_S is the sucrose concentration,, C_P is the ethanol concentration and V is the verified volume in the bioreactor [22].

TABLE II.   DESIGN PARAMETER VALUES

Data[b]	C_{SF} (g.L^{-1})	t (h)	t_F (h)
FB1	217	8	5.283
FB2	241.4	10	5.217
FB3	285	11	5.2

[b.] Values obtained from [22].

TABLE III.   INITIAL VALUES OF THE STATE VARIABLES USED IN THE ALCOHOLIC FERMENTATION PROCESS

Data[c]	C_X (g.L^{-1})	C_S (g.L^{-1})	C_P (g.L^{-1})	V (L)
FB1	88	0	35.17	1.5
FB2	83	0	36.71	1.5
FB3	83	0	36.78	1.5

[c.] Values obtained from [22].

TABLE IV.   EXPERIMENTAL MEASUREMENTS FOR THE FED-BATCH PROCESS (FB1) WITH C_{SF} = 217 G.L^{-1}

t (h)[d]	C_X (g.L^{-1})[d]	C_S (g.L^{-1})[d]	C_P (g.L^{-1})[d]	V (L)[d]
0	88.0	0	35.17	1.500
1	59.0	29.0	42.6	2.116
2	46.6	34.0	47.8	2.820
3	38.2	36.0	52.6	3.479
4	33.1	39.0	55.0	4.139
5.283	27.7	35.8	58.89	4.986
6	28.7	19.85	68.0	4.986
7	29.7	5.2	74.7	4.986
8	29.7	0.894	77.6	4.986

[d.] Values obtained from [22]

L. A. Guimarães, S. de Aviz Cardoso, D. C. Estumano, and B. M. Viegas,
"Estimation of parameters and state variables in an alcoholic fermentation process in a fed-batch bioreactor",
Latin-American Journal of Computing (LAJC), vol. 10, no. 2, 2023.

TABLE V.   EXPERIMENTAL MEASUREMENTS FOR THE FED-BATCH PROCESS (FB2) WITH C_{SF} = 241,4 G.L^{-1}.

t (h)[e]	C_X(g.L^{-1})[e]	C_S (g.L^{-1})[e]	C_P(g.L^{-1})[e]	V (L)[e]
0	83.0	0	36.71	1.500
1	56.0	40.0	41.8	2.168
2	44.1	53.0	47.8	2.837
3	36.3	58.11	49.6	3.505
4	31.0	56.0	51.7	4.174
5.217	26.5	64.1	55.3	4.987
6	26.8	40.0	60.4	4.987
7	27.4	21.2	69.94	4.987
8	27.5	8.0	78.2	4.987
9	28.3	2.8	80.4	4.987
10	28.4	0.899	81.2	4.987

e. Values obtained from [22]

TABLE VI.   EXPERIMENTAL MEASUREMENTS FOR THE FED-BATCH PROCESS (FB2) WITH C_{SF} = 285 G.L^{-1}

t (h)[f]	C_X(g.L^{-1})[f]	C_S (g.L^{-1})[f]	C_P(g.L^{-1})[f]	V (L)[f]
0	83	0	36.78	1.5
1	54	51.8	43.3	2.17
2	44	66.7	47.3	2.84
3	36.6	80	49.3	3.51
4	30.6	82	53.8	4.181
5.2	26.3	88	53.82	4.985
6	26.8	66	65.7	4.985
7	27	44	70.77	4.985
8	27.1	28.3	82.1	4.985
9	27.7	18.4	85.8	4.985
10	27.8	9.8	89.3	4.985
11	28.1	4.57	91.5	4.985

f. Values obtained from [22]

TABLE VII.   VALUES OF THE YIELD COEFFICIENTS, GENERAL KINETIC PARAMETERS, AND KINETIC PARAMETERS FOR THE TOSSETTO AND HOPPE – HANSFORD MODELS

Parameters	Values		
Yield coefficients[g]	FB1	FB2	FB3
$Y_{X/S}$	0.024	0.021	0.017
$Y_{P/S}$	0.445	0.418	0.413
Flow rate[g]	FB1	FB2	FB3
F	0.660	0.668	0.670
General kinetic parameters[g]	FB1	FB2	FB3
μ_{max}	0.02686	0.02293	0.02701
K_S	10.40	10.31	32.02
Kinetic parameters for Tosseto model[g]	FB1	FB2	FB3
K_{IS}	813.8	693.4	370.0
$C_{Pmáx}$	125.7	129.9	144.1
N	0.1	0.1	0.2861
Kinetic parameters for Hoppe– Hansford model[h]	FB1	FB2	FB3
K_{IP}	200	200	200

g. Values obtained from [22].

h. Abitrarily chosen value.

The deviation used for the experimental measurements was 1% from the maximum concentration value. The estimation results were presented in terms of the 99% confidence interval with 500 particles for Liu and West's algorithm.

E. Statistical analysis

The models were statistically analyzed with the coefficient of determination (R^2), by which the simulation data of the state variables were compared with the experimental data set.

III. RESULTS

A. Estimation of the state variables
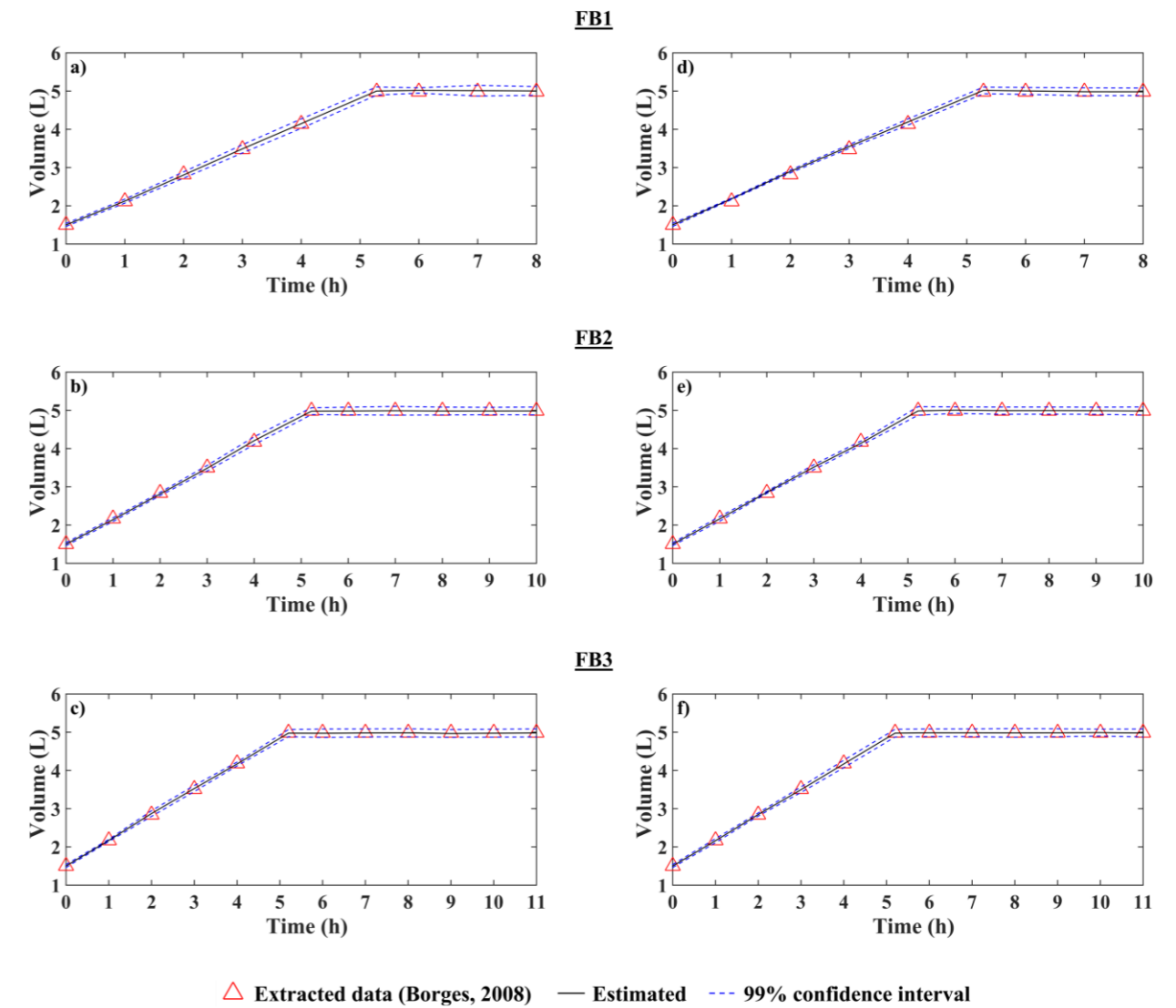
Fig. 1. Obtaining the volume variations (V) by applying the Liu and West filter. (a–c) Tosetto model for μ_X. (d–f) Hoppe–Hansford model for μ_X.

L. A. Guimarães, S. de Aviz Cardoso, D. C. Estumano, and B. M. Viegas,
"Estimation of parameters and state variables in an alcoholic fermentation process in a fed-batch bioreactor",
Latin-American Journal of Computing (LAJC), vol. 10, no. 2, 2023.

Fig. 2. Obtaining the variations of cell concentrations (C_X) – *Saccharomyces cerevisiae* – by applying the Liu and West filter. (a–c) Tosetto model for μ_X. (d–f) Hoppe–Hansford model for μ_X.

Fig. 3. Obtaining the variations of the concentrations of substrate (C_S) – Sucrose – by applying the Liu and West filter. (a-c) Tosetto model for μ_X. (d–f) Hoppe–Hansford model for μ_X.
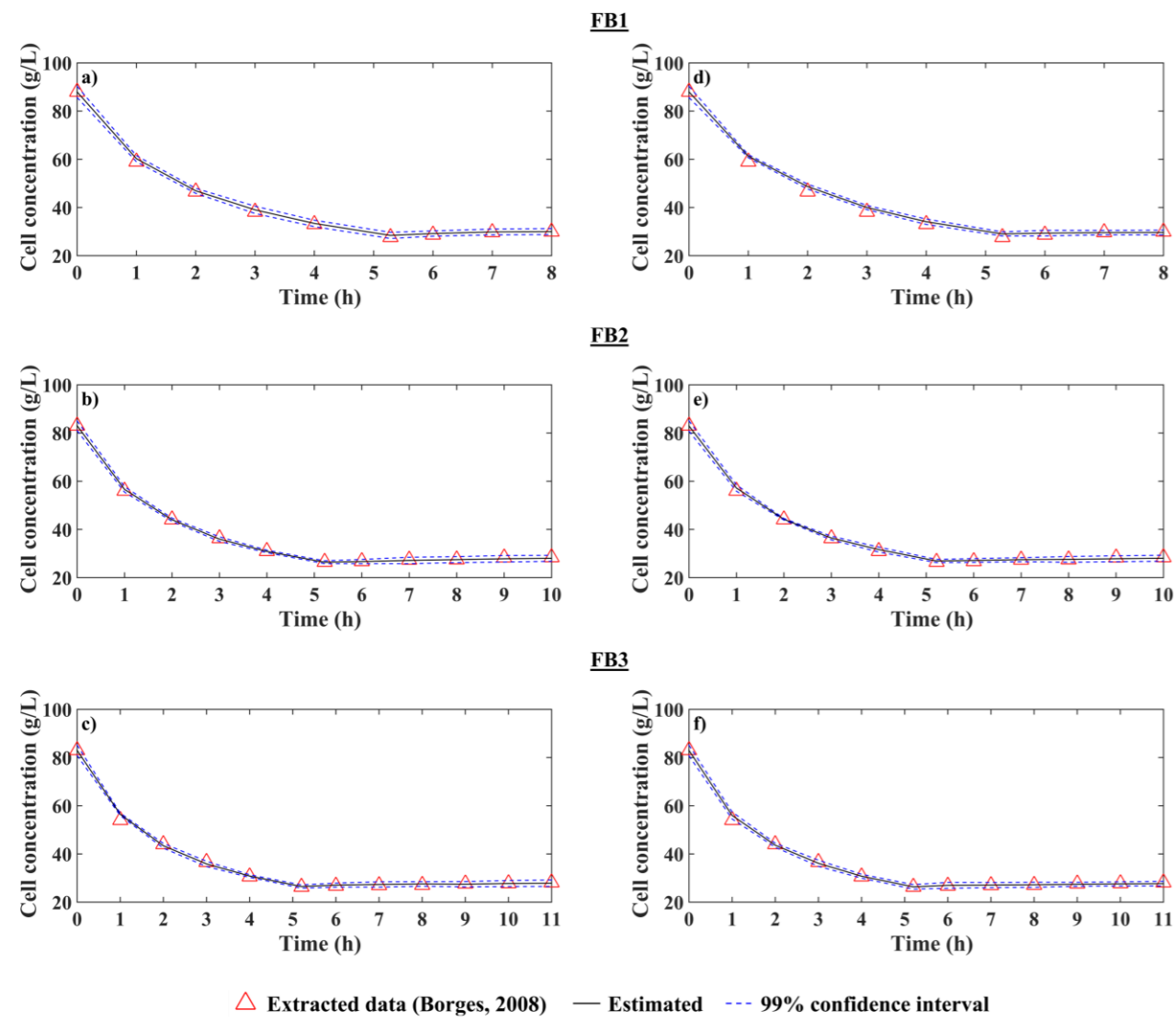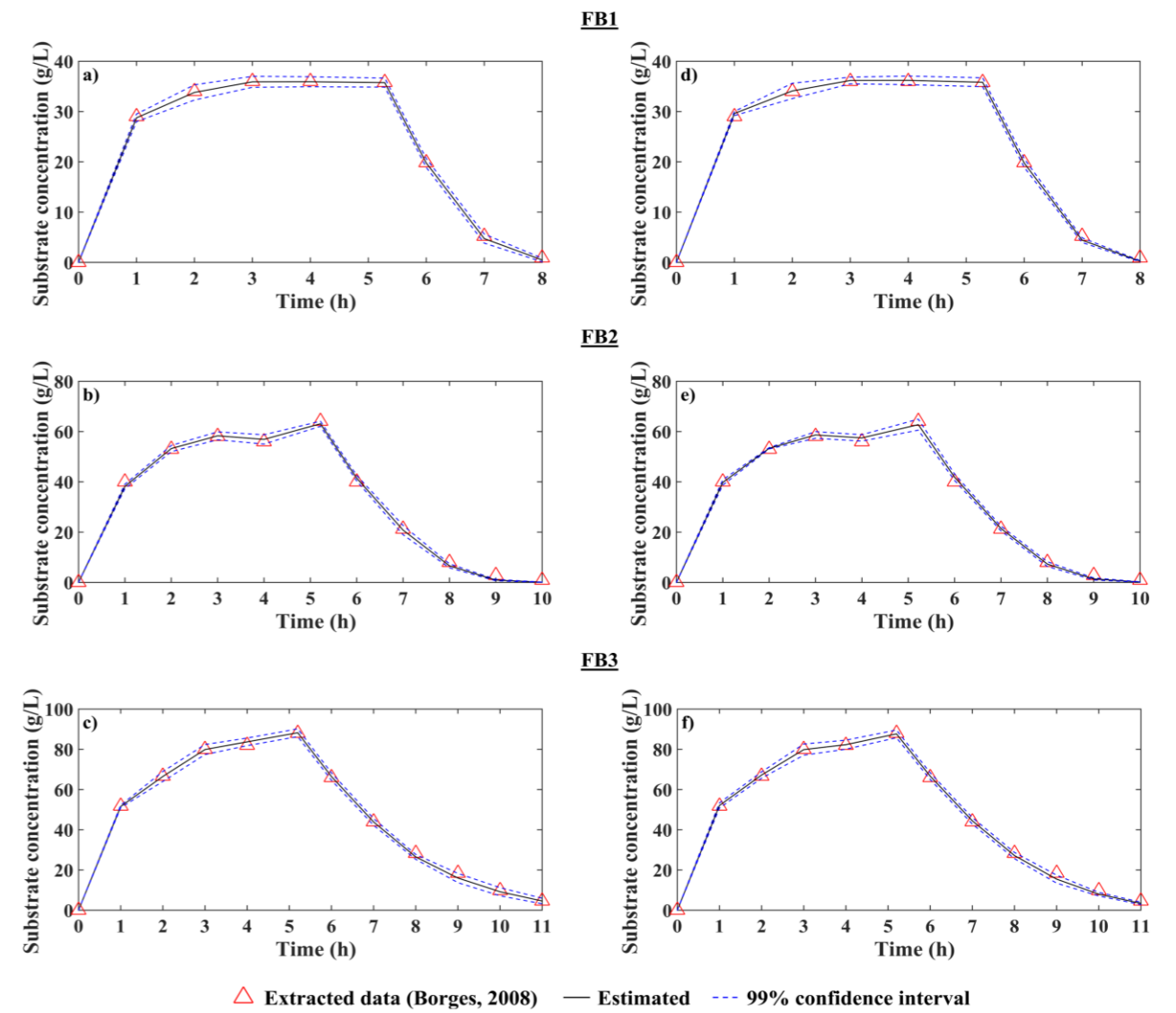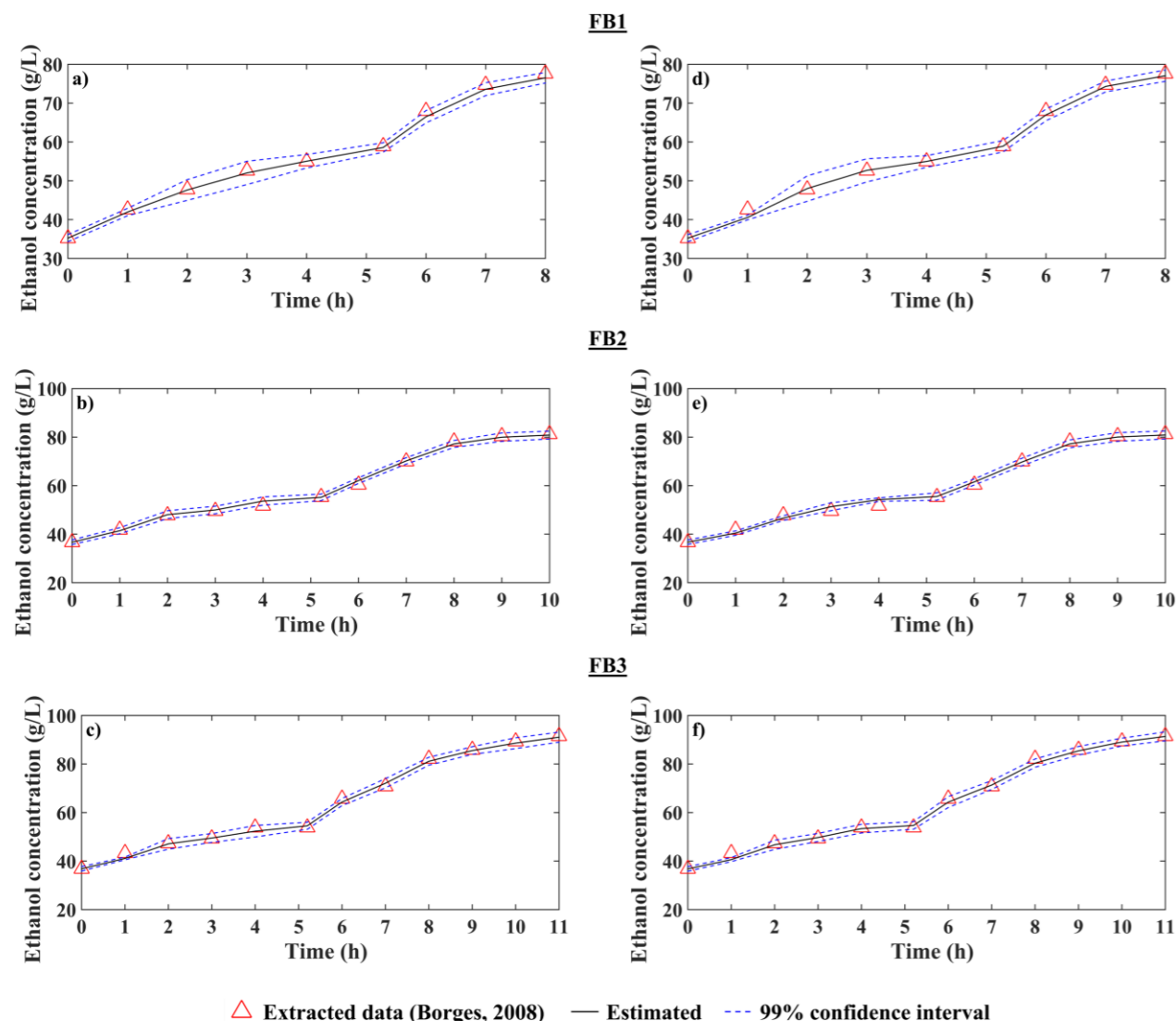
Fig. 4. Obtaining the product concentration variations (C_P) – Bioethanol – by applying the Liu and West filter. (a–c) Tosetto model for μ_X. (d–f) Hoppe–Hansford model for μ_X.

The evolution of the system volume is seen in Fig. 1, where a linear profile is observed during the process of feeding the medium, characteristic of the constant feed flow rate. The total volume becomes constant when the substrate feeding is interrupted.

In Fig. 2, we can see the immediate effects of the substrate-feeding step where initially there is a decrease in cell concentration due to the increase in the volume of the medium and the subsequent stability caused by reaching a constant system volume.

The results for substrate concentration are shown in Fig.3. It is verified that the concentration presents an increase until the time of about 5 hours (end of substrate feeding), followed by a decrease related to its consumption by the yeast cells present in the medium. Consequently, a gradual increase in ethanol production occurs during the fermentation process, as seen in Fig. 4. That is in agreement with what the literature propounds [23], in which ethanol production occurs simultaneously with yeast growth (biomass formation) because it is associated with the energy metabolism of the cell.
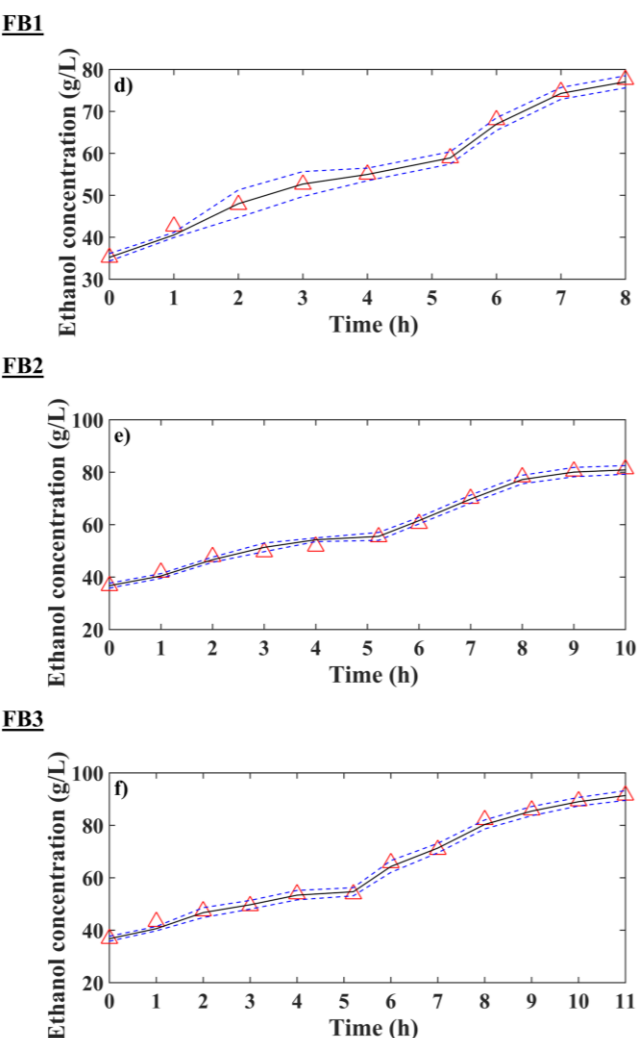
B. Kinetic parameters estimation

From the application of the particle filter, new values for the parameters were found for the proposed cases, as presented in Table VIII. Despite the differences in the experimental conditions, mainly referring to the C_{SF}, the yield coefficients and the kinetic parameter μ_{max} showed stable values. While the other parameters values showed a larger difference.

TABLE VIII. UPDATE PARAMETERS VALUES

Parameters	Values					
	Tosetto			Hoppe – Hansford		
Yields coefficients	FB1	FB2	FB3	FB1	FB2	FB3
$Y_{X/S}$	0.0213	0.0184	0.0211	0.0264	0.0230	0.0198
$Y_{P/S}$	0.4155	0.4002	0.4015	0.4402	0.3994	0.3872
Flow rate	FB1	FB2	FB3	FB1	FB2	FB3
F	0.5287	0.7024	0.8052	0.6478	0.5838	0.889
General kinetic parameters	FB1	FB2	FB3	FB1	FB2	FB3
μ_{max}	0.0233	0.0215	0.0303	0.0328	0.0313	0.0285
K_S	12.086	11.528	24.982	7.46111	12.754	24.496
Kinetic parameters for Tosseto model	FB1	FB2	FB3	FB1	FB2	FB3
K_{IS}	794.88	611.09	525.68			
$C_{Pmáx}$	194.29	141.80	92.793			
N	0.0759	0.1061	0.1620			
Kinetic parameters for Hoppe–Hansford model	FB1	FB2	FB3	FB1	FB2	FB3
K_{IP}				207.62	199.89	191.13

C. Statistical Analysis

TABLE IX. CORRELATION COEFFICIENTS (R^2) OF THE SIMULATION THROUGH LIU AND WEST FILTER.

Data	State variable	Kinectics models	
		Tosetto	Hoppe-Hansford
FB1	C_X	0.99902	0.99504
	C_S	0.99974	0.99925
	C_P	0.99665	0.99648
	V	0.99983	0.99868
	Average	**0.99881**	**0.99736**
FB2	C_X	0.99967	0.99922
	C_S	0.99788	0.99830
	C_P	0.99664	0.99394
	V	0.99983	0.99988
	Average	**0.99851**	**0.99784**
FB3	C_X	0.99766	0.99851
	C_S	0.99888	0.99859
	C_P	0.99682	0.99652
	V	0.99988	0.99997
	Average	**0.99831**	**0.99840**

The percent accuracy of the results with μ_X kinetic model by Tosetto was 99.83 – 99.88% and the best accuracy was for condition FB1 (lowest value of C_{SF} and C_P). In the other conditions, the value of the estimated data was decreasing but still with very good accuracy.

For the kinetic model of μ_X by Hoppe–Hansford the range was 99.74 – 99.84%. The best accuracy in this case was for the FB3 data (highest value of C_{SF} e C_P), it was also observed that the accuracy of the simulation was increasing and proportional to the increase in C_P, which confirms the potential of using the model to represent inhibition by the product

IV. CONCLUSION

In this study, mathematical modeling and simulation were performed to represent the alcoholic fermentation kinetics. Using the particle filter method of Liu and West, it was possible to perform the estimates of the state variables and parameters of the alcoholic fermentation process based on three experimental conditions. The applied technique showed good agreement in the estimation of all experimental conditions.

It was possible to verify the inhibition performance by the Tosetto and Hoppe–Hansford specific cell growth rate models. In this respect, the hybrid inhibition by the presence in excess of substrate and product considered by Tosetto fitted the data slightly better, although both models were 99% accurate.

The results obtained made important contributions to research involving fermentation kinetics and computational applications. Since, with the use of the mathematical models combined with the particle filter of Liu and West (2001), one can see the effectiveness of the application of this method and the potential incorporation into methodologies aimed at greater efficiency in bioethanol production, as well as in other fermentative processes.

References

[1] K. A. Gray, L. Zhao, and M. Emptage, "Bioethanol," *Current Opinion in Chemical Biology*, vol. 10, no. 2, pp. 141–146, 2006.

[2] P. M. Doran, "Bioprocess Development: An Interdisciplinary Challenge," in *Bioprocess Engineering Principles*, Waltham, MA: Academic Press, 2013, ch. 1, pp. 3-11.

[3] W. Schmidell and M.C.R. Facciotti, "Biorreatores e processos fermentativos," in *Biotecnologia industrial: Engenharia bioquímica*, vol. 2, W. Schmidell, U. A. Lima, E. Aquarone, W. Borzani, Eds., São Paulo, 1st ed, São Paulo, BR: Edgard Blücher, 2001,ch. 8, pp. 179–192.

[4] H. Hiss, "Cinética do processos fermentativos," in *Biotecnologia industrial: Engenharia bioquímica*, vol. 2, W. Schmidell, U. A. Lima, E. Aquarone, W. Borzani, Eds., 1st ed, São Paulo, BR: Edgard Blücher, 2001,ch. 6, pp. 93–122.

[5] L. C. Basso, S. N. Rocha, and T. O. Basso, "Ethanol Production in Brazil: The Industrial Process and Its Impact on Yeast Fermentation," in *Biofuel Production-Recent Developments and Prospects*, INTECH Open Access Publisher, 2011, pp. 85–100.
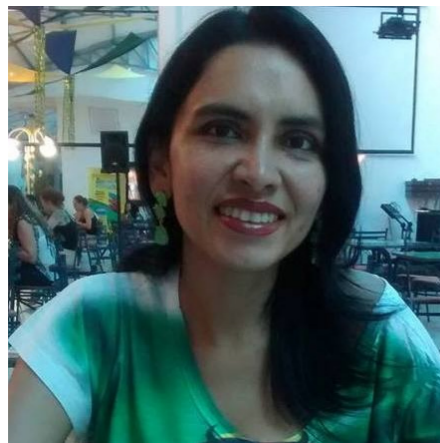
[6]   I. I. K. Veloso, "Modelagem e otimização da fermentação alcoólica em batelada alimentada a baixa temperatura," M.S. thesis, Dept. of Chem. Eng., Federal Univ. of São Carlos, São Carlos, SP, 2019.

[7]   N. Pereira Junior, E.P.S. Bom and M.A. Ferrara, "*Bioprocessos,*" in Tecnologia de Bioprocessos (Séries em Biotecnologia vol. 1), Rio de Janeiro, BR: Amiga Digital, 2008, ch. 2, pp. 18-20.

[8]   A. Bonomi and W. Schmidell, "Modelagem matemática e simulação de processos fermentativos," in *Biotecnologia industrial: Engenharia bioquímica*, vol. 2, W. Schmidell, U. A. Lima, E. Aquarone, W. Borzani, Eds., 1st ed., São Paulo, BR: Edgard Blücher, 2001, ch. 7, pp. 123–178.

[9]   J. Liu and M. West, "Combined parameter and state estimation in simulation-based filtering,". In: A. Doucet, N. de Freitas and N. Gordon, Eds.,*Sequential Monte Carlo Methods in Practice* (Statistics for Engineering and Information Science), New York, US: Springer, 2001, pp. 197–223.

[10]   P. M. Doran, "Material Balances," in *Bioprocess Engineering Principles*, Waltham, MA: Academic Press, 2013, ch. 4, pp. 87–91.

[11]   H. Hiss, "A cinética de inibição do crescimento," in *Cinética de fermentações-Uma análise matemática da atividade microbiana*, 1st ed., BR : Clube de Autores, 2013, ch. 4, pp. 306–394.

[12]   G. M. Tosetto, "Influência da matéria-prima no comportamento cinético de levedura na produção de etanol," M.S. thesis, Dept. of Biotechnological Processes, State Univ. of Campinas , Campinas, SP, 2002.

[13]   T. K. Ghose and R. D. Thyagi, "Rapid ethanol fermentation of cellulose hydrolysate,". II. product and Substrate Inhibition and Optimization of Fermentor Design. *Biotechnology and Bioengineering*, v. 21, no. 8, pp. 1401-1420, 1979.

[14]   G. K. Hoppe and G. S. Hansford, "Ethanol inhibition of continuous anaerobic yeast growth," *Biotechnology Letters*, vol. 4, no. 1, pp. 39–44, 1982.

[15]   R. Van De Schoot *et a*l., "Bayesian statistics and modelling," *Nature Reviews Methods Primers*, vol. 1, no. 1, 2021.

[16]   J. V. Beck and K. J. Arnold, "*Parameter estimation in engineering and science,*" John Wiley & Sons, New York, U.S., 1977.

[17]   J. Kaipio and E. Somersalo, "Statistical inverse problems: discretization, model reduction and inverse crimes,". *Journal of computational and applied mathematics*, v. 198, no. 2, pp. 493-504, jan. 2007.

[18]   B. M. Viegas, E. M. Magalhães, H. R. B. Orlande, D. C. Estumano and E. N. Macêdo, "Experimental study and mathematical modelling of red mud leaching: application of Bayesian techniques*,"*. *International Journal of Environmental Science and Technology*, v. 20, pp. 5533-5546, 2023.

[19]   T. G. Martins, "Aproximações determinısticas para distribuições a posterirori marginais," M.S, thesis, Dept. of Statistical Methods. , Federal Univ. of Rio de Janeiro, Rio de Janeiro, RJ, 2010.

[20]   D. C. Estumano, "Estimativa de parâmetros e variáveis de estado de modelos aplicados à neurônios citomegálicos utilizando dados experimentais do protocolo de tensão fixa," Ph.D. dissertation, Graduate Program in Mech. Eng., Federal Univ. of Rio de Janeiro, Rio de Janeiro, RJ, 2016.

[21]   W. Betencurte Da Silva, "Aplicação de filtros de partículas para a assimilação de dados em problemas de fronteira móvel," Ph.D. dissertation, Graduate Program in Mech. Eng., Federal Univ. of Rio de Janeiro, Rio de Janeiro, RJ, 2012.

[22]   P. C. S. Borges, "Otimização dinâmica da fermentação alcoólica no processo em batelada alimentada," M.S. thesis, Graduate Program in Chem. Eng., Federal Univ. of Uberlândia, Uberlândia, MG, 2008.

[23]   U. A. Lima, L. C. Basso and H. V. Amorim, "Produção de etanol," in *Biotecnologia industrial: Processos Fermentativos e Enzimáticos*, vol. 3, U. A. Lima, E. Aquarone, W. Borzani, W. Schmidell, Eds., São Paulo, 1st ed., BR: Edgard Blücher, 2001, ch. 1, pp. 1–43.

AUTHORS

Lucas Guimarães

Undergraduate student in Bioprocess Engineering at the Federal University of Pará (UFPA). Has experience with mathematical modeling and simulation of fermentative processes. Worked in offering workshops on algorithms and initiation to programming for high school students.

Diego Cardoso

Graduated in Chemical Engineering from the Federal University of Pará (2010), master's degree in Mechanical Engineering from the Federal University of Rio de Janeiro (2012) and Ph.D. in Mechanical Engineering from the Federal University of Rio de Janeiro (2016). He is currently an Adjunct Professor at the Federal University of Pará working in the Faculty of Biotechnology and in the Graduate Programs of Chemical Engineering (PPGEQ). His main line of research is the application of Bayesian techniques in estimating parameters and state variables. He already has experience applying these techniques in models applied in the following areas: bioengineering, reactors, mass transfer, heat transfer and adsorption.

Simone Cardoso

Degree in Chemical Engineering from the Federal University of Pará in 2004, and a Master's degree in Chemical Engineering from the Federal University of Pará in 2007 at the PPEQ (Postgraduate Program in Chemical Engineering) and a PhD in Natural Resources Engineering from the Federal University of Pará in 2010 at PRODERNA (Doctoral Program in Engineering of Natural Resources in the Amazon). She is currently a professor at the Federal University of Pará at the Faculty of Biotechnology of the Institute of Biological Sciences since 2011. Currently, she develops work in the area of biogas, modeling and simulation of bioprocesses, waste treatment and the environment, and also develops and coordinates projects of environmental and educational extension.

Bruno Marques Viegas

Graduated (2014) and Master's (2016) in Chemical Engineering from the Federal University of Pará. PhD (2019) in Natural Resources Engineering from the Federal University of Pará. He is currently an adjunct professor at the Faculty of Biotechnology and Coordinator of the Biotechnology Course (ICB / UFPA). Its main areas of expertise are: Waste Treatment and Use, Bioreactors, Hydrometallurgy and Inverse Problems.

Deflection Analysis of Beams from Vehicle Velocity

Werley Rafael da Silva
Instituto de Física - PPGCET
Universidade Federal de Catalão
Catalão, Brasil
werleyrafael2@gmail.com
ORCID: 0009-0004-1451-8182

Victor Henrique Rocha
Instituto de Física - PPGCET
Universidade Federal de Catalão
Catalão, Brasil
victor@vhrocha.com.br
ORCID: 0000-0003-4981-8834

Renato Alejandro Tintaya Mollo
Instituto de Matemática e
Estatistica - IMTec
Universidade Federal de Catalão
Catalão, Brasil
renato.atm@ufcat.edu.br
ORCID: 0000-0002-79353305

Marcos Napoleão Rabelo
Instituto de Matemática e
Estatistica - IMTec
Universidade Federal de Catalão
Catalão, Brasil
marcosrabelo@ufcat.edu.br
ORCID: 0000-0002-4205-4651

Deflection Analysis of Beams from Vehicle Velocity

Werley Rafael da Silva
Instituto de Física - PPGCET
Universidade Federal de Catalão
Catalão, Brasil
werleyrafael2@gmail.com
ORCID: 0009 0004 1451 8182

Victor Henrique Rocha
Instituto de Física - PPGCET
Universidade Federal de Catalão
Catalão, Brasil
victor@vhrocha.com.br
ORCID: 0000 0003 4981 8834

Renato Alejandro Tintaya Mollo
Instituto de Matemática e
Estatistica - IMTec
Universidade Federal de Catalão
Catalão, Brasil
renato.atm@ufcat.edu.br
ORCID: 0000 0002 79353305

Marcos Napoleão Rabelo
Instituto de Matemática e
Estatistica - IMTec
Universidade Federal de Catalão
Catalão, Brasil
marcosrabelo@ufcat.edu.br
ORCID: 0000 0002 4205 4651

Abstract—In this work, the modeling and calculations referring to the deflection of special artworks are presented. The type train is modeled as two degrees of freedom and mobile base, with the bridge deck being considered the mobile base. The base is treated as an elastic beam, according to the Euler-Bernoulli theory. The fundamental assumption made is that the relative displacements between the vehicle and the bridges are synchronous. This allows the calculation of natural frequencies, eigenvalues and normal modes of vibration of the beam. The temporal response of the beam deflection is obtained, assuming that the vehicle employs, at each instant of time, an impulse load on the beam. Numerical simulations are performed to improve the understanding of the dynamic behavior of the structure.

Keywords—Vehicle-bridge interaction (VBI), Bridge dynamics, Bridge deflection.

I. INTRODUCTION

Due to their great importance, large structures known as Special artworks, such as bridges and viaducts, must have their performance monitored periodically. This is because large structures have a small margin for safety estimates. When it comes to bridges and viaducts, factors such as structural access make it impossible to diagnose the conditions of use, therefore, when a bridge requires interdiction for maintenance or recovery, the impacts on society are considerable, from the creation of large traffic jams, deviations of long journeys or even structural collapse.

Stimuli caused by heavy vehicles cause vibrations that can significantly affect structural integrity. One way to understand the behavior of structures subject to vibrations is to describe a correct modeling based on the boundary conditions defined in the project. In this context, studies aimed at obtaining a structural response have gained strength in recent years. Research involving numerical models for vehicle-bridge interaction analysis can be seen in Zou *et al.* [1]; Yang and Lin [2] and Zhu and Law [3]. Eigenvalues and eigenfunctions problems for bridges idealized as Euler-Bernoulli beams were studied in Hayashikawa and Watanabe [4]. In Matsuoka and

Tanaka´s [5] work, a new method for estimating bridge deflection based on track irregularities, measured by a moving train, was studied. efficient according to the authors. In Corbally and Malekjafariam [6], a new approach is proposed that introduces the concept of operational deflection shape ratios from the measured responses in two axes of a bridge segment. Other results related to the dynamic analysis of structures can be detailed in Kwon *et al.* [7]; Yang *et al.* [8]; Meyer *et al.* [9].

In this approach, the main physical variable to be measured is displacement. For this measurement, the displacement field is seen as a response to excitation suffered by the structure. In the case of special artworks, the main excitations are the dynamic loads generated by the flow of vehicles, in this context the objective of the work is to present a model of dynamic analysis of structures, idealized as beams traveled by a train-type with constant speed.

II. METHODOLOGY

Special artworks are modeled as beams. The equations of motion that describe the behavior of the structure as well as its initial and boundary conditions can be derived from Hamilton's generalized variational principle. To obtain the energy functional, the Euler-Bernoulli theory is employed. According to this theory the main hypothesis is that the effects of rotation of the cross section, constant, is disregarded when compared with the translational displacement. Furthermore, the shear strain is disregarded when compared with the bending strain. It should also be noted that the present methodology is applied when the thickness of the beam is small, around ten times, when compared to its length. It is also considered that the deformations due to bending are small when compared to the length of the structure. So, in this context, evaluating that the vertical displacement of the beam is $w(x,t)$, the displacement field is:

$$u = -z\partial_x w(x,t), \ v = 0, \ w = w(x,t). \tag{1}$$

The deformation components, referring to the displacements defined in (1) are:

$$\varepsilon_{xx} = \partial_x u = -z\partial_{xx} w, \ \varepsilon_{yy} = \varepsilon_{zz} = \varepsilon_{xy} = \varepsilon_{yz} = \varepsilon_{xx} = 0, \tag{2}$$

$$\varepsilon_{xx} = \partial_x u = -z\partial_{xx} w, \ \varepsilon_{yy} = \varepsilon_{zz} = \varepsilon_{xy} = \varepsilon_{yz} = \varepsilon_{xx} = 0. \tag{3}$$

The strain energy for ε_{xx}, denoted by U, can be expressed as:

$$U = \frac{1}{2}\int_0^L EI(\partial_{xx} w)dx + \frac{1}{2}\Big[k_1 w(0,t)^2 + k_{t_1}\partial_x w(0,t)^2 \dots$$
$$\dots + k_2 w(L,t)^2 + k_{t_2}\partial_x w(L,t)^2\Big], \tag{4}$$

where the second term on the right side of (4) represents the deformation, translational and rotational energy of the spring and I denotes the moment of inertia of the cross section of the beam about axis y,

$$I_y = \iint_A z^2 dA. \tag{5}$$

The kinetics energy is given by:

$$T = \frac{1}{2}\int_0^L \rho A\partial_t w^2 dx + \frac{1}{2}\Big[m_1\partial_t w(0,t)^2 + m_2\partial_t w(L,t)^2\Big]. \tag{6}$$

In (6) the first term on the right side represents the kinetic energy of the beam, and the second term indicates the kinetic energy of masses coupled to the beam contours. The work done by the transverse distributed loading $f(x,t)$ is given by:

$$W = \int_0^L fwdx. \tag{7}$$

By Hamilton's generalized variational principle, we obtain the differential equation of transverse motion of the beam

$$\partial_{xx}(EI\partial_{xx} w) + \rho A\partial_u w = f(x,t) \tag{8}$$

with the following board conditions:

$$\left(-EI\partial_{xx} w + k_{t_1}\partial_x w\right)\delta(\partial_x w)\Big|_{x=0} = 0, \tag{9}$$

$$\left(EI\partial_{xx} w + k_{t_2}\partial_x w\right)\delta(\partial_x w)\Big|_{x=L} = 0, \tag{10}$$

$$\left(\partial_x(EI\partial_{xx} w) + k_1 w + m_1\partial_u w\right)\delta w\Big|_{x=0} = 0, \tag{11}$$

$$\left(-\partial_x(EI\partial_{xx} w) + k_2 w + m_2\partial_u w\right)\delta w\Big|_{x=L} = 0. \tag{12}$$

The equations in (9) imply the following board conditions. In $x = 0$:

$$\partial_x w = \text{constant} \mid \delta(\partial_x w) = 0 \text{ or}$$
$$\left(-EI\partial_{xx} w + k_{t_1}\partial_x w\right) = 0 \tag{13}$$

and

$$w = \text{constant} \mid \partial(\partial_x w) = 0 \text{ or}$$
$$\left(\partial_x(EI\partial_{xx} w) + k_1 w + m_1 + \partial_u w\right) = 0 \tag{14}$$

In $x = L$,

$$\partial_x w = \text{constant} \mid \delta(\partial_x w) = 0 \text{ or}$$
$$\left(EI\partial_{xx} w + k_{t_2}\partial_x w\right) = 0 \tag{15}$$

e

$$w = \text{constant} \mid \partial w = 0 \text{ or}$$
$$\left(-\partial_x(EI\partial_{xx} w) + k_2 w + m_2\partial_u w\right) = 0. \tag{16}$$

For free vibrations, it is assumed that the external excitation is zero:

$$f(x,t) = 0, \tag{17}$$

therefore, the equation of motion, (8), reduces to:

$$\partial_{xx}(EI\partial_{xx} w) + \rho A\partial_u w = 0. \tag{18}$$

For beams made of uniform, E constant material and A constant cross-sectional area, (2) can be expressed as:

$$c\partial_{xxxx} w(x,t) + \partial_u w(x,t) = 0, \tag{19}$$

where

$$c = \sqrt{\frac{EI}{\rho A}}. \tag{20}$$

The methodology for solving the free frequencies is based on solving the eigenvalues and eigenfunctions of the problem (19) that can be found using the method of separation of variables as:

$$w(x,t) = W(x)T(t). \tag{21}$$

replacing (21) in (19) we have:

$$\frac{c^2}{W(x)}\frac{d^4W(x)}{dx^4} = -\frac{1}{T(t)}\frac{d^2T(t)}{dt^2} = \omega^2. \tag{22}$$

Equation (22) can be decomposed into the set of two equations:

$$\frac{d^4W(x)}{dx^4} - \beta^4W(x) = 0, \tag{23}$$

$$\frac{d^2T(t)}{dt^2} + \omega^2 T(t) = 0, \tag{24}$$

where

$$\beta^4 = \frac{\omega^2}{c^2} = \frac{\rho A\omega^2}{EI}. \tag{25}$$

LATIN-AMERICAN JOURNAL OF COMPUTING (LAJC), Vol X, Issue 2, July 2023

W. Da Silva, V.Rocha, R. Tintaya, Ma. Rabelo,
"Deflection Analysis of Beams from Vehicle Velocity",
Latin-American Journal of Computing (LAJC), vol. 10, no. 2, 2023.

The solution of (25) is given by:

$$T(t) = A\cos(\omega t) + B\sin(\omega t), \qquad (26)$$

where A and B are constants found from the initial conditions of the problem. The solution of (23) is provided by means of an exponential form:

$$W(x) = C\exp(sx), \qquad (27)$$

where and are constants. Replacing (27) into (23) we get the auxiliary equation:

$$s^4 - \beta^4 = 0, \qquad (28)$$

whose square are given by:

$$s_{1,2} = \pm\beta, \quad s_{3,4} = \pm i\beta. \qquad (29)$$

So, the solution of (23) can be expressed as:

$$W(x) = C_1\exp(\beta x) + C_2\exp(-\beta x) + C_3\exp(i\beta x) + C_4\exp(-i\beta x) \qquad (30)$$

where $C_i, i = 1,\ldots,4$, are constants. It follows from (25) that the natural frequencies of the beam can be determined as:

$$\omega = \beta\sqrt{\frac{EI}{\rho A}}. \qquad (31)$$

The function $W(x)$ is known as the normal mode of vibration of the structure, characteristic function or even eigenfunction associated with the problem (23). For any type of beam, there will be an infinite number of eigenfunctions of (23) with an associated frequency, or eigenvalue. The constants C_i in (30) and the value of β in (31) can be determined from the boundary conditions of the problem. In particular, if we denote by ω_i the $i-$ésimo eigenvalue corresponding to $W_i(x)$ the eigenfunction the total response to free vibration of the beam can be obtained by the principle of superposition of normal modes as:

$$w(x,t) = \sum_{i=1}^{\infty} W_i(x)(A_i\cos(\omega_i t) + B_i\sin(\omega_i t)), \qquad (32)$$

where the constants A_i and B_i, $i = 1,\ldots,\infty$ are calculated from the initial conditions of the beam.

III. MODELING OF STRUCTURES

The deflections presented in bridges subject to mobile loads can be correctly expressed taking into account the pre-established boundary conditions, used to determine the normal modes of vibration. Following the ideas presented by Kwon *et al.* [7]; the vertical displacements of bridges crossed by heavy vehicles are modeled as a mass-spring model on a mobile elastic base. It is understood by base the beam that is considered of the Euler-Bernoulli type and therefore the modeling of the foundation must consider the elastic behavior of the structure. Figure 1 presents the analysis scheme where k_1, m_1 e c_1 e k_2, m_2 e c_2 they are the spring constant, mass and damping for the vehicle body and wheel, respectively.
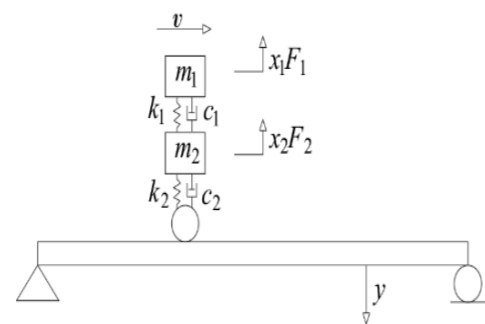

Fig. 1. Schematic: beam and train-type model.

A. Equations of Motion

In this section, the modeling of the bridge will be done along with the standard train. For this, the structure will be represented by a beam, simulating a mobile base. On the other hand, the standard train will be described as the coupling of two bodies, as shown in Figure 1, whose masses will be denoted respectively by m_1 e m_2. Together with the masses we will also consider the elastic constants $k_i, c_i, i = 1, 2$ representing the elastic and dissipative forces of the system, for more details see Rao [10]. Following Kwon *et al.* [7], the following hypotheses will be assumed:

- The structure is idealized as an Euler-Bernoulli beam;
- Only the vertical displacements generated by the vehicle are considered;
- The vehicle moves at a constant speed.

According on image 1 $x_i, i = 1, 2$ represent, respectively, the displacement of the body and structure of the vehicle, while y denoting the displacement of the bridge. The modeling is done considering the bridge as a mobile base but with elastic behavior. Using the free-body diagram for the mass m_1 and m_2, see Figures 1 and 2.
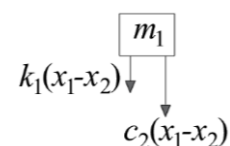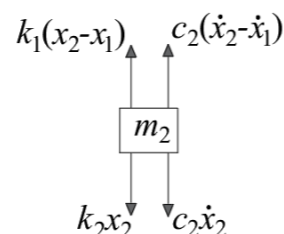

Fig. 2. Free body diagram for mass m_1

Fig. 3. Free body diagram for mass m_2

According to the equations of motion, the following is valid:

$$m_1\ddot{x}_1 + c_1\dot{x}_1 + k_1x_1 - c_1\dot{x}_2 - k_1x_2 = 0 \qquad (33)$$

$$m_2\ddot{x}_2 + c_2\dot{x}_2 + k_2x_2 - c_2\dot{x}_1 - k_2x_1 = k_2y. \qquad (34)$$

Because it is an elastic body and taking into account the Euler-Bernoulli theory, it satisfies the following equation:

$$EI\frac{d^4y}{dx^4} + m\ddot{y} + k_2(y - x_2) = F(x,t),$$
$$y(0) = y(L) = y''(0) = y''(L) = 0. \qquad (35)$$

where $F(x,t)$ denotes the charge concentration due to vehicle displacement being given by:

$$F(x,t) = [(m_1 + m_2)g + m_2\ddot{x}_2 + m_1\ddot{x}_1]\delta(x - vt). \qquad (36)$$

As it is usual in vibration analysis, we will consider the solutions as being harmonic functions, that is, the three displacements, $x_i, i = 1, 2$ and y they present movement synchrony:

$$x_1 = X_1e^{j(\omega t + \varphi)}, \qquad (37)$$

$$x_2 = X_2e^{j(\omega t + \varphi)}, \qquad (38)$$

Calculating $\dot{x}_1, \dot{x}_2, \ddot{x}_1, \ddot{x}_2$ and substituting in equations (33) and (34) we get:

$$-m_1\omega^2 X_1 + jc_1\omega X_1 - jc_2\omega X_2 + k_1X_1 - k_1X_2 = 0 \qquad (39)$$

$$-m_2\omega^2 X_2 - jc_2\omega X_1 + jc_2\omega X_2 - k_2X_1 + k_2X_2 = k_2\phi(x) \qquad (40)$$

The set of equations (39)-(40) can be written in matrix form:

$$\begin{bmatrix} -m_1\omega^2 + jc_1\omega + k_1 & -jc_2\omega - k_1 \\ -j\omega c_2 - k_2 & -m_2\omega^2 + j\omega c_2 + k_2 \end{bmatrix}\begin{bmatrix} X_1 \\ X_2 \end{bmatrix} = \begin{bmatrix} 0 \\ k_2\phi \end{bmatrix},$$

whose solution, by Cramer's rule, is given by:

$$X_1(\omega,x) = \frac{k_2(-jc_2\omega - k_1)\phi(x)}{(-m_1\omega^2 + jc_1\omega + k_1)(-m_2\omega^2 + j\omega c_2 + k_1) - (-j\omega c_2 - k_2)(-jc_2\omega - k_1)}, \qquad (41)$$

$$X_2(\omega,x) = \frac{k_2(m_1\omega^2 + jc_1\omega + k_1)\phi(x)}{(-m_1\omega^2 + jc_1\omega + k_1)(-m_2\omega^2 + j\omega c_2 + k_1) - (-j\omega c_2 - k_2)(-jc_2\omega - k_1)}. \qquad (42)$$

In what follows, we will make use of the following notation:

$$g_1(\omega) = m_1m_2\omega^4 - (m_1k_2 + m_2k_1 + c_1c_2)\omega^2 + k_1k_2 \qquad (43)$$

$$g_2(\omega) = -(c_1m_2 + m_1c_2)\omega^3 + (k_2c_1k_1c_2)\omega, \qquad (44)$$

$$h_1(\omega) = -k_1k_2g_1(\omega) - k_2c_2\omega g_2(\omega)\ldots$$
$$+j(k_1k_2g_2(\omega) - k_2c_2\omega g_1(\omega)) \qquad (45)$$

$$h_2(\omega) = (k_2m_1\omega^2 + k_1k - 2)g_1(\omega) - c_1k_2\omega g_2(\omega)\ldots$$
$$+ j(-(k_2m_1\omega^2 + k_1k_2)g_2(\omega) + c_1k_2\omega g_1(\omega)). \qquad (46)$$

Using equations (43), (44), (45) and (46) and simplifying equations (41) and (42) we get:

$$X_1(\omega,x) = \frac{h_1(\omega)}{g_1(\omega)^2 + g_2(\omega)^2}\phi(x), \qquad (47)$$

$$X_2(\omega,x) = \frac{h_2(\omega)}{g_1(\omega)^2 + g_2(\omega)^2}\phi(x). \qquad (48)$$

In equations (47) and (48), it can be seen that the oscillation amplitude of the vehicle depends both on the frequency and the position of the particle.

For the calculation of the displacement of the base, the following equation must be satisfied for:

$$EI\frac{d^4y}{dx^4} + m\ddot{y} + k_2y = k_2x_2 + F(x,t). \qquad (49)$$

Note that if we consider the operator

$$H = EI\frac{d^4}{dx^4} + k_2I, \qquad (50)$$

acting on space K^2, see in Meirovitch [11], with board conditions given in (35), then equation (50) can be written as:

$$Hy + m\ddot{y} = k_2x_2 + F(x,t). \qquad (51)$$

According to Meirovitch [11], the first step to solve equation (51) is to calculate the natural frequency of the system of equation (51), which naturally leads to the system of eigenvalues for the operator H,

$$H\phi = m\omega^2\phi$$
$$B_i\phi = 0, \quad i = 1:4. \qquad (52)$$

The eigenvalues problem in equation (52) leads to the frequency equation given by:

$$EIs^4 + (m\omega^2 + k_2) = 0, \qquad (53)$$

Doing it $-\beta^4 = \frac{1}{EI}(m\omega^2 + k_2)$ we get:

$$s^4 - \beta^4 = 0, \qquad (54)$$

which implies that the solutions to the problem must be of the form:

$$\phi(x) = c_1\cos(\beta x) + c_2\sin(\beta x) + c_3\cosh(\beta x) + c_4\sinh(\beta x) \qquad (55)$$

W. Da Silva, V.Rocha, R. Tintaya, Ma. Rabelo,
"Deflection Analysis of Beams from Vehicle Velocity",
Latin-American Journal of Computing (LAJC), vol. 10, no. 2, 2023.

It follows from the boundary conditions of the problem and imposing the condition of existence of non-trivial solutions, that the following condition is satisfied:

$$det(A(\beta)) = 0, \tag{56}$$

where the matrix $A(\beta)$ is defined by:

$$A(\beta) = \begin{bmatrix} 1 & 0 & 1 & 0 \\ -\beta^2 & 0 & \beta^2 & 0 \\ \cos(\beta L) & \sin(\beta L) & \cosh(\beta L) & \sinh(\beta L) \\ -\beta^2\cos(\beta L) & -\beta^2\sin(\beta L) & \beta^2\cosh(\beta L) & \beta^2\sinh(\beta L) \end{bmatrix}$$

To get values from β note that:

$$det(A(\beta)) = det(A_1(\beta),\ldots,A_4(\beta)),$$
$$\frac{d}{d\beta}det(A(\beta)) = det'(A(\beta))\frac{dA(\beta)}{d\beta}. \tag{57}$$

The expression on the right in the second equation in (57) is defined by:

$$det'(A(\beta))\frac{dA(\beta)}{d\beta} = \sum_{k=1}^{4}det(A_1(\beta),\ldots,A_{k-1}(\beta),\frac{dA_k(\beta)}{d\beta},A_{k+1}(\beta),\ldots,A_4(\beta)). \tag{58}$$

Using the expression in (58) together with Newton's method, approximate solutions in (56) can be computed by generating the sequence of eigenvalues $\{\beta_n\}$.

The system of equations (33) and (34) together with the boundary condition (35) is solved taking into account the eigenvalues problem in (52). Using the fact that the solution is decomposed into normal vibration modes we have:

$$w(x,t) = \sum_{n=1}^{\infty}q_n(t)\phi_n(x). \tag{59}$$

From (51) we get that the following equation is valid:

$$\left((EIs_n^4 + k_2)q_n(t) + m\omega_n^2\ddot{q}_n(t)\right)e^{s_n x} = \left[(m_1+m_2)g - m_2X_2(x,\omega)\ldots \right. \\ \left. - m_1X_1(x,\omega)\right]\omega^2\delta(x-vt). \tag{60}$$

Multiplying both sides of (60) by $\phi_n(x)$ and integrating from 0 to L we get:

$$\left(EIs_n^4 + k_2\right)q_n(t) - m\omega_n^2\ddot{q}_n(t) = \left[(m_1+m_2)g - m_2h_2(\omega_n)\ldots \right. \\ \left. - m_1h_1(\omega_n)\right]\frac{s_n\omega_n^2(e^{2s_n vt}-1)^{-1}e^{2s_n vt}}{g_1(\omega_n)^2 + g_2(\omega_n)^2} \tag{61}$$

Equation (61) is the bridge oscillation amplitude response. Note that (61) shows the explicit dependence of the system output on the oscillation frequency and vehicle speed.

The image 2 presents the solutions of (61) for values of $n = 1:10$, and image 4 is the sum of all displacements $w_n(x,t)$.
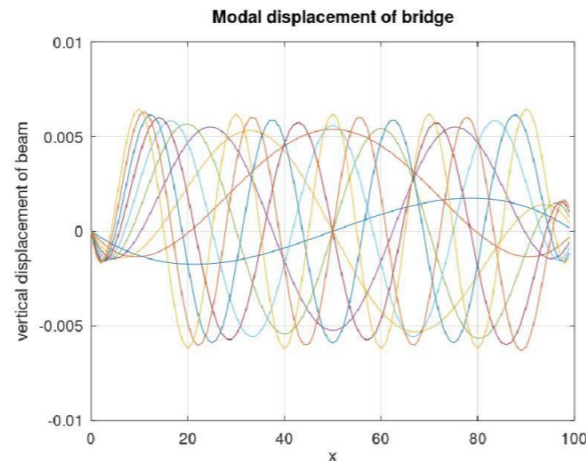

Fig. 4.   Structure modal Displacements

IV. NUMERICAL RESULTS AND CONCLUSIONS

The analyzed project is a reinforced concrete viaduct with 34.50m in length and 13.20m in width, executed on a state highway in the municipality of Goiás. The superstructure is designed in a straight line, consisting of three spans: a central one measuring 14.00m and two adjacent to the central span measuring 7.00m. The spans are constituted by an independent structure simply supported. The structure is formed by the set of 9 beams in the central span as shown in image 3. The work was designed for class 45, using a type 45tf vehicle as prescribed by NBR 7188/82 (brazilian rule), moving at a constant speed of approximately 80km/h. For this class of structures images 2 and 4, respectively represent the displacements of several normal modes of vibration and the displacement involving the sum of ten modes of vibrations. It can be seen from image 4 a damping factor of the structure, even though the equation is a free frequency model. The justification for this fact is that one must take into account the fact that concrete is a composite material, and steel is the main damping factor.
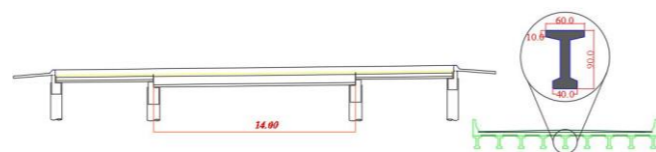

Fig. 5.   Bridge scheme

TABLE I.   STRUCTURE GEOMETRY

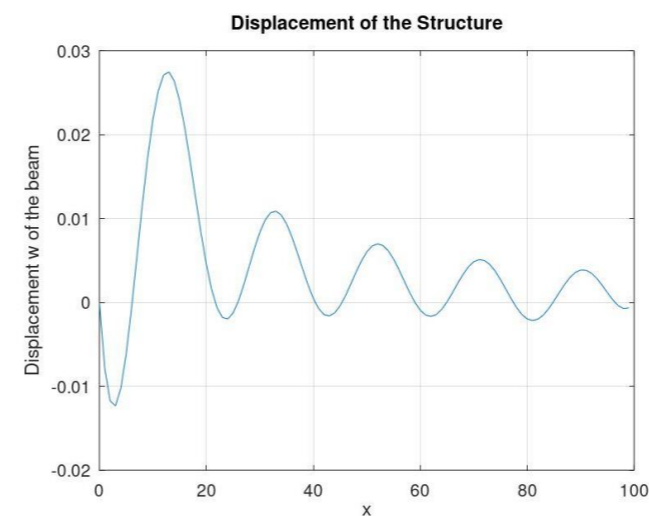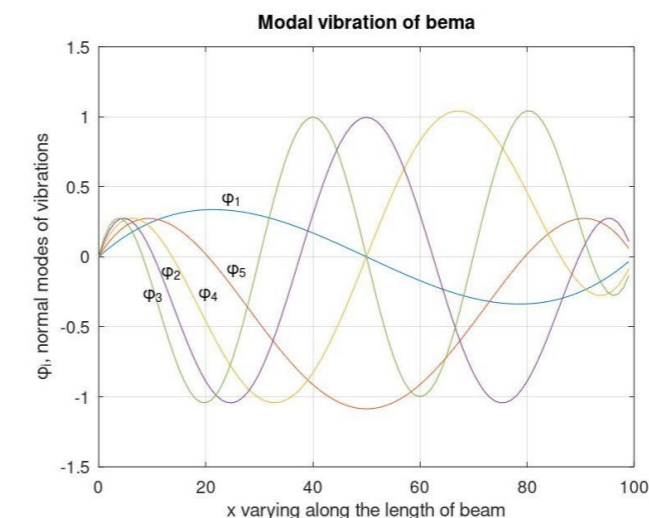| Module of Elasticity	Density of Material	Section Area	Moment of Inertia
35000 (Mpa)	300 (kgf/cm²)	4,81 (m²)	49,33x10⁻⁴ (m⁴)

Fig. 6.   Structure displacement

Fig. 7.   H operator autofunctions for the first five vibration modes

REFERENCES

[1]   Q. Zou, L. Deng, T. Guo, and X. Yin, "Comparative Study of Different Numerical Models for Vehicle–Bridge Interaction Analysis". World Scientific Publishing Company, vol. 16, no. 28, 2016.

[2]   Y. B. Yang, B. H. Lin, "Vehicle–bridge interaction analysis by dynamic condensation method". Journal Struct. Eng., ASCE, vol.121, pp. 1636-1643, 1995.

[3]   X. Q. Zhu, S. S. Law, "Structural Health Monitoring Based on Vehicle-Bridge Interaction: Accomplishments and Challenges". Advances in Structural Engineering, vol. 18, pp.1999-2015, 2015.

[4]   T. Hayashikawa, N. Watanabe, "Dynamic behavior of continuous beams with moving loads".Journal of Engineering Mechanics Division, ASCE, vol. 107, pp. 229-246, 1981.

[5]   K. Matsuoka, H. Tanaka, "Drive-by deflection estimation method for simple support bridgesbased on track irregularities measured on a traveling train". Mechanical Systems and Signal Processing, vol. 182, pp. 109-149, 2023.

[6]   R. Corbally, A. Malekjafarian, "Bridge damage detection using operating deflection shape ratiosobtained from a passing vehicle". Journal of Sound and Vibration, vol. 27, pp.117-125, 2022.

[7]   H. C. Kwon, M. C. Kim, I. W. Lee, "Vibration Control of Bridges Under Moving Loads". Computer e Structures, vol. 66, pp. 473-480, 1998.

[8]   Y. B. Yang, C. W. Lin, J. D. Yau, "Extracting bridge frequencies from the dynamic response of a passing vehicle". Journal of Sound and Vibration, vol. 272, pp. 471-493, 2004.

[9]   M. V. Meyer, D. Cantero, R. Lenner, "Dynamics of long multi-trailer heavy vehicles crossingshort to medium span length bridges". Engineering Structures, vol. 247, pp. 113-149, 2021.

[10]   S. S. Rao, Mechanical vibrations", 5° ed., Pearson, Miami. 2010.

[11]   L. Meirovitch, Computational methods in structural dynamics, Springer Science & BusinessMedia 1980.

AUTHORS

Werley da Silva

Graduated in Mathematics from the Federal University of Goiás (2012), with emphasis on Mathematical Modeling as a way of learning. He holds a degree in Civil Engineering from Centro Universitário UNA de Catalão (2019), with an emphasis on automation in vibration control in Special Artworks. He holds a Master's Degree in Production Engineering from the Federal University of Goiás (2020). He is currently a student of the Graduate Program in Exact and Technological Sciences at the Federal University of Catalão, working mainly on the following topics: finite element methods, signal acquisition/treatment, mathematical methods applied to structures, mathematical modeling and non-linear systems , prestressed concrete and theory of structures.

Renato Tintaya Mollo

Renato Alejandro Tintaya Mollo nasceu em Arequipa - Peru, no ano de 1984, e obteve o título de Bachiller em Matemáticas em 2006 na Facultad de Ciencias Naturales e Fomales da Universidad Nacional de San Agustín de Arequipa e o título de Mestre em Ciências no Programa de Matemática em 2009, pelo Instituto de Ciências Matemáticas e de Computação da Universidade de São Paulo.
Atualmente é professor adjunto no Instituto de Matemática e Tecnologia da Universidade Federal de Catalão, onde atua desde 2013 principalmente nas disciplinas de Cálculo Diferencial e Integral, Geometria Analítica e Álgebra Linear. Foi membro da Comissão de Ações de Enfrentamento ao Assédio Moral, Sexual e Preconceito. Também é aluno de doutorado do Programa de Pós-Graduação em Ciências Exatas e Tecnológicas da UFCAT. Tem interesse no estudo de modelagem matemática e simulação computacional de estruturas, além de pesquisa em ensino de matemática com foco no nível superior.

Victor Henrique Rocha

Graduated in Production Engineering from the University of Uberaba (2015), Master in Production Engineering from UFG Federal University of Goiás (2021), technical training from Senai (National Service for Industrial Learning) as a mechanical technician (2012). He currently works as Professor of Higher Education at the UNA university, and acts as Management and Engineering Coordinator at a mining company in Brazil. He has experience in project management, industrial maintenance planning, lean methodology and technical asset management, and preparation of maintenance engineering technical studies.

Marcos Rabelo

Graduated in Mathematics from the Federal University of Uberlândia (2001), Master's in Mathematics from the University of São Paulo (2003), Ph. He is currently adjunct level II at the Federal University of Goiás. He has experience in Mathematical Physics and Numerical Modeling, with emphasis on methods based on finite differences and finite element methods, acting on the following topics: partial functional differential equations, ordinary equations, mathematical methods applied to structures and dynamic systems.

Analysis of U-Net Neural Network Training Parameters for Tomographic Images Segmentation

Yana dos Santos Pereira
Laboratory of Computational Intelligence
Federal University of Western Pará
Santarém, Brazil
yana.pereira@discente.ufopa.edu.br
ORCID: 0000-0002-2307-0752

Davi Guimarães da Silva
Laboratory of Computational Intelligence
Federal University of Western Pará
Santarém, Brazil
davi.guimaraes@ifpa.edu.br
ORCID: 0000-0001-9810-6820

Regina Cely Barroso
Laboratory of Applied Physics to
Biomedical and Environmental Sciences
University of Rio de Janeiro
Rio de Janeiro, Brazil
cely_barroso@hotmail.com
ORCID: 0000-0001-6348-694X

Anderson Alvarenga de Moura Meneses
Laboratory of Computational Intelligence
Federal University of Western Pará
Santarém, Brazil
anderson.meneses@ufopa.edu.br
ORCID: 0000-0003-1461-2772

Y. Pereira, A. Meneses, D. Silva, R. Barroso,
"Analysis of U-Net Neural Network Training Parameters for Tomographic Images Segmentation",
Latin-American Journal of Computing (LAJC), vol. 10, no. 2, 2023.

Analysis of U-Net Neural Network Training Parameters for Tomographic Images Segmentation

Yana dos Santos Pereira
Laboratory of Computational Intelligence
Federal University of Western Pará
Santarém, Brazil
yana.pereira@discente.ufopa.edu.br
ORCID: 0000-0002-2307-0752

Davi Guimarães da Silva
Laboratory of Computational Intelligence
Federal University of Western Pará
Santarém, Brazil
davi.guimaraes@ifpa.edu.br
ORCID: 0000-0001-9810-6820

Regina Cely Barroso
Laboratory of Applied Physics to Biomedical and Environmental Sciences
University of Rio de Janeiro
Rio de Janeiro, Brazil
cely_barroso@hotmail.com
ORCID: 0000-0001-6348-694X

Anderson Alvarenga de Moura Meneses
Laboratory of Computational Intelligence
Federal University of Western Pará
Santarém, Brazil
anderson.meneses@ufopa.edu.br
ORCID: 0000-0003-1461-2772

Abstract— In the field of computational vision, image segmentation is one of the most important resources. Nowadays, this procedure can be made with high precision using Deep Learning, and this fact is important to applications of several research areas including medical image analysis. Image segmentation is currently applied to find tumors, bone defects and other elements that are crucial to achieve accurate diagnoses. The objective of the present work is to verify the influence of parameters variation on U-Net, a Deep Convolutional Neural Network with Deep Learning for biomedical image segmentation. The dataset was obtained from Kaggle website (www.kaggle.com) and contains 267 volumes of lung computed tomography scans, which are composed of the 2D images and their respective masks (ground truth). The dataset was subdivided in 80% of the volumes for training and 20% for testing. The results were evaluated using the Dice Similarity Coefficient as metric and the value 84% was the mean obtained for the testing set, applying the best parameters considered.

Keywords— *Deep Learning, Biomedical Image Segmentation, Fully Convolutional Networks, U-Net, Computed Tomography*

I. Introduction

Deep Learning (DL) is a branch of machine learning developed by learning successive layers, almost always using models called neural networks [1], through data representations. Nowadays the application of DL has presented promising results in biomedical image segmentation. Zhang et al. [2] designed Convolutional Neural Networks (CNNs) [3] architectures to segment infant brain tissues in Magnetic Resonance (MR) images which is a process even more difficult for adults due to the low tissue contrast, increased noise and ongoing white matter myelination. The CNNs segmentation of isointense-phase brain image outperformed competing methods on a set of manual process. Oktay et al. [4] applied the U-Net model to the segmentation of pancreas, which presented Dice Similarity Coefficients (DSCs) 2% to 3% higher than other models. This improvement in pancreas segmentation is important in many clinical applications of liver segmentation in 3D images [5]. In addition, through the application of DL, it becomes possible to perform more qualitative or even quantitative analysis of the regions of interest, such as lesions [6], a factor that represents important advances for the entire healthcare sector. The use of DL generates results that do not rely on the subjectivity of the observer and provide a decrease of the time needed for segmentation once the model is trained.

Although several Artificial Neural Networks (ANNs) [7] have been used in biomedical image segmentation, in this work, the U-Net architecture was used. U-Net is a Fully Convolutional Neural Network (FCN or Fully Convnet) that has been consolidating as one of the most prominent ANNs for biomedical images.

The performance improvement of U-Net into images segmentation can be achieved by adjusting the parameters for the problem in question. Goyal et al. [8] investigated the influence of batch size in other CNNs performances and verified that large minibatches cause optimization difficulties when working with ImageNet dataset [9]. Furthermore, Nishio et al. [10] developed a methodology for determining cancer diagnoses, classifying nodules between benign and malignant as well as verifying the stage of the disease, which could correspond to primary lung cancer or metastatic lung cancer. Evaluating the effect of image size as input of the deep convolutional neural network used, testing image sizes equal to 56, 112 and 224, the results showed that larger image sizes as inputs improved the accuracy of lung nodule classification.

The objective of the present work is to evaluate the influence of U-Net parameters variation during the segmentation of lung computed tomographies. This way, it is possible to segment the lungs in the tomography with high precision which makes subsequent processes easier, for example, the detection of pulmonary nodules for early diagnosis of lung cancer.

The remaining of the article is structured as follows. Section II contains the theoretical framework. Section III presents the adopted methodology. Section IV is dedicated to the results and discussions. Finally, section V contains the conclusion of the work.

II. Theorical Framework

A. Biomedical Image Segmentation

Image segmentation is considered the most important medical imaging process and corresponds to the extraction of the Region of Interest (ROI), subdividing the image into areas based on specific characteristics, such as segmenting body organs and tissues to detect tumors and other elements and this division can be applied for both 2D and 3D data [11]. The binary segmentation, applied in the present work, subdivides the image in a white part that corresponds to the mask containing the ROI, and a black part as background. Once obtained, in addition to detecting tumors or other abnormalities, the masks can measure tissue growth analyzing the growth of possible tumors and help in treatment planning.

B. Fully Convolutional Neural Networks

FCNs are classified as a specific type of CNNs that contains a convolutional path connected to a Fully Connected (FC) layer [12]. The FCs has Multilayer Perceptron (MLP) as main representative and they are used to classification. The main difference between the designs of CNNs and FCNs is that the last one has a deconvolutional path, also called expansion path, instead of the dense layer. Therefore, FC reduce the number of parameters once there are no FC layers, speeding up learning and inference. As output, the FCNs generate a pixel vector whose size corresponds to the input data [13].
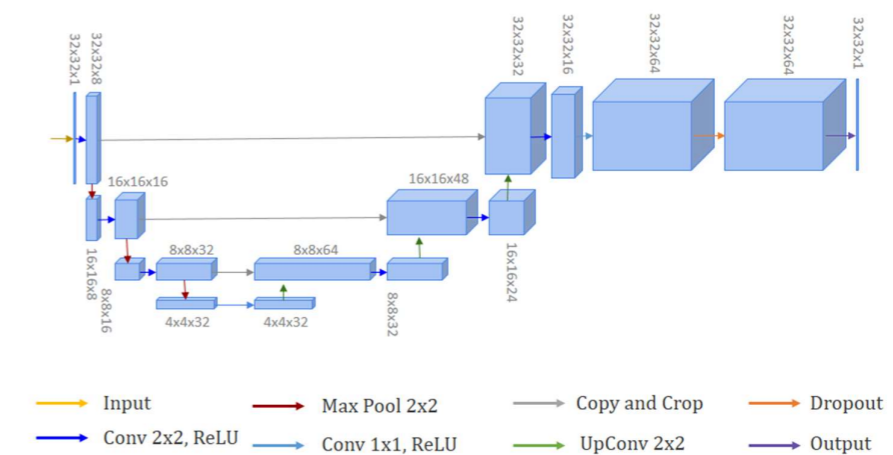

Fig. 1. Architecture of U-Net

C. Net

U-Net is an FCN created by Ronneberger, Fischer and Brox [14] in order to cope with biomedical images segmentation. The architecture of the ANN is composed of two paths. The first path is called the contracting one, which aims to capture the context. On the other hand, the second path corresponds to the expanding path, which allows precise localization. Precisely, because of the fact that the database of biomedical images uses not to be very large, the authors created a network that is able to be trained end-to-end and presents accurate results.

In Fig. 1, each blue box corresponds to a multi-channel feature map. The path indicated by the red arrows on the left side of the image corresponds to convolutional path, also known as downsampling path. On the right side, indicated by green arrows, there is the deconvolutional path or upsampling path. Just before the output, there is a layer called Dropout, where some neurons are randomly turned off during the training. This regularization is a method to avoid overfitting in the process.

D. Batch Size

During each epoch, all training set was used but subdivided in batches, for updating the U-Net weights and improving performance. Batch Size is the hyperparameter in Convolutional Neural Networks that corresponds to the number of images used to train a single forward and backward pass. The correlation between CNNs performance and Batch Size also depends on the datasets nature, mainly in the case of medical ones due to its complexity [15].

E. Early Stopping

Early Stopping is considered a regularization method capable of determining when to stop the execution of an iterative algorithm [16]. This callback calculates the precision of segmentation or classification using validation data. It interrupts the training when precision stops improving, avoiding overfitting, within a given range called patience that corresponds to its most important hyperparameter.

F. Related Works

Paiva et al. [17] used U-Net to segment microcomputed tomography images which the ROI corresponds to lenses of tadpole specimen of the frog Thoropa miliaris and compared the performance to methods of semiautomatic segmentation. The research concluded that the automatic segmentation using Fully Convnet was much faster than the semiautomatic processes and it also showed high accuracy.

Moura and Meneses [18] segmented heart computed tomography images testing U-Net performance with number of epochs (50, 100) variation, number of features (32, 64) variation, BatchNormalization, RMSprop optimizer function and BinaryCrossentropy loss function. The authors concluded that there was no statistically significant difference between the different parameters adjustment, therefore the chosen model could be the one with the smallest standard deviation

LATIN-AMERICAN JOURNAL OF COMPUTING (LAJC), Vol X, Issue 2, July 2023

Y. Pereira, A. Meneses, D. Silva, R. Barroso,
"Analysis of U-Net Neural Network Training Parameters for Tomographic Images Segmentation",
Latin-American Journal of Computing (LAJC), vol. 10, no. 2, 2023.

(0.065) and the smallest time of execution (368 seconds), which was U-Net with 32 feature maps, BatchNormalization and 100 epochs.

Saood and Hatem [19] segmented lung Computed Tomography (CT) using U-Net and SegNet in order to detect and label infected tissues in the lungs and contribute to verify the diagnosis of patients contaminated by COVID-19. The results of the work presented that U-Net showed better performance as a multi-class segmentor.

Kandel and Castelli [15] classified images from a histopathology dataset, testing batch size equal to 16, 32, 64, 128 and 256, with fixed learning rate 0.001 and Adam optimizer. The authors concluded that the largest batch size presented the highest performance.

Thambawita et al [20] classified gastrointestinal endoscopy images using two different CNNs models testing image resolutions ranging from 32x32 to 512x512 pixels. The results showed that the best performance occurred when the models were training and applied into testing data with the highest image resolution.

III. MATERIAL AND METHODS

The code was implemented in Python 3.8.13, using Keras 2.6.0 API, Numpy 1.21.5, and OpenCV 4.5.5.64 with Tensorflow 2.6.0 as backend. An HP Elitedesk 800 desktop was used with an Intel Core i7-6700 3.40 GHz CPU, 16 GB RAM, Windows 10 Pro 64 bits Operating System, and an Nvidia GeForce GT 730 GPU.

Fig. 2 presents the research methodological flowchart and each stage will be described during the following sections.
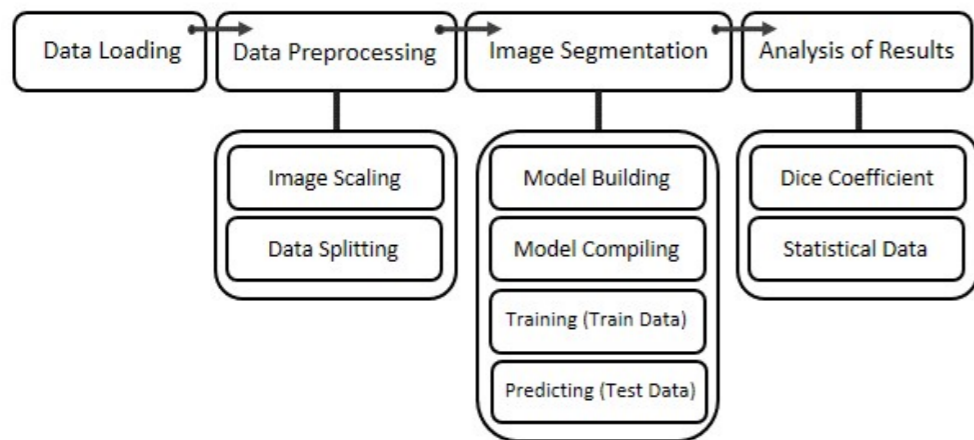

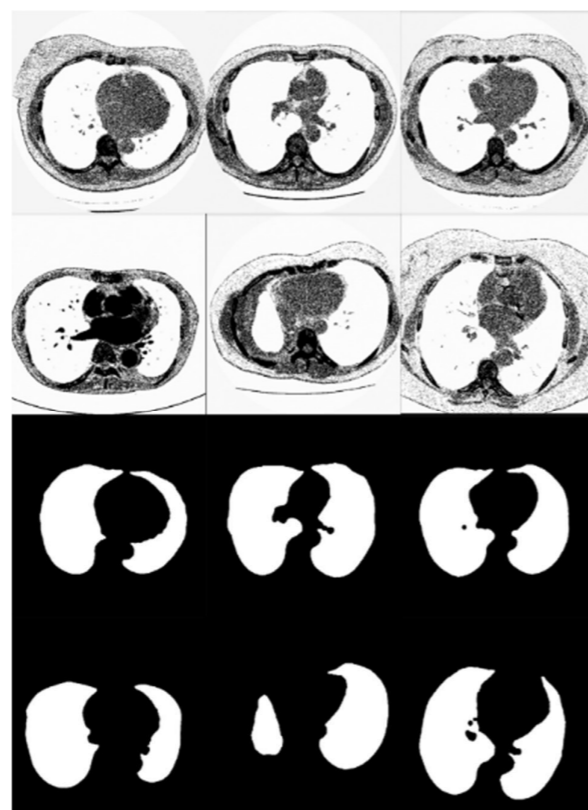Fig. 2. Methodological Flowchart

A. Dataset

Fig. 3. Representation of Dataset Volumes

The CT volumes were downloaded from Kaggle website (https://www.kaggle.com/datasets/kmader/finding-lungs-in ct-data?resource=download) which contains several open source datasets.

The database used is composed of 267 lungs CT scans and each volume presents 2D images and their corresponding mask representing the ROI highlighted in white and the background in black. The data contained 512x512 pixels on its dimensions.

B. Data Preprocessing

Before starting the segmentation, there were three stages of preprocessing that had to be performed. First step was to subdivide the volumes in training and testing. Therefore, 80% of the initial data became training and validation data, corresponding to 214 volumes, while 20% of the initial data became testing data, equivalent to 53 volumes. Secondly, the images were resized for ensuring the correct reading of the data and avoiding possible differences in file dimensions.

Thirdly, the images were normalized. Let I be an n-dimensional grayscale image. A linear normalization transforms $I: \{X \subseteq R^n\} \rightarrow \{I_{min}, ..., I_{max}\}$ with intensity values in the range (I_{min}, I_{max}), into a new image $I_n: \{X \subseteq R^n\} \rightarrow \{I_{n\,min}, ..., I_{n\,max}\}$ with intensity values in the range $(I_{n\,min}, ..., I_{n\,max})$. The linear normalization is represented by:

$$I_n = (I - I_{min}) \frac{I_{n\,max} - I_{n\,min}}{I_{max} - I_{min}}, \quad (1)$$

where I_n is the new intensity, I is the initial intensity, $I_{n\,min}$ is the desired minimum intensity, $I_{n\,max}$ is the desired maximum intensity and I_{max} and I_{min} are the current maximum and minimum intensity. In this case, the minimum value of the range is equal to 0 while the maximum one is equivalent to 1.

C. Data Augmentation

Once the preprocessing was completed, a process of Data Augmentation [21] was realized to enable an increase in the number of training volumes based on the original ones. In order to add more variability in the dataset, certain geometric transformations were applied, such as horizontal and vertical displacement of the lungs in the images, rotation and zoom. With these changes, from each original image 32 new images were generated, improving quality of the training data and avoiding overfitting.

D. Callbacks

Besides Early Stopping as mentioned in section II, the model was performed using two other callbacks, Model Checkpoint and Learning Rate Scheduler, respectively to save the best weight configuration in a .h5 format file and to update the value of the optimization rate between the epochs.

E. Data Splitting

Furthermore, of the 214 volumes reserved for training, only 80% (171 volumes) were actually used for training while the remaining 20% (43 volumes) were used for model validation.

F. Dice Similarity Coefficient

The metric used for both training and testing was the DSC. The DSC corresponds to a comparison between the result shown by the model and the mask equivalent to the image segmented that is the Ground Truth (GT), the reference image. The metric is a reason between the double of the intersection of the compared images and the sum of pixels of the both images and can be calculated by the equation below:

$$Dice\ coef = \frac{2[n(prediction) \cap n(GT)]}{n(prediction) + n(GT)} \quad (2)$$

G. Parameter testing

Different numbers of epochs and patience value from Early Stopping were preliminarily tested. The number of epochs tested were 10, 50 and 100. Then, patience values tested of Early Stopping were 10, 20, 30, 40 and 50. Subsequently, Batch Size values equal to 4, 8, 16 and 32 were tested. Finally, Image Size equal to 32, 64 and 128 pixels were implemented. Five executions were performed for each parameter test in order to analyze its influence on model performance. The seed used during each execution was randomized with a range of 1 to 100 in order to guarantee impartiality in the process.

H. Statistical Analysis

Kruskal-Wallis and Dunn's tests [22, 23] were performed in order to verify if there is statistically significant difference between the parameters' values tested. The Kruskal-Wallis test is used to compare three or more groups of data. If the null hypothesis of no statistically significant difference is rejected, then the Dunn's post-hoc test is used for pairwise comparison between the groups. The Bonferroni correction was applied to Dunn's test for reducing the Type I Error probability. The threshold 0.05 was adopted for the statistical tests. The graphs were plotted with Plotly 5.11.0.

IV. RESULTS AND DISCUSSION

A. Preliminary tests

Kruskal-Wallis test was implemented to analyze the results of number of epochs preliminary test and the p-value obtained was equal to 0.6861. The value shows that there is no statistically significant difference in model performance using different number of epochs, but once using 50 epochs the segmentation presented the highest mean (0.7873) and also the smallest standard deviation (0.0153), it was selected to next steps.

The same procedure was applied to evaluate the results of Early Stopping patience value preliminary test. The p-value was equal to 0.4305, which points to the fact that also no statistically significant difference was found. Again, once patience value equal to 40 obtained the highest mean (0.7880) with the smallest standard deviation (0.0170), it was chosen as the best parameter to patience.

B. Batch Size

In Fig. 4, it is possible to verify the boxplots of DSCs distribution for Batch Size comparison. Table I presents the statistical results for Kruskal-Wallis test.
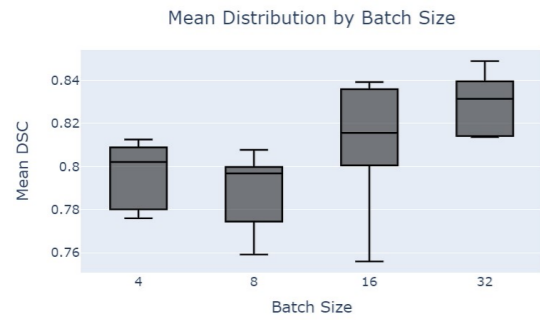
Y. Pereira, A. Meneses, D. Silva, R. Barroso,
"Analysis of U-Net Neural Network Training Parameters for Tomographic Images Segmentation",
Latin-American Journal of Computing (LAJC), vol. 10, no. 2, 2023.

Fig. 4. DSC distribution boxplot for Batch Size

TABLE I: STATISTICAL RESULTS FOR BATCH SIZE

EXEC	MEAN DSC			
	BATCH 4	BATCH 8	BATCH 16	BATCH 32
1	0.7815	0.8077	0.8391	0.8142
2	0.8076	0.7795	0.8347	0.8363
3	0.8125	0.7592	0.7559	0.8136
4	0.7760	0.7971	0.8155	0.8313
5	0.8020	0.7968	0.8153	0.8488
ST-DEV	0.0145	0.0170	0.0297	0.0135
MIN	0.7760	0.7592	0.7559	0.8136
MEAN	0.7959	0.7880	0.8121	0.8289
MEDIAN	0.8020	0.7968	0.8155	0.8313
MAX	0.8125	0.8077	0.8391	0.8488

In this case, the p-value obtained with Kruskal-Wallis test was equal to 0.028 between batch size values used. Then, Dunn's multiple comparisons test with Bonferroni correction was applied to the results.

TABLE II: DUNN'S MULTIPLE COMPARISONS FOR BATCH SIZE

	BATCH 4	BATCH 8	BATCH 16	BATCH 32
BATCH 4	1.0000	1.0000	0.6529	0.1292
BATCH 8	1.0000	1.0000	0.2878	0.0452
BATCH 16	0.6529	0.2878	1.0000	1.0000
BATCH 32	0.1292	0.0452	1.0000	1.0000

Although there is no statistically significant difference between the results obtained using batch size 16 and 32, batch size 32 was statistically significant different from batch size 8, with p-value 0.0452. Batch size 32 also presented a tendency for better results, with mean 0.8289 and standard deviation 0.0135.

C. Image Size

In Fig. 5, it is possible to verify the boxplots of DSCs distribution for Image Size comparison. Table III presents the statistical results for Image Size parameter.
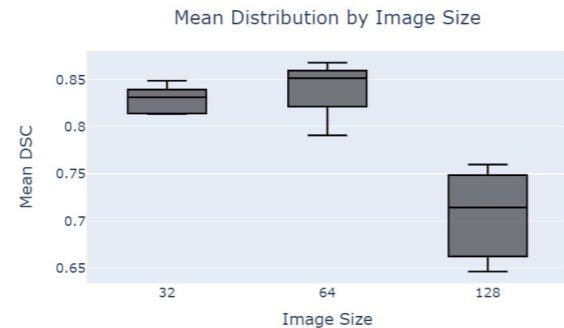

Fig. 5. DSC distribution boxplot for Image Size

TABLE III: STATISTICAL RESULTS FOR IMAGE SIZE

EXEC	MEAN DSC		
	SIZE 32x32	SIZE 64x64	SIZE 128x128
1	0.8142	0.8568	0.6676
2	0.8363	0.8515	0.7598
3	0.8136	0.7909	0.7449
4	0.8313	0.8680	0.6461
5	0.8488	0.8315	0.7142
ST-DEV	0.0135	0.0271	0.0437
MIN	0.8136	0.7909	0.6461
MEAN	0.8289	0.8398	0.7065
MEDIAN	0.8313	0.8515	0.7142
MAX	0.8488	0.8680	0.7598

The p-value obtained by Kruskal-Wallis was 0.0068 between image sizes used. Therefore, Dunn's test with Bonferroni correction was also implemented and the results are presented as follows.

TABLE IV: DUNN'S MULTIPLE COMPARISONS BY IMAGE SIZE

	SIZE 32x32	SIZE 64x64	SIZE 128x128
SIZE 32x32	1.0000	1.0000	0.0710
SIZE 32x32	1.0000	1.0000	0.0071
SIZE 32x32	0.0710	0.0071	1.0000

The Dunn's test results show that there is no statistically significant difference between the means obtained using image size equal to 32 and 64. There is only a statistically significant difference between 64×64 with respect to 128×128. Furthermore, although image size 32 presented the smallest standard deviation (0.0135), once image size 64 showed the highest mean (0.8398) and the highest median (0.8515), it was chosen as the best parameter.

Fig. 6 presents the segmentation with maximum DSC. It is possible to verify that the lung in the tomography has well-defined edges and low noise.

Fig. 6. Computed tomography, equivalent Ground Truth and prediction by U-Net, respectively, of the volume with maximum DSC of testing data.

Conversely, Fig. 7 shows the segmentation with minimum DSC, showing that the CT scan has high noise and low contrast on its edges.

Fig. 7. Computed tomography, equivalent Ground Truth and prediction by U-Net, respectively, of the volume with minimum DSC of testing data.

This way, it is observed that the best segmentations occurred to images that had low noise image, the lung borders are not scattered and there was a significant contrast between the lung and background.

V. CONCLUSION

In this work, U-Net was used to segment lungs in CT data. The dataset was subdivided in training data and testing data

and the model was trained using the masks (GTs) also available in the dataset.

Four parameter tests were implemented. First, different number of epochs and early stopping patience were compared with no statistically significant difference observed.

Afterwards, Batch Size test was performed, in which 32 was classified as the most satisfactory value, demonstrating that the model needed to increase the number of images used to training on each forward and backward pass, probably because of computed tomography complexity.

Finally, Image Size test was performed, in which 64×64 pixels was the dimension that presented better results in relation to 128×128, it shows that using the highest dimensions available can cause difficulty to model learning and segmentation, but the results were not conclusive regarding 32×32 pixels.

Predictions performed by the model to the testing data were compared to the GT, presenting satisfactory results in terms of the metrics used as basis throughout the process (DSC) even though the low number of volumes in the dataset.

Therefore, in terms of the dataset used, the present research confirms the efficiency of the U-Net architecture in order to segment biomedical images, factor which enables its implementation to future works of interest to both DL and health care applications.

REFERENCES

[1] F. Chollet, Deep Learning with Python. Manning Publications; 2017. ISBN 9781617294433.

[2] W. Zhang et al., "Deep convolutional neural networks for multi-modality isointense infant brain image segmentation," Neuroimage, vol. 108, pp. 214–224, Mar. 2015, doi: 10.1016/j.neuroimage.2014.12.061.

[3] Y. Lecun, E. Bottou, Y. Bengio, and P. Haffiner, "Gradient-Based Learning Applied to Document Recognition", 1998.

[4] O. Oktay et al., "Attention U-Net: Learning Where to Look for the Pancreas," Apr. 2018, [Online]. Available: http://arxiv.org/abs/1804.03999

[5] D. Shen, G. Wu, and H.-I. Suk, "Deep Learning in Medical Image Analysis," 2017, doi: 10.1146/annurev-bioeng-071516.

[6] X. Liu, L. Song, S. Liu, and Y. Zhang, "A review of deep-learning-based medical image segmentation methods," Sustainability (Switzerland), vol. 13, no. 3, pp. 1–29, Feb. 2021, doi: 10.3390/su13031224.

[7] S. Haykin, Neural Networks: A Comprehensive Foundation., Prentice-Hall, 1999.

[8] P. Goyal et al., "Accurate, Large Minibatch SGD: Training ImageNet in 1 Hour," Jun. 2017, [Online]. Available: http://arxiv.org/abs/1706.02677.

[9] J. Deng, W. Dong, R. Socher, L.-J. Li, K. Li, and L. Fei-Fei, ImageNet: A Large-Scale Image Database. IEEE, 2009.

[10] M. Nishio et al., "Computer-aided diagnosis of lung nodule classification between benign nodule, primary lung cancer, and metastatic lung cancer at different image size using deep convolutional neural network with transfer learning," PLoS One, vol. 13, no. 7, Jul. 2018, doi: 10.1371/journal.pone.0200721.

[11] A. Ashour, Y. Guo, and Mohamed W., "Medical Image Segmentation."

[12] I. Goodfellow, A. Courville and Y. Bengio. Deep Learning (Adaptive Computation and Machine Learning Series).

[13] D. Nie, L. Wang, Y. Gao, and D. Sken, "Fully convolutional networks for multi-modality isointense infant brain image segmentation," in Proceedings - International Symposium on Biomedical Imaging, Jun. 2016, vol. 2016-June, pp. 1342–1345. doi: 10.1109/ISBI.2016.7493515.

[14] O. Ronneberger, P. Fischer, and T. Brox, "U-net: Convolutional networks for biomedical image segmentation," in Lecture Notes in Computer Science (including subseries Lecture Notes in Artificial Intelligence and Lecture Notes in Bioinformatics), 2015, vol. 9351, pp. 234–241. doi: 10.1007/978-3-319-24574-4_28.

[15] I. Kandel and M. Castelli, "The effect of batch size on the generalizability of the convolutional neural networks on a histopathology dataset," ICT Express, vol. 6, no. 4, pp. 312–315, Dec. 2020, doi: 10.1016/j.icte.2020.04.010.

[16] G. Raskutti, M. J. Wainwright, and B. Yu, "Early Stopping and Non-parametric Regression: An Optimal Data-dependent Stopping Rule," 2014.

[17] K. Paiva et al., "Performance evaluation of segmentation methods for assessing the lens of the frog Thoropa miliaris from synchrotron-based phase-contrast micro-CT images," Physica Medica, vol. 94, pp. 43–52, Feb. 2022, doi: 10.1016/j.ejmp.2021.12.013.

[18] M. Moura and A. Meneses, "Evaluation Of Unet Convolutional Neural Network Parameters For Segmentation Of Heart CT Images". Available in the annals of XXIV National Meeting of Computacional Modeling (ENMC).

[19] A. Saood and I. Hatem, "COVID-19 lung CT image segmentation using deep learning methods: U-Net versus SegNet," BMC Med Imaging, vol. 21, no. 1, Dec. 2021, doi: 10.1186/s12880-020-00529-5.

[20] V. Thambawita, I. Strümke, S. A. Hicks, P. Halvorsen, S. Parasa, and M. A. Riegler, "Impact of image resolution on deep learning performance in endoscopy image classification: An experimental study using a large dataset of endoscopic images," Diagnostics, vol. 11, no. 12, Dec. 2021, doi: 10.3390/diagnostics11122183.

[21] C. Shorten and T. M. Khoshgoftaar, "A survey on Image Data Augmentation for Deep Learning," J Big Data, vol. 6, no. 1, Dec. 2019, doi: 10.1186/s40537-019-0197-0.

[22] A. Dmitrienko, C. Chuang-Stein, R. D'Agostino. "Pharmaceutical Statistics Using SAS", 2014. In Journal of Chemical Information and Modeling (Vol. 53, Issue 9). SAS Publishing.

[23] M. Neuhauser. "Nonparametric Statistical Tests", 2011. Chapman and Hall/CRC. https://doi.org/10.1201/b11427.

AUTHORS

Yana Pereira

Yana dos Santos Pereira is currently pursuing a Physics Engineer Bachelor degree at the Federal University of Western Pará (UFOPA). She is member of the Computational Intelligence Laboratory (LabIC/UFOPA) since 2021, granted by the Brazilian National Council for Scientific and Technological Development from August 2022 to January 2023, when started working as data scientist and technology consultant at Ernst & Young Global Limited. In 2022, she won a Merit Award at UFOPA for her research in the U-Net convolutional neural network for lung computed tomographies segmentation. She currently remains developing researches in the field of biomedical image segmentation using Deep Learning. Her research interests are Deep Learning, Data Mining, Data Analytics, Data Science, Computational Vision, Biomedical Image Segmentation, Computing applied to health and Software Engineering. She has skills to apply principles of Agile Methodologies, mainly Scrum and Kanban, for developing software and working with groups in an efficient and responsive manner.

Regina Cely Barroso

Regina Cély Barroso is Full Professor in the Physics Institute at the Rio de Janeiro State Univerty, UERJ, in Brazil, since 1986. Currently, she is the coordinator of the Laboratory of Applied Physics in Biomedical and Environmental Sciences, Lab_FisMed/UERJ. Dr. Barroso earned her BS in Physics at UERJ, MS and PhD in Nuclear Engineering from COPPE/ Federal University of Rio de Janeiro in 1997. She published more than one hundred of papers in scientic journals and supersived more than thirty MS, PhD and postdoctor students. Her interests include the methodologies, instrumentation and applications of hard X-ray nanoprobes for quantitative three-dimensional imaging, propagation based phase contrast X-ray imaging, synchrotron based microtomography. Her research focus particularly on key applications of synchrotron X-ray on biomedical imaging.

Davi Guimarães

Davi Guimarães da Silva is doctorate in Environmental Sciences from Federal University of Western Pará (UFOPA - 2023). Master in Informatics from the Federal University of Amazonas (UFAM - 2016). Specialization in Teaching for Vocational Education (2018). Specialization in Systems Engineering (2013). MBA Specialization in Environment (2011). Graduated in Data Processing Technology from the Federal University of Pará (UFPA - 2009). He is currently Professor at the Federal Institute of Education Science and Technology of Pará (IFPA). Areas of interest: Deep Learning (Time Series Prediction), Energy (Computational Intelligence applied to monitoring electrical energy consumption), Database and Information Retrieval area, Machine Learning, Data mining, Information Technologies applied to Education, Virtual Learning Objects, Augmented Reality Applied to Education.

Anderson Meneses

Anderson Alvarenga de Moura Meneses - Graduated in Physics from the Federal University of Rio de Janeiro (2000), in Brazil. Master (2005) and doctorate (2010) degrees in Nuclear Engineering from COPPE Institute, at the Federal University of Rio de Janeiro, with a fellowship at the Dalle Molle Institute for Artificial Intelligence (IDSIA, University of Lugano, Switzerland) in 2009. Specialist in Systems Analysis, Design and Management from Pontifical Catholic University, in Rio de Janeiro (2008). Associate Professor at the Federal University of Western Pará (UFOPA). Head of the Computational Intelligence Laboratory (LabIC/ UFOPA) since 2015. Leader of the Computational Intelligence and Optimization research group. Permanent member of the Postgraduate Program in Amazon Natural Resources (PPGRNA/UFOPA). Collaborating member of the Postgraduate Program in Society, Nature and Development (PPGSND/UFOPA). Researcher PQ2 granted by the Brazilian National Council for Scientific and Technological Development (CNPq/Brazil). Areas of interest: Nuclear Engineering (optimization of nuclear reactor fuel reload), Deep Learning (Time Series Prediction and Image Processing) and Energy (Artificial Intelligence applied to electrical energy consumption monitoring).

Identification of Nano-Beams Rigidity Coefficient: A Numerical Analysis Using the Landweber Method

Elisa Ferreira Medeiros
Instituto Federal de Educação, Ciência e
Tecnologia Sul-rio-grandense (IFsul)
Pelotas, Brasil
fm.elisa@hotmail.com
ORCID: 0000-0002-5356-8244

Adriano De Cezaro
Instituto de Matemática, Estatística e Física
(IMEF)
Fundação Universidade Federal do Rio
Grande (FURG)
Rio Grande, Brasil
decezaromtm@gmail.com
ORCID: 0000-0001-8431-9120

Fabiana Travessini De Cezaro
Instituto de Matemática, Estatística e Física
(IMEF)
Fundação Universidade Federal do Rio
Grande (FURG)
Rio Grande, Brasil
fabi.travessini@gmail.com
ORCID: 0000-0001-9401-5315

E.F. Medeiros, A. De Cezaro, F. Travessini De Cezaro,
"Identification of Nano-Beams Rigidity Coefficient: A Numerical Analysis Using the Landweber Method",
Latin-American Journal of Computing (LAJC), vol. 10, no. 2, 2023.

Identification of Nano-Beams Rigidity Coefficient: A Numerical Analysis Using the Landweber Method

Elisa Ferreira Medeiros
Instituto Federal de Educação, Ciência
e Tecnologia Sul-rio-grandense (IFsul)
Pelotas, Brasil
fm.elisa@hotmail.com
ORCID 0000-0002-5356-8244

Adriano De Cezaro
Instituto de Matemática, Estatística e
Física (IMEF)
Fundação Universidade Federal do Rio
Grande (FURG)
Rio Grande, Brasil
decezaromtm@gmail.com
ORCID 0000-0001-8431-9120

Fabiana Travessini De Cezaro
Instituto de Matemática, Estatística e
Física (IMEF)
Fundação Universidade Federal do Rio
Grande (FURG)
Rio Grande, Brasil
fabi.travessini@gmail.com
ORCID 0000-0001-9401-5315

Abstract— Due to their supporting function, beams are one of the main elements in structural projects. With the intense technological development in the field of nanotechnology, beams at micro- and nanoscales have become objects of intense study and research interest, see for example [8]. In this approach, we analyze numerically the inverse problem of identifying the stiffness coefficient in micro-nano-beams as a function that implicitly depends on the fractal media map for the continuum from strain measurements. Such a problem is unstable with respect to noise in strain measurements, which is inherent in practical problems. We introduce the equations that compose Landweber's iterative regularization method as a strategy to obtain a stable and convergent approximate solution with respect to the noise level in the measurements. We show some scenarios with simulated data for identifying the stiffness coefficient for different noise levels in measurements and for different coefficient of transformation of fractal medium. The results found numerically show that Landweber's method is a regularization strategy for the problem of identifying the stiffness coefficient in micro/nano-beams.

Keywords—micro/nano-beams, inverse problem, fractal media, Landweber's method

I. INTRODUCTION

Every day, we are surrounded by beams. They are the fundamental structural elements that carry vertical loads. Though beams are traditionally used to describe building or civil engineering, beams can be found in all existing structures as structural elements, including machine frames, bones, carbon nanotubes, molecular chains, and other mechanical or structural systems. In these structures, the size-scale is paramount for a precise description of the mechanical properties of the beam [9].

In continuum mechanics, the analysis of movements and deformations is determined by the hypothesis that the medium is composed of matter in a homogeneous way. This theory ignores the existence of voids formed when molecules and atoms are not evenly distributed. The question that arises in micro- and nanoscale analysis is whether conventional models of continuum mechanics, such as Euler-Bernoulli and Timoshenko, may not be appropriate, given that such approaches do not take into account the scale factor in their models, see for example [9]. To address the scale issue, some non-classical continuum theories, as well as theories incorporating non-integer order derivatives in the [6, 7, 8, 9] models, have been investigated. Models with fractional

dynamics have been shown to be more suitable for describing the properties of various real materials, e.g. [6], and thus have aroused the interest of engineering research.

In [7] an overview of the modeling of fractal media through the theory of continuous mechanics is presented using the ideas proposed in [8]. This theory consists of describing the laws of equilibrium for fractal media using fractional integrals. Using a map from the fractal to the continuous medium, those fractional integrals are rewritten as integrals in conventional Euclidean space. The interesting thing about this approach is that the essential condition of continuum mechanics, the separation of scales, can be replaced by the use of continuum field equations. In Section II, we present the deduction of the Euler-Bernoulli equation for beams in fractal media, using the techniques proposed in [8]. We also show that the analyzed model has a unique solution $u(x)$, which is known in the literature as the direct problem for the Euler-Bernoulli beam model in fractal media.

The main contribution of this work is the numerical investigation of an "inverse problem" for the Euler-Bernoulli beam model in fractal media. Indeed, the stable identification of the stiffness parameter $a(x)$ associated with the Euler-Bernoulli equation in fractal media, as described in Section II, from indirect measurements of the nano (micro)-beam deflection of $u(x)$. Given that measurements of the nano (micro)-beam deflection $u(x)$ are subject to errors and that the inverse problems are generally ill-posed in the Hadamard sense [2, 3], the issue of instability in the identification of stiffness parameter $a(x)$ due to noise measurements of the beam deflection $u(x)$ necessitates the use of some regularization strategy. In this contribution, we use the Landweber iterative method (see Section III), which will be used to numerically demonstrate the stability of the approximations for the identification coefficient $a(x)$ in Section IV. In Section IV, we will present several numerical tests with varying levels of noise in the measurements. The presented scenarios demonstrated numerically that the Landweber iteration obtains stable approximate solutions for the coefficient $a(x)$ under different fractal medium properties.

II. EULER-BERNOULLI EQUATION IN FRACTAL MEDIA

In general, a fractal medium cannot be considered as a continuous medium, as there are points and domains that are

not filled by particles of the medium. These domains can be called porous. Thus, the application of continuum theory to fractal media is not appropriate. To get around this difficulty, [8] proposed the use of fractional integrals to represent the mass of a region W in three-dimensional Euclidean space $\mathbb{E}^3$ as being:

$$m(W) = \int_W \rho(R)dV_D = \int_W \rho(R)c_3(D,R)dV_3, \quad (1)$$

with

$$c_3(D,R) = R^{D-3}\frac{2^{3-D}\Gamma(3/2)}{\Gamma(D/2)}, \quad R = \sqrt{x_i x_i}, \quad (2)$$

where R is the length scale measurement, D is the fractal dimension of mass, and Γ is Euler's Gamma function. The coefficient c_3 establishes the transformation between fractal and continuous media. The term dV_D is the infinitesimal element of volume in fractal space, and dV_3 is the infinitesimal element of volume in $\mathbb{E}^3$. However, the proposal of [8] implies that the measure of the fractal dimension in each of the directions of the medium must be the same. To contour this limitation, [8] proposed an approach in which the measure of length in relation to each coordinate of the medium is given by:

$$dl_k(x_k) = \rho(x)c_1^{(k)}(\alpha_k, x_k)dx_k, \quad k = 1, 2, 3, \quad (3)$$

where $\rho(x)$ represents mass density and α_k a fractal dimension in the direction x_k.

Assuming that $c_1^{(k)}$ is given by the modified Riemann-Liouville integral, that is:

$$c_1^{(k)} = \alpha_k\left(\frac{l_k - x_k}{l_{k0}}\right), \quad k = 1, 2, 3. \quad (4)$$

where l_k is the total length along x_k and l_{k0} is the characteristic length in the given direction, [8] showed that it is possible to reproduce almost all the known results of the mechanical theory of the continuum, in addition to allowing to represent more heterogeneous media.

A. One-dimensional fractal medium: the Euler-Bernoulli equation

Assume that we are in Euclidean dimension 1, in the x direction. Let dimension $D < 1$ be the dimension of the fractal structure in which we are immersed, in the direction x. Then it follows from (3) that the element dx must be replaced by:

$$dl_D = c_1(D,x)dx. \quad (5)$$

Rewriting the balance equations in variational form, with the measure given by (5) and using the generalized Green-Gauss Theorem, see [8], it follows that the Euler-Bernoulli equation in fractal means is given by:

$$\nabla_x^D\nabla_x^D(EI\nabla_x^D\nabla_x^D u) = 0 \quad (6)$$

wherein

$$M(x) = a(x)\nabla_x^D\nabla_x^D u(x) \quad (7)$$

is the bending moment with $a(x) = E(x)I(x)$ the stiffness coefficient. In (6) and (7), the operator $\nabla_x^D\nabla_x^D$ is the Laplacian operator for fractal media, given by:

$$\nabla_x^D\nabla_x^D u = c^{-1}(c^{-1}u'(x))' \quad (8)$$

where $c = c(x) = c_1(x)$ is the transformation coefficient between the fractal medium and the continuous medium.

In this work, we will consider (7) with the following boundary conditions:

$$u(0) = u'(0), \quad (9)$$

corresponding to a cantilever beam.

B. The inverse problem as an equation of operators

To formulate the inverse problem that we are interested in this work, we first need to formulate some hypotheses for which problem (7) with boundary conditions (9), has a single solution, that is, the direct problem is well posed.

A1: The stiffness coefficient $a = a(x)$ and the transformation coefficient $c = c(x)$ are measurable functions on $[0,L]$ that satisfy the condition $\bar{a} \geq a(x) \geq \underline{a} > 0$ and $\bar{c} \geq c(x) \geq \underline{c} > 0$ for known constants $\bar{a}, \underline{a}, \bar{c}, \underline{c}$. The set of coefficients satisfying the hypothesis **A1** will be denoted by Ad in this manuscript and referred to as the admissible set.

A1': The stiffness coefficient and the transformation coefficient besides satisfying **A1** have uniformly bounded $\|a'\|, \|c'\|$, that is, the coefficients belong to the set $A = \{a, c \in L^\infty | \lambda_1 \leq a, c \leq \lambda_2, \|a', c'\| \leq Q\}$, where $\|\cdot\|$ denotes the norm $L^2(0,L)$ with $0 < \lambda_1 \leq \lambda_2 < \infty$ and $Q > 0$.

A2: The bending moment $M(x) \in C[0,L]$.

Consider the vector space

$$\mathcal{L}^2[0,L] := \{f \text{ measurable, such that}$$

$$\int_0^L c^{-1}(x)(f(x))^2 dx < \infty\} \quad (10)$$

with the inner product below

$$< f, g >_{\mathcal{L}^2} = \int_0^L \sqrt{c(x)}f(x)\sqrt{c(x)}g(x)dx. \quad (11)$$

It follows from the Assumption **A1** that the space of functions $\mathcal{L}^2[0,L]$ with the norm induced by the inner product (11) is a space of Hilbert. Furthermore, the space $\mathcal{H}_0^1[0,L]$ will denote the Sobolev space of all functions in, $g \in \mathcal{L}^2[0,L]$ with the derivatives in the weak sence, g' also belongs to $\mathcal{L}^2[0,L]$, and satisfies $g(0) = g(L) = g'(0) = g'(L) = 0$. See, for example [1].

In order to prove existence and uniqueness for a solution of the problem (7) with conditions in (9), we use the theory of weak solution as follows. First, we consider as a weak solution to problem (7) any function $u \in \mathcal{H}_0^1[0,L]$ such that

$$\int_0^L c^{-1}u'\phi'dx = \int_0^L \frac{M}{a}c\phi dx \quad (12)$$

for any test function $\phi \in \mathcal{H}_0^1[0,L]$.

Lemma 1: Assume that the assumptions **A1** and **A2** are satisfied. If there is u satisfying the problem (7) and (9), then u is a weak solution to the problem (12). Conversely, if u is a weak solution to (12), then u satisfies (7) almost always.

LATIN-AMERICAN JOURNAL OF COMPUTING (LAJC), Vol X, Issue 2, July 2023

E.F. Medeiros, A. De Cezaro, F. Travessini De Cezaro,
"Identification of Nano-Beams Rigidity Coefficient: A Numerical Analysis Using the Landweber Method",
Latin-American Journal of Computing (LAJC), vol. 10, no. 2, 2023.

Proof: It follows from Hypothesis **A1** and **A2** that $c.M/a \in \mathcal{L}^2[0,L]$. Therefore, from (7) and conditions (9), $u \in \mathcal{H}_0^2[0,L]$ and satisfy (12) (see the Green's identities in [1]).

Reciprocally, if $u \in \mathcal{H}_0^1[0,L]$ is a weak solution to (7), it is, satisfies (12), then boundary conditions (9) for the problem in (7) are satisfied. Furthermore, as u satisfied (12) by assumption, we have, after an integration by parts, that

$$< -a\nabla_x^D \nabla_x^D u - M, \phi > = < 0, \phi > \forall \phi \in C_0^\infty[0,L]. \quad (13)$$

Therefore, it follows from the density of $C_0^\infty[0,L]$ in $\mathcal{H}_0^1[0,L]$ that $-a\nabla_x^D \nabla_x^D u = M$, almost everywhere. Hence, by the Hahn-Banach theorem (see [1]) the result for (13) can be extended to $\mathcal{H}_0^1[0,L]$.

Given the Lemma 1, it is possible to prove through the Lax Milgram's Theorem [1] the existence of a unique solution $u \in \mathcal{H}_0^1[0,L]$ that satisfies (12). Indeed, notice that u is a weak solution of (7) if and only if u satisfies

$$A(u,\phi) = l(\phi) \qquad \forall \phi \in \mathcal{H}_0^1[0,L] \quad (14)$$

where $A : \mathcal{H}_0^1[0,L] \times \mathcal{H}_0^1[0,L] \to \mathbb{R}$ is the bilinear form defined as

$$A(u,\phi) := \int_0^L c^{-1} u' \phi' dx \quad (15)$$

and $l : \mathcal{H}_0^1[0,L] \to \mathbb{R}$ is the linear functional given by

$$l(\phi) := \int_0^L \frac{M}{a} c\phi dx. \quad (16)$$

Theorem 1: Assuming that the hypotheses **A1** and **A2** are satisfied, there is a unique solution to (12). As a consequence of the Lemma 1, there is a unique weak solution to (7).

Sketch of Proof: Following the same ideas in [4], it is possible to prove that the linear functional defined in (16) is continuous and furthermore that the bilinear form defined in (15) is continuous and coercive in $\mathcal{H}_0^1[0,L]$. Therefore, it follows from the Lax-Milgram Theorem [1, Corollary 5.8] the existence of a unique function $u \in \mathcal{H}_0^1[0,L]$ satisfying (12).

As a result of Theorem 1, it follows that, for any given function $c(x)$, satisfying Assumption **A1**, the operator

$$F_{c(x)} : Ad \subset \mathcal{L}^2[0,L] \longrightarrow \mathcal{L}^2[0,L]$$
$$a \longmapsto u(a) \quad (17)$$

where $u(a) = u_c(x, a(x))$ is the unique solution of (7), is well defined. $F_{c(x)}$ is called the forward operator in the theory of inverse problems, see for example [2, 3].

C. The inverse problem

Assume that the functions $M(x)$ and $c(x)$ are known. The inverse problem that we are interested in this work deals with the identification of the stiffness coefficient $a(x)$ from measurements $u^\delta(x)$, with noise level δ, satisfying:

$$\|u^\delta - u_c(a)\|_{\mathcal{L}^2[0,L]} \leq \delta \quad (18)$$

of the deflection $u(x) = u_c(x)$ solution of (7) with boundary conditions (9). Equivalently, determine $a(x)$ in the operator equation (17), from the measures $u^\delta(x)$ satisfying (18).

Inverse problems, in general, do not have the property of continuous dependence of the measures u^δ. This implies that small perturbations of magnitude δ in the measurements can generate large perturbations in obtaining the solution of the inverse problem of interest, e.g., [2, 3]. As a result, obtaining stable and convergent solutions with respect to the noise level δ requires the use of regularization methods. See for example [2, 3, 4, 5].

The problem of identifying the stiffness coefficient $a(x)$ in a beam does not have the property of continuous dependence of the measures u^δ, as demonstrated in the case of $c(x) = 1$ in [4, 5]. As a result, the stable identification of the stiffness coefficient $a(x)$, requires some regularization methods [2, 3]. In this contribution, we will use an iterative regularization method called the Landweber method [2] to recover the parameter $a(x)$ in a stable and convergent manner with respect to the noise level δ. In other words, we will show numerically that the Landweber iteration (see equation (19)) together with a stop criterion, called the discrepancy principle (see equation (20)), generates approximate stiffness coefficients a_k^δ, for $a(x)$, with values that are stable and convergent to $a(x)$, as a function of the noise level in the data δ. The iterative algorithm is presented in Section III, while the numerically simulated scenarios for the recovery of the stiffness coefficient $a(x)$ is presented in Section IV.

III. LANDWEBER'S ITERATIVE METHOD

The Landweber iteration (Landweber's iterative method) for the identification of the coefficient $a(x)$ in (7), is given by

$$a_{k+1}^\delta = a_k^\delta + \gamma F'_{c(x)}(a_k^\delta)^*(u^\delta - F_{c(x)}(a_k^\delta)), \quad (19)$$

where γ is a relaxation parameter. $F'_{c(x)}(a_k^\delta)^*$ denotes the adjunct of the Fréchet derivative of the parameter-to-measurement operator $F_{c(x)}(a)$, defined in (7). a_0 is the initial guess of the iteration (14), that shall be chosen properly.

Because the data contains δ noise, the iterative method must be combined with a stop rule, as mentioned in [2, 3, 4, 5]. In this work, we use the discrepancy principle's stopping criterion, which states that (19) must be stopped at the first step k^* that satisfies

$$\|u^\delta - F_{c(x)}(a_{k^*}^\delta)\| \leq \tau\delta < \|u^\delta - F_{c(x)}(a_k^\delta)\| \quad (20)$$

for some $\tau > 1$. Thus, the number of iterations k^* determines the stopping rule of the method.

The numerical implementation to obtain the coefficient $a(x)$ iteratively according to (19) is given by the following algorithm:

(1) Choose an initial value for $a_0 \in L^\infty$ and $c(x)$ satisfying Assumptions **A1** and **A1'**, respectively. Choose also the parameter values δ, τ, γ.

(2) Add the uniformly distributed random variable $z(x) \in [0,1]$ to the solution $u(x)$ of the forward problem to generate the noise data $u^\delta = u(x) + \delta z(x)$, satisfying $\|u(x) - u^\delta\| \leq \delta$.

(3) As long as the iteration (19) is such that a_k^δ, for $k < k^*$, where k^* denotes the iteration index that satisfies the discrepancy principle, do the following steps:

(4) Solve the problem

$$a_k^\delta c^{-1}(c^{-1} u'(a_k^\delta))' = M$$

with the initial conditions

$$u(0) = u'(0) = 0.$$

(5) Evaluate the residue

$$r_k = u_k^\delta - F_{c(x)}(a_k^\delta)$$

wherein $F_{c(x)}(a_k^\delta)$ is solution of differential equation calculated in Step (4).

(6) To calculate $F'_{c(x)}(a_k^\delta)^* r_k$, firstly,

(6.1) Solve the differential equation

$$-(c^{-1}(a_k^\delta v_k)')' = r_k$$

with finals conditions

$$v(L) = v'(L) = 0.$$

(6.2) Then, find the adjunct

$$AD_k := F'_{c(x)}(a_k^\delta)^* r_k$$

solving

$$\frac{M}{a_k^\delta} v_k$$

wherein v_k is solution of equation obtained in Step (6.1).

(7) Update a_{k+1}^δ wherein $a_{k+1}^\delta = a_k^\delta - \gamma AD_k$.

(8) Go back to Step (3) while the discrepancy principle given by (20) is not reached.

(9) Otherwise, the regularized solution is $a_{k^*}^\delta$, where k^* is determined by the discrepancy principle (20).

It is important to mention that, for the calculations of $F'_{c(x)}(a_k^\delta)^*$ in Step (6) in the algorithm, it is necessary to define an auxiliary operator given by

$$A(a) : H^2[0,L] \cap H_0^1[0,L] \longrightarrow L^2[0,L]$$
$$u \longmapsto A(a)u := -ac^{-1}(c^{-1}u')'. \quad (21)$$

for $a, c \in Ad$. It is straightforward to show that the operator defined in (21) is linear, bounded and bijective. Therefore, it also has a linear and bounded inverse $A^{-1}(a)$. The adjunct operator of $A(a)$ is such that $A^*(a)v = -(c^{-1}(av)')'$, corresponding the Step (6.1) in the algorithm. Because it is also linear and bounded, its inverse is given by

$$(A^*(a))^{-1}w = v \quad (22)$$

where v is the unique solution of the $-(c^{-1}(av)')' = w$.

The equations obtained in Step (6) of the above algorithm are calculated by taking the Fréchet derivative of the operator $F_{c(x)}(\cdot)$ defined in (12) and integrating by parts with respect to the inner product given by (11). Therefore, we obtain

$$F'(a)^* r = (c^{-1}u')'(A^{-1}(a))^* r \quad (23)$$

with $A^*(a)^{-1}$ as (22) applied to residue $r = u^\delta - F_{c(x)}(a^\delta)$. Hence, the Steps (6.1) and (6.2) of the algorithm are equivalent to (23).

IV. NUMERICAL EXAMPLES

In this section, we use the Landweber regularization method given by (19) to identify the beam stiffness coefficient $a(x)$, in the fractal media Euler-Bernoulli equation modeled by (7) and (9). In all the simulations presented below, we use $x \in [0,1]$, and the bending moment $M(x) = \frac{x^2}{2} - x + \frac{1}{2}$. Also, we use $a_0 = 0.75$ as the initial guess of the Landweber iteration method (19). The finite difference method was used to obtain the numerical solution u for (7) at points $x_i = i/n$ where $i = 0, 1, 2, \ldots, n$ for $n = 50$ points for the simulated scenario of Example 1 and $n = 100$ points for the other simulated scenarios. In all examples, the noisy data u^δ is generated by adding a random variable $z(x) \in [0,1]$, evenly distributed, to the solution $u(x)$ of (7), such that $u^\delta(x) = u(x) + \delta.z(x)$, where δ is the noise level.

The differential equations corresponding to Step (6) of the algorithm were solved using backward Euler's method to account for the final conditions. The steps of the algorithm resulting from the Landweber method, presented in Section III, were implemented in Python (version 3.8.5).

Example 1: The simulated scenario corresponding to this first example consists in identifying the stiffness coefficient $a^*(x) = 1$ in the fractal medium Euler-Bernoulli beam where the fractal medium transformation coefficient is $c(x) = 2x + 1$.

Fig. 1 compares the coefficients $a(x)$ and $a_{k^*}^\delta(x)$ recovered by the Landweber method given by (14) for noise levels $\delta = 0.0001, \delta = 0.001$ and $\delta = 0.01$, respectively. The simulations were performed on a mesh with $n = 100$ points. The numerical results shown in Fig. 1 demonstrate that Landweber's iterative method produces stably approximate solutions $a_{k^*}^\delta(x)$ for the stiffness coefficient $a^*(x) = 1$, as a function of the noise level δ.
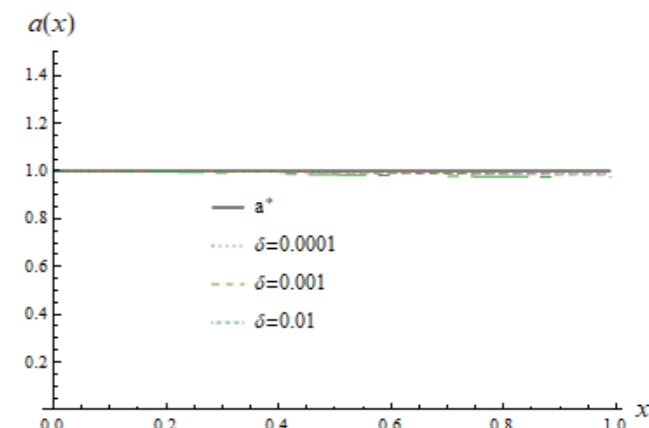

Fig. 1. Identification of the stiffness coefficient $a^*(x)$ corresponding to Example 1

In the simulations presented in Fig. 1, the reconstructed coefficient $a_{k^*}^\delta(x)$ is obtained by using the discrepancy principle, for with the iteration is stopped after $k^* = 143$ iterations for the noise level $\delta = 0.0001$. While, the iteration is stopped after $k^* = 92$ and $k^* = 77$, for the noise level of $\delta = 0.001$ and $\delta = 0.01$, respectively.

In the following simulated scenarios, we will consider the identification of a non-constant stiffness coefficient $a(x)$, as a way of evaluating the performance of Landweber's iterative method in more unfavorable scenarios.

Example 2: The simulated scenario of this example corresponds to the identification of the stiffness coefficient

LATIN-AMERICAN JOURNAL OF COMPUTING (LAJC), Vol X, Issue 2, July 2023

E.F. Medeiros, A. De Cezaro, F. Travessini De Cezaro,
"Identification of Nano-Beams Rigidity Coefficient: A Numerical Analysis Using the Landweber Method",
Latin-American Journal of Computing (LAJC), vol. 10, no. 2, 2023.

$a^*(x) = \dfrac{1}{2-x}$, from noise measurements of the fractal Euler-Bernoulli beam equation (6), where the fractionality of the medium is given by $c(x) = 2x + 1$.

The results for noise levels of $\delta = 0.0001, \delta = 0.001$ and $\delta = 0.01$ are shown in Fig. 2. The mesh was chosen uniformly with $n = 50$ points. This figure show that the Landweber iteration with the stopping criterion given by the discrepancy principle in (20) produced stable and satisfactory approximations $a_{k^*}^{\delta}$ for the non-constant coefficient $a^*(x)$.
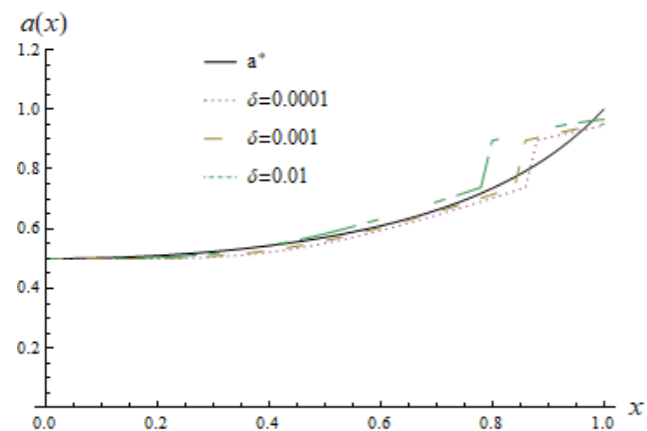

Fig. 2. Identification of the stiffness coefficient $a^*(x)$ for Example 2

The principle of discrepancy given in (20) is reached for the scenarios of this example with $k^* = 101$, $k^* = 44$ and $k^* = 37$, for the simulated noise levels for $\delta = 0.0001$, $\delta = 0.001$, and $\delta = 0.01$, respectively.

In the simulated scenarios that follow, we present approximate solutions for recovering the coefficient $a^*(x)$ as in Examples 1 and 2, where the fractionality of the medium $c(x)$ is distinct.

Example 3: The simulated scenario of this example corresponds to the Euler-Bernoulli fractional media beam, where the coefficient of fractionality is given by $c(x) = x^2 + 1$. The simulations for a noise level of $\delta = 0.0001$, $\delta = 0.001$ and $\delta = 0.01$, are presented in order to recover the coefficient $a^*(x) = 1$, in Fig. 3.

Fig. 3 shows the coefficient $a(x)$ recovered by the Landweber method given in (19) for different noise levels $\delta = 0.0001$, $\delta = 0.001$ and $\delta = 0.01$. The simulation was performed on a mesh with $n = 50$ points.
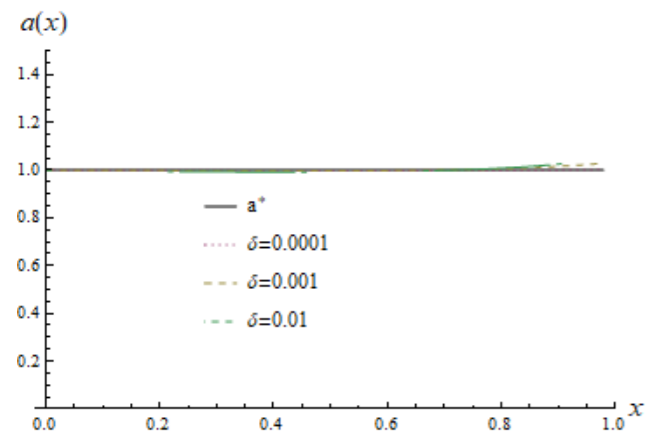

Fig. 3. Identification of the constant stiffness coefficient for Example 3

In Fig. 3, the reconstructed coefficients $a_{k^*}^{\delta}(x)$ for different noise levels $\delta = 0.0001$, $\delta = 0.001$ and $\delta = 0.01$ satisfied the discrepancy principle, respectively, with $k^* = 102$, $k^* = 97$ and $k^* = 89$.

Example 4: The simulated scenario of this example corresponds to the Euler-Bernoulli fractional media beam, where the coefficient of fractionality is given by $c(x) = x^2 + 1$. The simulations for noise level $\delta = 0.0001$, $\delta = 0.001$ and $\delta = 0.01$ are presented in Fig. 4 in order to recover the coefficient $a^*(x) = \dfrac{1}{2-x}$.

Fig. 4 shows the coefficient $a_{k^*}^{\delta}(x)$ recovered by the Landweber method given in (19) for different noise levels $\delta = 0.0001$, $\delta = 0.001$ and $\delta = 0.01$, respectively. The simulation was performed on a mesh with $n = 50$ points.

The principle of discrepancy given in (20) is reached of this example for the simulated noise levels, where $k^* = 132$ for $\delta = 0.0001$, $k^* = 117$, for $\delta = 0.001$ and $k^* = 105$ for $\delta = 0.01$.
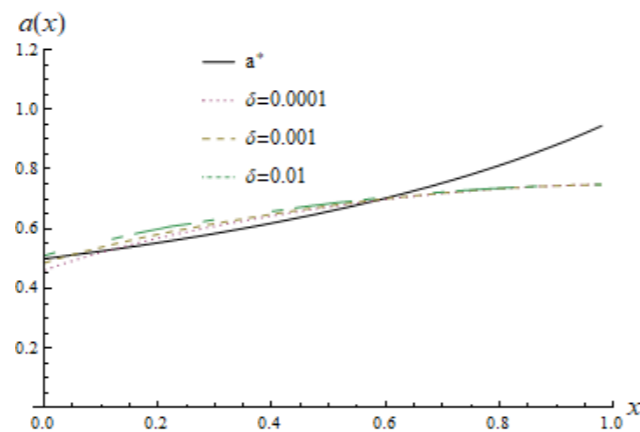

Fig. 4. Identification of the stiffness coefficient $a^*(x)$ for Example 4

The numerical results shown in Examples 1, 2, 3, and 4 demonstrate that Landweber's iterative method terminated with the discrepancy principle produces stably approximate solutions $a_{k^*}^{\delta}(x)$, for the simulated scenarios with the stiffness coefficient $a(x) = 1$ and $a(x) = \dfrac{1}{2-x}$ and for different proposed noise levels with distinct fractionality transformation coefficient $c(x)$. It is worth noting that the discrepancy principle in Examples 3 and 4 is stretched after more iterations than previous examples, which is possible due to the polynomial degree of the coefficient $c(x)$. It will be investigated in future contributions.

V. Conclusions

In this paper, we present a fractal mechanics-based version of the Euler-Bernoulli equation for beams at micro- and nanoscales, as well as the inclusion of the parameter $c(x)$ responsible for characterization of the fractionality of scales. We investigated the inverse problem of identifying the Euler-Bernoulli equation coefficient $a(x)$ from measures of noisy data corresponding to the bending of a fractal media beam. As this problem is ill-posed in the Hadamard sense, we numerically analyze the Landweber iteration method as a regularization, in order to obtain stable and convergent solutions for the parameter of interest in terms of the noise level. We present some numerical examples for different noise

levels in the recovery of constant and non-constant stiffness coefficients $a(x)$. In addition, we performed tests with two different functions for the fractal parameter $c(x)$, evaluating the performance of the method in these cases as well. In fact, the numerical results presented showed that the proposed iterative method satisfactorily recovered the stiffness coefficient, reaching the stopping criterion with a similar number of iterations in the different tests, even when simulated for different parameters $c(x)$.

References

[1] H. Brezis, "Functional Analysis, Sobolev Spaces and partial differential equations," vol. 2. New York: Springer, 2011.

[2] B. Kaltenbacher, A. Neubauer, and O. Scherzer, "Iterative regularization methods for nonlinear ill-posed problems," de Gruyter, 2008.

[3] A. Kirsch, "An introduction to the mathematical theory of inverse problems," vol. 120. New York: Springer, 2011.

[4] E.F. Medeiros, "Identificação do coeficiente de rigidez no modelo de Euler-Bernoulli para vigas," M.S. thesis, FURG, Rio Grande, 2019.

[5] E.F. Medeiros, A. De Cezaro, F. Travessini de Cezaro, "Métodos iterativos de regularização para identificação do coeficiente de rigidez na equação de Euler-Bernoulli para vigas," *Trends in Computational and Applied Mathematics*, vol. 23, no. 2, 2022.

[6] Z. Rahimi, S.R. Ahmadi, and W. Sumelka, "Fractional Euler-Bernoulli Beam Theory Based on the Fractional Strain-Displacement Relation and its Application in Free Vibration, Bending and Buckling Analyses of Micro/Nanobeams," *Acta Physica Polonica, A.*, vol. 134, no. 2, 2018.

[7] O.M. Starzewski, J, Li, H. Joumaa, and P.N. Demmie, "From fractal media to continuum mechanics," *ZAMM-Journal of Applied Mathematics and Mechanics/Zeitschrift für Angewandte Mathematik und Mechanik*, vol. 94, pp. 373-401, 2014.

[8] V. Tarasov, "Continuous medium model for fractal media," Physics Letters A, vol. 336, pp. 167-174, 2005.

[9] L. Tonetto, "Modelos elásticos não-clássicos para vibrações de micro e nanovigas," Ph.D. dissertation, UFRGS, Porto Alegre, 2015.

AUTHORS

Elisa Medeiros

Graduated in Mathematics from the Federal University of Rio Grande in 2017, Master in Computational Modeling from the Federal University of Rio Grande in 2019 and she is currently a PhD student in the same program. Since 2021 she is Professor of Basic, Technical and Technological Education at the Federal Institute Sul-rio-grandense. She is interested in inverse problems and regularization methods.

Adriano De Cezaro

Graduated in Mathematics from the Federal University of Rio Grande in 2003, Master in Mathematics and Scientific Computing from the Federal University of Santa Catarina in 2006 and PhD in Mathematics from the National Institute of Pure and Applied Mathematics Association in 2010. Since 2008 he is Professor at the Federal University of Rio Grande. He has experience in Applied Mathematics, with emphasis on Inverse Problems where the main proposal is to study parameter identification problems in tomography models, differential equation models and propose regularization strategies for such inverse problems, as for example, iterative and continuous regularization methods, level set methods for inverse problems. He is also interested in modeling dynamic systems in biophysical models, with applications in disease dispersion and biological rhythms.

Fabiana De Cezaro

Graduated in Mathematics from the Federal University of Santa Catarina in 2004, Master in Mathematics and Scientific Computing from the Federal University of Santa Catarina in 2007 and PhD in Mathematics from the Federal University of Rio de Janeiro in 2011. Since 2008 she is Professor at the Federal University of Rio Grande. He has experience in Applied Mathematics, with emphasis on Partial Differential Equations and Inverse Problems, working with Parabolic and Hyperbolic Partial Differential Equations (existence, uniqueness, continuous dependence, decay and stability), Spectral Numerical Methods (analysis of convergence and stability rates), and parameter identification problems in tomography models. She is also interested in modeling dynamic systems in biophysical models, with applications in disease dispersion and biological rhythms.

Segmentation of Lung Tomographic Images Using U-Net Deep Neural Networks

Eduardo Stefanato
Dept. of Materials Physics and Mechanics
University of São Paulo
São Paulo, Brazil
edustefanato@gmail.com
ORCID: 0000-0002-2318-9884

Vitor Oliveira
Dept. of Experimental Physics
University of São Paulo
São Paulo, Brazil
vitor.souza.premoli@gmail.com
ORCID: 0000-0001-7688-6854

Christiano Pinheiro
Dept. of Rural Engineering
Federal University of Espírito Santo
Alegre, Brazil
christrieste@yahoo.it
ORCID: 0000-0003-2898-8738

Regina Barroso
Dept. of Applied Physics
Rio de Janeiro State University
Rio de Janeiro, Brazil
cely_barroso@hotmail.com
ORCID: 0000-0001-6348-694X

Anderson Meneses
Inst. of Engineering and Geosciences
Lab. of Computational Intelligence
Federal University of Western Pará
Santarém, Brazil
anderson.meneses@ufopa.edu.br
ORCID: 0000-0003-1461-2772

Segmentation of Lung Tomographic Images Using U-Net Deep Neural Networks

Eduardo Stefanato
Dept. of Materials Physics and Mechanics
University of São Paulo
São Paulo, Brazil
edustefanato@gmail.com
ORCID: 0000-0002-2318-9884

Vitor Oliveira
Dept. of Experimental Physics
University of São Paulo
São Paulo, Brazil
vitor.souza.premoli@gmail.com
ORCID: 0000-0001-7688-6854

Christiano Pinheiro
Dept. of Rural Engineering
Federal University of Espírito Santo
Alegre, Brazil
christrieste@yahoo.it
ORCID: 0000-0003-2898-8738

Regina Barroso
Dept. of Applied Physics
Rio de Janeiro State University
Rio de Janeiro, Brazil
cely_barroso@hotmail.com
ORCID: 0000-0001-6348-694X

Anderson Meneses
Inst. of Engineering and Geosciences
Lab. of Computational Intelligence
Federal University of Western Pará
Santarém, Brazil
anderson.meneses@ufopa.edu.br
ORCID: 0000-0003-1461-2772

Abstract—Deep Neural Networks (DNNs) are among the best methods of Artificial Intelligence, especially in computer vision, where convolutional neural networks play an important role. There are numerous architectures of DNNs, but for image processing, U-Net offers great performance in digital processing tasks such as segmentation of organs, tumors, and cells for supporting medical diagnoses. In the present work, an assessment of U-Net models is proposed, for the segmentation of computed tomography of the lung, aiming at comparing networks with different parameters. In this study, the models scored 96% Dice Similarity Coefficient on average, corroborating the high accuracy of the U-Net for segmentation of tomographic images.

Keywords—*U-Net, Semantic Segmentation, Deep Neural Networks, Biomedical Images*

I. Introduction

In recent years, several works involving Artificial Intelligence (AI) models in biomedical applications have been successful in their proposal. According to [1] and [2], startups such as Ubenwa use acoustic signal processing and machine learning to optimize the diagnosis of asphyxia during birth under low resources.

In other work, Bellemo et al. [3] conducted a study that examines the potential of AI to diagnose diabetic retinopathy in Zambia. Therefore, in view of the great impact and complexity of AI, it is divided into sub-areas of study based on its methods, applications and architectures. One of such areas is Deep Learning (DL) [4].

DL focuses on complex neural networks architectures called DNNs (Deep Neural Networks). According to [5], DL models have architectures with multiple hidden layers, giving depth and complexity to the network. This complexity allows the network to learn different features with various levels of abstraction and generality.

There are several architectures of DNNs, characterized by different method or application, which are used for example for partitioning regions of interest in a set of images. This image processing task is called segmentation and can be applied in various fields such as engineering or medicine.

According to Santos et al. [6], segmentation aids the processing and analysis of medical images by splitting it, and using its parts for correlation with normal anatomy or lesions.

Segmentation of biomedical images has a great importance during a diagnosis, because locating tumors or organs in a medical image is a laborious process, even more so when applied to a large number of images that make up a volume of the examined body [7]. Basically, in a manual segmentation, the professional observes and partitions the objects of analysis.

If the expert uses algorithms or software, then it is a semiautomatic segmentation. For example, local adaptive segmentation algorithms can provide accurate and robust results. However, there is an influence on the quality of segmentation according to the settings applied by each practitioner [8], [9].

Since the manual or semiautomatic methodology is repetitive, it becomes less productive and susceptible to mistakes. Therefore, segmentation has been automated and performed with different mathematical and computational methods such as prototype pairing, geometric modeling, algorithms, statistics, and neural networks [10]–[12].

In this sense, there are several architectures of DNNs for image segmentation, including optimized for medical images such as conventional X-rays, Computed Tomography (CT) and Magnetic Resonance. Some of them are used in the works of Yang et al. [13], Santos et al. [14] and Shusharina et al. [7].

Among the DNNs used for segmentation, U-Net [15] has achieved prominence. The great performance of U-Net in segmentation tasks is a result of its architecture based on successive convolutions and deconvolutions, configuring encoding and decoding sections.

Such a network was first implemented by Ronneberger et al. [15] for biomedical segmentation of 2D images. It was later refined to be applied to 3D images by Çiçek et al. [16]. This peculiarity of U-Net has made it one of the main networks used in the segmentation of medical or biomedical images, even requiring less data (images) to achieve good results [17].

For example, Dong et al. [18] used U-Net for semantic segmentation, highlighting the objects of interest. After segmentation, the objects were classified according to their degree of similarity as lung (left or right), heart, esophagus, or vertebra. Christ et al. [19] applied two U-Net cascade representations, with one of them, they intended exclusively for segmentation and localization of the liver. The other network was in charge of segmenting the tumor within a delimiting region of the CT image.

Therefore, considering the impact that U-Net architecture has on the segmentation of biomedical images, the current work aims to study the performance of U-Net in the segmentation of lung CTs. Analyzing a possible significant influence of the number of levels on the network performance through two architecture configurations. Some training parameters, namely the number of epochs (iterations) and the Batch Size (BS) were also investigated.

Thus, in the present study an evaluation of the effectiveness of some U-Net models is proposed for segmenting healthy lung CT scans. Besides the validation of the networks, it is expected to consolidate one or more models for possible applications in the biomedical area, according to the works of Paiva et al. [20] and Sena et al. [21].

II. Theoretical Background

Some work and descriptions about neural networks, especially U-Net, in image segmentation will be discussed. In this aspect, the work goes through some common literature and reviews on the subject. From this, it was possible to define the types of segmentations seen in the literature, besides describing the U-Net from its particularities.

A. Image Segmentation

Semantic image segmentation is defined as a process that aims to classify the pixels of an image with semantic labels. In the case of instance segmentation, it is possible to partition individual objects. The combination of both processes is known as panoptic segmentation [22]. Thus, in the field of computer vision, segmentation is defined as a step that precedes the classification of objects of interest [23].

Chen et al. [24] reviewed several papers involving the segmentation of cardiac images using DL. Using DNNs, it is possible to highlight anatomical structures of interest, such as ventricles, atria, and vessels. In this aspect, Gosh et al. [23] proposes a study on the different techniques used in image segmentation. The article brings a list of the different neural network architectures used for segmentation as well as their singularities.

In computer vision, the Convolutional Neural Network (CNN) is one of the most widespread techniques for image segmentation [25]. Its learning, in practical terms, occurs by successive segmentations of the input images (forward pass) and the retrofitting of the weights (backward pass) after the calculation of the loss function [26], [27].

Wang et al. [28] investigated segmentation for pathological analysis. Many machine learning algorithms, such as CNNs, have been proposed to automatically segment pathology images. According to the authors, CNNs, such as Fully Convolutional Networks (FCNs), stand out for their accuracy, computational efficiency, and generalizability.

In biomedical applications, the process of segmentation occurs in the partition of an image into multiple segments, simplifying a complex digital image. This procedure allows removing uninteresting information from other objects or artifacts, thus optimizing the image analysis [29].

In this work, the U-Net models propose a semantic segmentation, since it is interested in segmenting the lungs in tomographic images. Therefore, the models are not concerned with partitioning the objects after their detection, not differentiating the left lung from the right lung.

B. U-Net

The U-Net architecture was launched in 2015 [15] and has been improved since 2016 [16]. Its prominence is its effectiveness in segmenting biomedical images without the need for a large number of images to achieve this feature [30]. Since it is a CNN, it is composed of convolution and pooling layers, its particularity lies in the deconvolutions that characterizes the FCN.

Unlike a conventional CNN focused on nominal classification, the goal of the U-Net is to generate new images properly segmented, keeping the dimensions of the input image and the "masks", called Ground Truths (GTs) [26]. The GTs represent the images segmented manually by the professional, they are the ones that together with the input images will feed the network for the beginning of the training.

The insertion of the input images starts the downsampling step, described as the process of successive convolutions that make the image contraction and encodes its information. This process is also called encoder and corresponds to the typical organization process of a CNN [15], [25].

The encoder stage ends at the level where the lower feature map is. From this level on we have the survey layers, also called decoder, which is composed of successive deconvolutions that reduce the number of channels and decode the information, expanding the image by unpooling and highlighting the segmented objects [5]. Sha et al. [31] present an application of U-Net, a semantic segmentation CNN, modified for climate analysis.

The differential of the U-Net architecture is the skip-connections, which are non-sequential neural connections between the symmetric convolution and deconvolution layers. Thus, obtaining an improvement in the updates of the weights and avoiding the saturation gain as the network increases its depth [15].

This particularity causes U-Net architectures to use discrete details learned at the encoder stage to build the segmented image at the decoder layers [30]. Such architecture can be visualized in Fig. 1. Its design diagram represents one of the networks tested in the present work, based on [31], with 5 levels. Fig. 2 represents the second U-Net architecture of the work, with 7 levels.
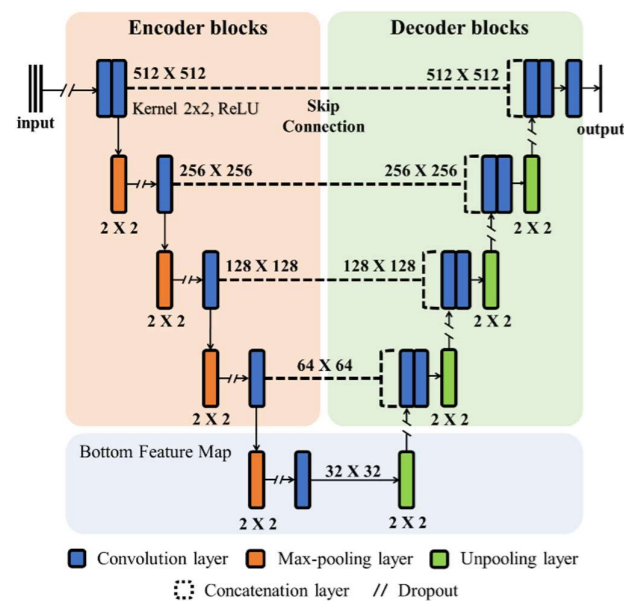
Fig. 1. Diagram of U-Net architecture "v1" with 5 levels. The architectures have the conventional structure of a 2D U-Net with a rectified linear activation function (ReLU).
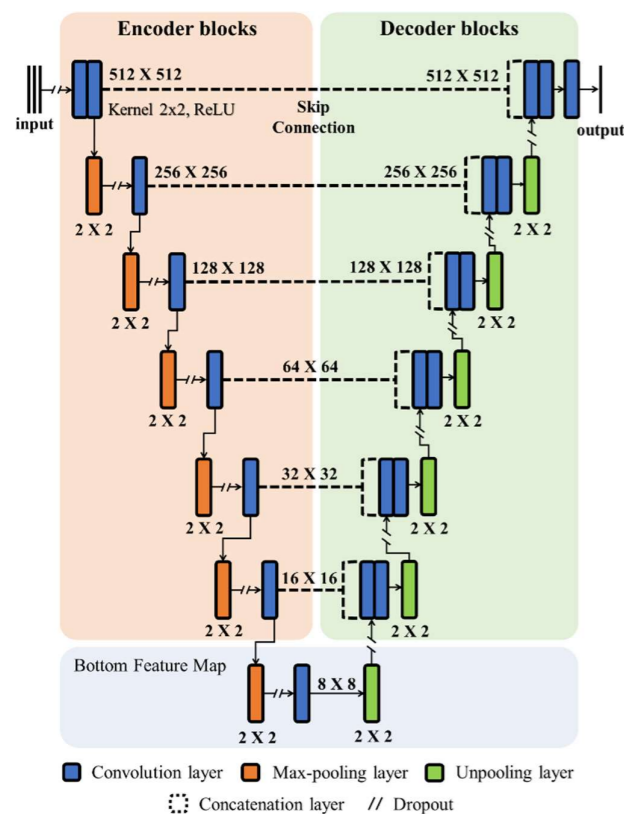

Fig. 2. Diagram of the "v2" U-Net architecture with 7 levels that features two more encoder/decoder layer pairs than "v1". The architectures have the conventional structure of a 2D U-Net with a rectified linear activation function (ReLU).

III. Methodology

The methodology used in the work was divided into five parts, aiming at reproducibility. The first and second parts refer to the data used for training the neural network, the third

and fourth parts to the architectures of the neural network and its training. The fifth part is about the evaluation method, followed by the metrics used for scoring, and finally the statistical analysis used to verify a possible significant difference between the models.

A. Dataset

The images used for training and validation of the networks come from the Cancer Image Archive platform (cancerimagingarchive.net). Three of the 60 thoracic CT image sets from the 2017 AAPM Thoracic Auto-segmentation Challenges [32]–[34] were used. Each set is a scan that contains the entire region of a patient's chest, there was concern that the sets chosen were from different patients, aiming for a more generalist training.

Each thoracic volume image battery has manual contours outlined according to the RTOG1106 guidelines. The contours of each tone highlight some organs such as heart, lungs (left and right), esophagus and vertebra. Each raw set of images of the first, second and third patient have 161, 154 and 148 images, respectively.

B. Data Preprocessing

The sets of images obtained have a lot of information that is not relevant to the network, i.e., because they are a full chest scan, they have images without the presence of the lungs. Therefore, in view of the large number of irrelevant images in each set, it was necessary to remove such slices from the total volume.

After this selection, we obtained 193 images of the first plus second patient that were used for training and internal validation. In addition, 71 images of the third patient were separated for testing and network evaluation.

The second step in the grouping was to extract the GTs from each volume, for which it was necessary to use the "3D Slicer" software. This open source program is recommended by the Cancer Image Archive to interpret the images in DICOM (short for "Digital Imaging and Communications in Medicine") format.

Since the objective of the work is to analyze only the segmentation of the lungs. The other contours of the heart, esophagus and vertebra were removed, thus obtaining only the unified and binarized GTs of the lungs.

The images obtained have, by default, 512 × 512 pixels, however, such dimension includes other elements that are not important for the network, such as the table where the person lies down to perform the exam. Therefore, it was necessary to crop the images to remove such elements, resulting in new images with varied dimensions and specified in Fig. 3.

After the cropping, the images were resized to the standard format (512 × 512). It is worth mentioning that the images were extracted in TIF (Tagged Image File) format, aiming for greater compatibility with the Python language and libraries. Besides this change, the resolution of the images was reduced from 32 bits to 8 bits.

Subsequently, the images were imported and interpreted as a list of matrices. Each element of the matrix, which corresponds to the pixels, went through a normalization process from the maximum and minimum pixel values. After normalization, a list of pixel matrices ranging from 0 to 1 was obtained from both the input images and the GTs.
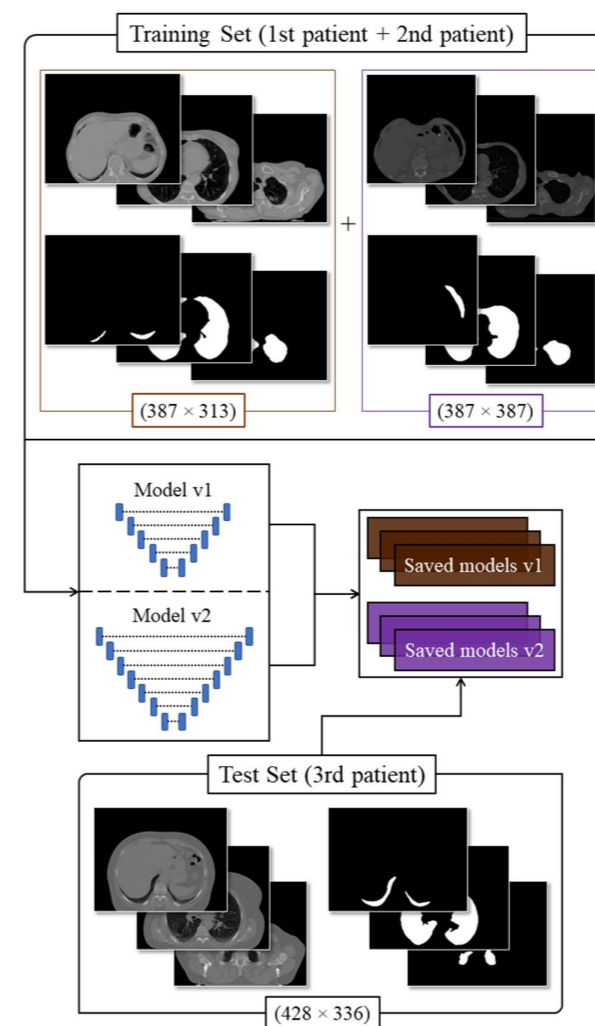

Fig. 3. Samples of the input images and their respective GTs, taken from the first, second and third patient sets with dimensions equal to (387 × 313), (387 × 387) and (428 × 336), respectively. The training images feed the models that after being saved are loaded with new test images.

C. Network Architecture

With the images properly formatted, the next step was to build the U-Nets models. Taking into account the impact that the number of levels can have on the final performance, two network configurations were implemented (v1 and v2), respectively with 5 and 7 levels, see Fig. 1 and Fig. 2.

The convolution layers are two-dimensional, followed by max-pooling layers. ReLU [35] is the activation function inherent to the process. The dropout is used to avoid overfitting, while the concatenation layers illustrate the skip-connection action [26], [15].

Training a CNN for segmentation or classification can be summarized as minimizing the loss function. To complement this learning process, the Adam optimizer was used. After the architecture design was finalized, training methods were assigned to the network function.

D. Network Training

One of the techniques used to generalize the input data is "Data Augmentation", which generates new images coming

from the input images from different perspectives. Data Augmentation was used to generate input images and their respective GTs horizontally inverted, doubling the amount of images during training.

In view of the investigative study of BSs in the training stage, the callbacks "ReduceLRonPlateaus" and "EarlyStopping" from the Keras library were used. The purpose of this is to establish a common iteration for all models, allowing comparison of BSs.

The callbacks are used by DNN during training, and are a compilation of functions for monitoring the internal states and statistical results of the model [26], [36]. "EarlyStopping" is responsible for terminating the DNN training if the model does not show a decrease in the validation group error after a specific number of epochs, such number is called "patience".

During the training process, if there is no decrease in error for a "patience", "ReduceLRonPlateau" reduces the U-Net learning rate. This method is used to avoid a local optima and find the global optima.

To study the impact of BSs on network progress, the two architectures were trained with three different BSs; 4, 8 and 16. The analysis of the number of epochs was done by studying network performance according to loss.

"EarlyStopping" is a good way to establish the number of epochs a network needs. Through a series of preliminary tests, a number of epochs equal to 80 was empirically estimated for all models. Then, 10 trainings were done for each BS, that is, 30 models of each version of the neural network (v1 and v2), totaling 60 trained models.

E. Evaluation

To evaluate the performance of networks, it is necessary to have a number of models capable of covering various training scenarios. Therefore each net configuration was trained 10 times with random starts. This approach allows the models to be analyzed with a high degree of generalization and reproducibility.

This method consists of training the net with all training samples, for internal validation of the network. One of the sets (the testing set) is separated to test the model after training. The segmented images from the test set are separated and evaluated later.

In this sense, the set of two patients was divided into 80% of the images for training and 20% for internal validation of the network. The images from the third patient was used in the testing stage, where the performance data was collected based on the metrics established in the work.

Such a method is ideal for cases where there is little data, because the model error was calculated for each sample, obtaining a final average of the test volume and reducing the computational cost.

F. Dice Similarity Coefficient

There are several metrics to evaluate and validate DNN models. Generally, each metric can be applied in different situations, but there are certain fields where its use best matches the performance of the neural network, delivering higher reliability.

The Dice Similarity Coefficient (DSC) is a metric that analyzes the similarity between two samples [37]. DSC is commonly used in biomedical image analysis. It can be defined as the ratio of twice the area of overlap between segmentations and GTs by the total number of pixels [22].

The DSC is identical to the F1 Score [38] and has its mathematical representation described in (1). Where |·| represents the cardinality of sets A and B.

$$DSC = \frac{2|A \cap B|}{|A|+|B|} \quad (1)$$

In other words, the DSC is a measure that quantifies the degree of similarity between the segmented image obtained by the model and the reference image (GT) during the supervised training or testing step. The DSC for each image can vary between 0 (no overlap) and 1 (complete overlap).

G. Statistical Analysis

After the trainings, each model went through the testing step with the third patient data. After segmentation, the DSC of such a set was calculated. The scores were organized according to the network version and BS, so the comparison was made between BSs per model version.

To check for a possible statistically significant difference between BSs, the Kruskall-Wallis test [39] was used on the 6 groups of data, see Table 1. The p-value shows whether or not the null hypothesis shall be rejected for values above or below 5%. In this case, the null hypothesis is that there is no statistically significant difference between the groups if the p-value is less than the 0.05 threshold.

If there is statistically significant differences, Dunn's test [40] shall be used. Dunn's test aims to find which pairs of groups, within each version of the model, have a significant difference.

IV. RESULTS AND DISCUSSIONS

As described in the methodology, 60 DNNs were trained and the models were saved to receive the test images. Table 1 shows the scores of the v1 and v2 models with 10 runs for each BS. The bottom of Table 1 displays the mean, standard deviation, and the maximum and minimum value for each column.

From the preview results, it can be seen that all models obtained a performance above 90%, except for one of the v2 models with BS equal to 8. Such results reinforce the positive deliberations about U-Net.

A. Statistical Analysis of The Models

From these data, the Kruskal-Wallis test was applied, and the null hypothesis can be accepted, since the p-value was less than 5% (p-value < 0.05). The boxplots in Fig. 4, 5 and 6 show a trend towards higher DSCs for BSs equal to 16. This observation also occurs in Dunn's test, as described later.

Using larger batches allows the training time to be reduced. Dong et al. [18] used 35 thoracic CT sets to train the network, for these cases, not taking advantage of parallel processing can make training slow and error prone.

In [41]–[43], the authors used different methods to determine the training parameters, either through prior knowledge or experimental testing. The choice of parameters such as BS may be little debated, however, the statistical study of these parameters allows training to be optimized with greater reliability and reproducibility.

Kandel and Castelli [44] show a high correlation between BS and learning rate. According to the authors, large BSs perform better for large learning rates. Such a correlation can be tested in future work by bringing a statistical study on such parameters.

TABLE I. DSC VALUES FROM THE TEST WITH MODELS V1 AND V2

Executions[a]	Model v1			Model v2		
	Batch size 4	Batch size 8	Batch size 16	Batch size 4	Batch size 8	Batch size 16
0	0.951	0.957	0.918	0.952	0.959	0.963
1	0.960	0.958	0.955	0.955	0.957	0.964
2	0.960	0.957	0.969	0.958	0.956	0.965
3	0.950	0.960	0.975	0.953	0.950	0.964
4	0.960	0.937	0.975	0.959	0.864	0.969
5	0.950	0.958	0.954	0.959	0.957	0.957
6	0.952	0.958	0.963	0.965	0.958	0.958
7	0.956	0.957	0.971	0.959	0.962	0.961
8	0.958	0.960	0.965	0.956	0.952	0.962
9	0.962	0.963	0.976	0.957	0.955	0.947
Mean	0.956	0.956	0.962	0.957	0.947	0.961
Standard Deviation	0.004	0.007	0.017	0.017	0.017	0.017
Median	0.957	0.958	**0.967**	0.957	0.957	**0.963**
Maximum	0.962	0.963	0.976	0.965	0.962	0.969
Minimum	0.950	0.937	0.918	0.952	0.864	0.947

a. Running the tests, each index represents a test and its score from the model with the third patient images.
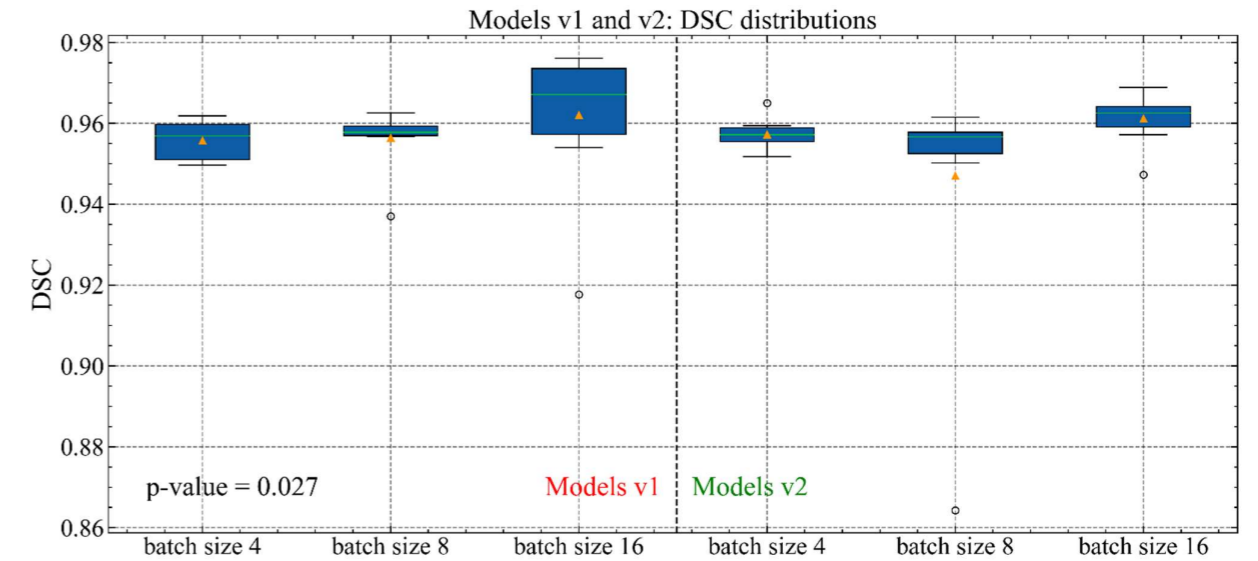
Fig. 4. Boxplot representing the distributions of each model, it contains the comparison between all groups. The p-value is shown in the lower left corner.
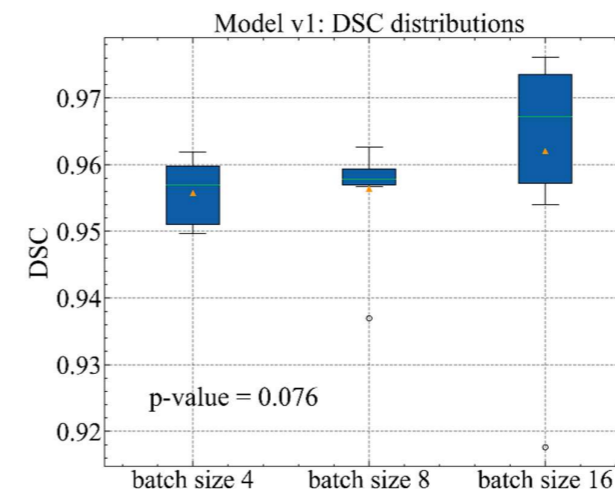

Fig. 5. Boxplot representing the distributions of model v1, it contains the comparison between all batch sizes. The p-value is in the lower left corner.
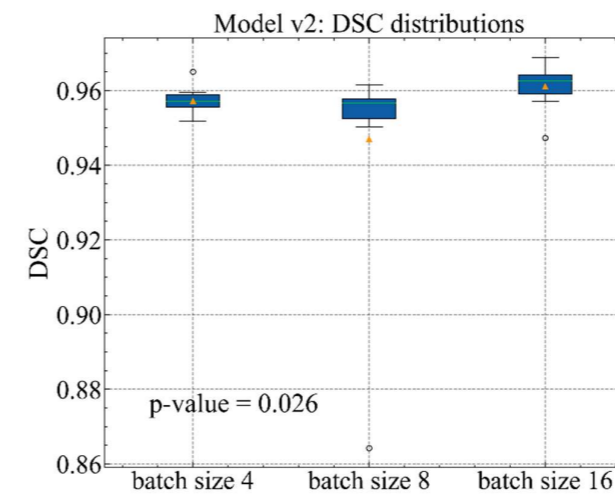

Fig. 6. Boxplot representing the distributions of model v2, it contains the comparison between all batch sizes. The p-value is in the lower left corner.

Regarding separately, each model in Fig. 5 and 6, only v2 has a statistically significant difference between the BSs (p-value = 0.026). The isolated results of v1 also tend to be different, but it is not conclusive (p-value = 0.076). Fig. 7 shows Dunn's test results for each model, highlighting BS 16, the main group responsible for the statistical divergences (p-value = 0.027).

The larger BS was favored with the increase of levels in the v2 model. However, regardless of the model, it is observed that the BS 16 is more likely to obtain better results and be applied in future works.

B. Practical Segmentation Analysis

The comparison in Fig. 8a allows exemplifying the origin of most of the losses in the metric, which is mostly located in the lower regions of the tone, such location is highlighted in red. This makes the stereology of the segmented lung volume different from the real one dictated by the GTs, i.e., a loss of white pixels in the segmented images.

The segmented lung volume, Fig. 8b (2), respects the shape of the organ, even with the small differences. Analyzing the volumes, one can see some irregularities on the surface of the segmented lung, a characteristic not found in the real volume, see Fig. 8b (1). In some biomedical applications, the small amount of samples leads to low data volume. The trained models were successful in segmenting the images, even with the use of 2 of the original 60 data sets.
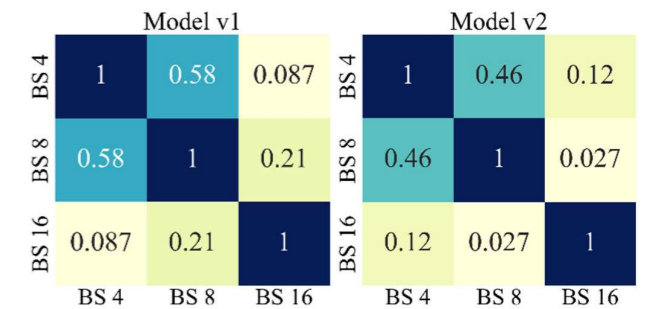

Fig. 7. Heatmap containing the results of the paired Dunn test for models v1 and v2. It shows which pairs have a statistically significant difference.
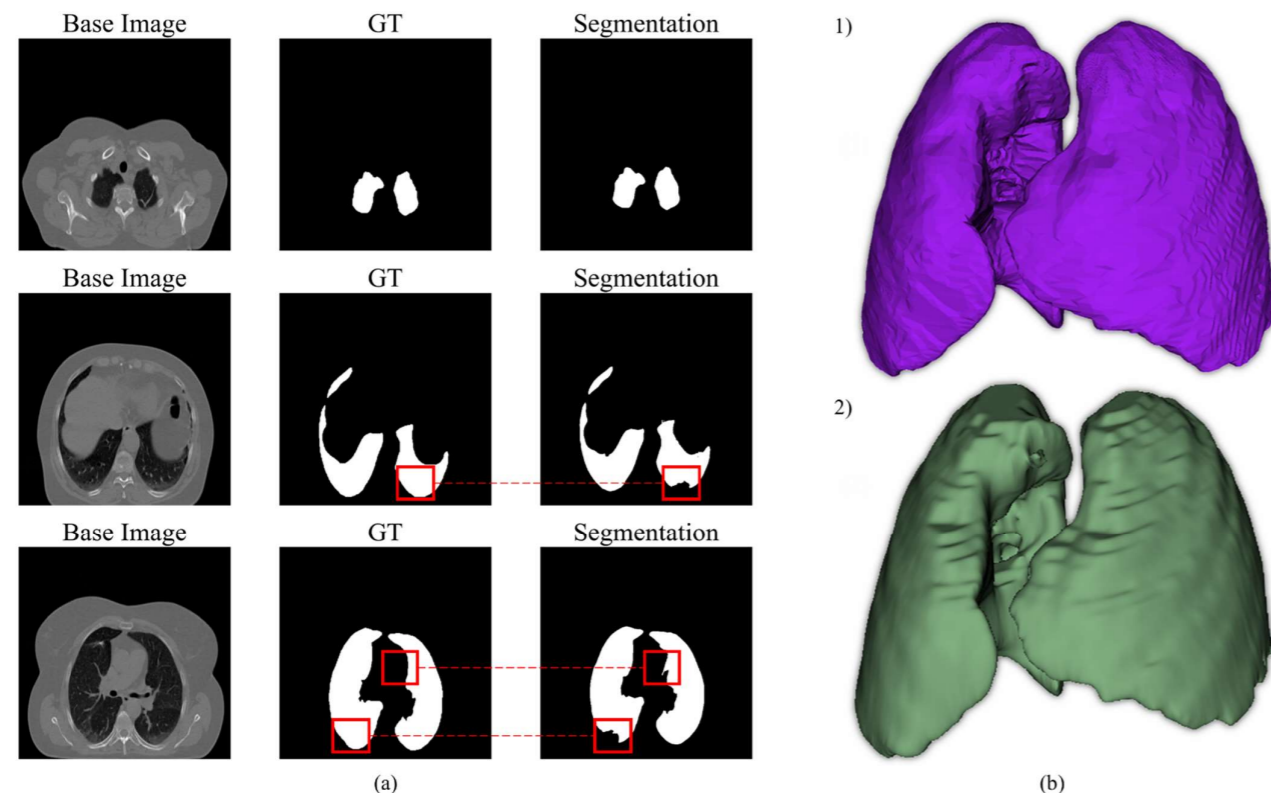
Fig. 8. (a) comparative examples of segmentation done by the model (v2) with batch size equal to 16 and (b) lung volumes from the third patient, the upper one (1) coming from the GTs and the lower one (2) from the segmentations of the model used in (a).

V. Conclusions

From the results, it was possible to establish some aspects regarding the variability of U-Net. BS has a significant impact for model v2. The v1 model, despite not reaching statistical criteria, showed similar behavior to the v2 model. Increasing the levels slightly improved the results, raising hypotheses for future work involving networks with different levels. This perspective can be evaluated with other network parameters.

Although adding levels has achieved a performance gain that is sensitive to statistical tests, there are other ways to achieve considerable gains. New architectures, such as 3D U-Net [16], U-Net++ [45], U-Net 3+ [46] and ELU-Net [47], present a substantial gain through other non-trivial modifications and could be applied in future work.

According to the analyses, BSs equal to 16 provided better results while reducing training time due to parallel processing. Thus, BSs equal to 16 are suitable for future biomedical research, and can be increased as the number of images for training increases.

However, it is hoped to investigate the BS in combination with other parameters and features of the model, such as the learning rate or network levels. In [44] the authors showed the correlation between these parameters, but between different learning optimizers.

References

[1] A. Owoyemi, J. Owoyemi, A. Osiyemi, and A. Boyd, "Artificial Intelligence for Healthcare in Africa," *Front Digit. Health*, vol. 2, Jul. 2020, doi: 10.3389/fdgth.2020.00006.

[2] C. C. Onu, J. Lebensold, W. L. Hamilton, and D. Precup, "Neural Transfer Learning for Cry-Based Diagnosis of Perinatal Asphyxia," in *Interspeech 2019*, Sep. 2019, pp. 3053–3057. doi: 10.21437/Interspeech.2019-2340.

[3] V. Bellemo et al., "Artificial intelligence using deep learning to screen for referable and vision-threatening diabetic retinopathy in Africa: a clinical validation study," *Lancet Digit. Health*, vol. 1, no. 1, pp. e35–e44, May 2019, doi: 10.1016/S2589-7500(19)30004-4.

[4] Y. LeCun, Y. Bengio, and G. Hinton, "Deep learning," *Nature*, vol. 521, no. 7553, pp. 436–444, May 2015, doi: 10.1038/nature14539.

[5] M. A. Wani, F. A. Bhat, S. Afzal, and A. I. Khan, Advances in Deep Learning, vol. 57. *Singap.: Springer Singap.*, 2020. doi: 10.1007/978-981-13-6794-6.

[6] M. K. Santos, J. R. Ferreira Júnior, D. T. Wada, A. P. M. Tenório, M. H. Nogueira-Barbosa, and P. M. de A. Marques, "Artificial intelligence, machine learning, computer-aided diagnosis, and radiomics: advances in imaging towards to precision medicine," *Radiol. Bras.*, vol. 52, no. 6, pp. 387–396, Dec. 2019, doi: 10.1590/0100-3984.2019.0049.

[7] N. Shusharina et al., "Cross-Modality Brain Structures Image Segmentation for the Radiotherapy Target Definition and Plan Optimization," in *Segmentation, Classification, and Registration of Multi-modality Med. Imag. Data, Cham: Springer*, 2021, pp. 3–15. doi: 10.1007/978-3-030-71827-5_1.

[8] P. Iassonov, T. Gebrenegus, and M. Tuller, "Segmentation of X-ray computed tomography images of porous materials: A crucial step for characterization and quantitative analysis of pore structures," *Water Resour. Res.*, vol. 45, no. 9, Sep. 2009, doi: 10.1029/2009WR008087.

[9] A. Buratti, J. Bredemann, M. Pavan, R. Schmitt, and S. Carmignato, "Applications of CT for Dimensional Metrology," in *Industrial X-Ray Computed Tomography, Cham: Springer Int. Publishing*, 2018, pp. 333–369. doi: 10.1007/978-3-319-59573-3_9.

[10] A. Alvarenga de Moura Meneses et al., "Automated segmentation of synchrotron radiation micro-computed tomography biomedical images using Graph Cuts and neural networks," *Nucl. Instrum. Methods Phys. Res. A*, vol. 660, no. 1, pp. 121–129, Dec. 2011, doi: 10.1016/j.nima.2011.08.007.

[11] A. El-Baz, X. Jiang, and J. S. Suri, Biomedical Image Segmentation: Advances and Trends. 2016.

[12] A. A. de M. Meneses, D. B. Palheta, C. J. G. Pinheiro, and R. C. R. Barroso, "Graph cuts and neural networks for segmentation and porosity quantification in Synchrotron Radiation X-ray μCT of an igneous rock sample," *Appl. Radiat. and Isot.*, vol. 133, pp. 121–132, Mar. 2018, doi: 10.1016/j.apradiso.2017.12.019.

[13] J. Yang et al., "Autosegmentation for thoracic radiation treatment planning: A grand challenge at AAPM 2017," *Med. Phys.*, vol. 45, no. 10, pp. 4568–4581, Oct. 2018, doi: 10.1002/mp.13141.

[14] M. K. Santos, J. R. Ferreira Júnior, D. T. Wada, A. P. M. Tenório, M. H. Nogueira-Barbosa, and P. M. de A. Marques, "Artificial intelligence, machine learning, computer-aided diagnosis, and radiomics: advances in imaging towards to precision medicine," *Radiol. Bras.*, vol. 52, no. 6, pp. 387–396, Dec. 2019, doi: 10.1590/0100-3984.2019.0049.

[15] O. Ronneberger, P. Fischer, and T. Brox, "U-Net: Convolutional Networks for Biomedical Image Segmentation," in *Med. Image Comput. and Computer-Assisted Intervention, Cham: Springer*, 2015, pp. 234–241. doi: 10.1007/978-3-319-24574-4_28.

[16] Ö. Çiçek, A. Abdulkadir, S. S. Lienkamp, T. Brox, and O. Ronneberger, "3D U-Net: Learning Dense Volumetric Segmentation from Sparse Annotation," in *Med. Image Comput. and Computer-Assisted Intervention, Cham: Springer*, 2016, pp. 424–432. doi: 10.1007/978-3-319-46723-8_49.

[17] J. C. González Sánchez, M. Magnusson, M. Sandborg, Å. Carlsson Tedgren, and A. Malusek, "Segmentation of bones in medical dual-energy computed tomography volumes using the 3D U-Net," *Physica Medica*, vol. 69, pp. 241–247, Jan. 2020, doi: 10.1016/j.ejmp.2019.12.014.

[18] X. Dong et al., "Automatic multiorgan segmentation in thorax CT images using U-net-GAN," *Med. Phys.*, vol. 46, no. 5, pp. 2157–2168, May 2019, doi: 10.1002/mp.13458.

[19] P. F. Christ et al., "Automatic Liver and Lesion Segmentation in CT Using Cascaded Fully Convolutional Neural Networks and 3D Conditional Random Fields," in *Med. Image Comput. and Computer-Assisted Intervention, Cham: Springer*, 2016, pp. 415–423. doi: 10.1007/978-3-319-46723-8_48.

[20] K. Paiva et al., "Performance evaluation of segmentation methods for assessing the lens of the frog Thoropa miliaris from synchrotron-based phase-contrast micro-CT images," *Physica Medica*, vol. 94, pp. 43–52, Feb. 2022, doi: 10.1016/j.ejmp.2021.12.013.

[21] G. Sena et al., "Synchrotron X-ray biosample imaging: opportunities and challenges," *Biophys. Rev.*, vol. 14, no. 3, pp. 625–633, Jun. 2022, doi: 10.1007/s12551-022-00964-4.

[22] S. Minaee, Y. Y. Boykov, F. Porikli, A. J. Plaza, N. Kehtarnavaz, and D. Terzopoulos, "Image Segmentation Using Deep Learning: A Survey," *IEEE Trans. Pattern Anal. Mach. Intell.*, pp. 1–1, 2021, doi: 10.1109/TPAMI.2021.3059968.

[23] S. Ghosh, N. Das, I. Das, and U. Maulik, "Understanding Deep Learning Techniques for Image Segmentation," *ACM Comput. Surv.*, vol. 52, no. 4, pp. 1–35, Jul. 2020, doi: 10.1145/3329784.

[24] C. Chen et al., "Deep Learning for Cardiac Image Segmentation: A Review," *Front Cardiovasc. Med.*, vol. 7, Mar. 2020, doi: 10.3389/fcvm.2020.00025.

[25] Y. Lecun, L. Bottou, Y. Bengio, and P. Haffner, "Gradient-based learning applied to document recognition," *Proc. of the IEEE*, vol. 86, no. 11, pp. 2278–2324, 1998, doi: 10.1109/5.726791.

[26] Francois Chollet, Deep Learning with Python, 2nd ed. 2021.

[27] D. E. Rumelhart, G. E. Hinton, and R. J. Williams, "Learning representations by back-propagating errors," *Nature*, vol. 323, no. 6088, pp. 533–536, Oct. 1986, doi: 10.1038/323533a0.

[28] S. Wang, D. M. Yang, R. Rong, X. Zhan, and G. Xiao, "Pathology Image Analysis Using Segmentation Deep Learning Algorithms," *Am J Pathol*, vol. 189, no. 9, pp. 1686–1698, Sep. 2019, doi: 10.1016/j.ajpath.2019.05.007.

[29] A. Voulodimos, N. Doulamis, A. Doulamis, and E. Protopapadakis, "Deep Learning for Computer Vision: A Brief Review," *Comput.*

[30] N. Siddique, S. Paheding, C. P. Elkin, and V. Devabhaktuni, "U-Net and Its Variants for Medical Image Segmentation: A Review of Theory and Applications," *IEEE Access*, vol. 9, pp. 82031–82057, 2021, doi: 10.1109/ACCESS.2021.3086020.

[31] Y. Sha, D. J. Gagne II, G. West, and R. Stull, "Deep-Learning-Based Gridded Downscaling of Surface Meteorological Variables in Complex Terrain. Part I: Daily Maximum and Minimum 2-m Temperature," *J Appl. Meteorol. Climatol.*, vol. 59, no. 12, pp. 2057–2073, Dec. 2020, doi: 10.1175/JAMC-D-20-0057.1.

[32] K. Clark et al., "The Cancer Imaging Archive (TCIA): Maintaining and Operating a Public Information Repository," *J Digit. Imaging*, vol. 26, no. 6, pp. 1045–1057, Dec. 2013, doi: 10.1007/s10278-013-9622-7.

[33] "Data from Lung CT Segmentation Challenge," The Cancer Imaging Archive, May 2017.

[34] J. Yang et al., "Autosegmentation for thoracic radiation treatment planning: A grand challenge at AAPM 2017," *Med. Phys.*, vol. 45, no. 10, pp. 4568–4581, Oct. 2018, doi: 10.1002/mp.13141.

[35] N. Vinod and E. H. Geoffrey, "Rectified Linear Units Improve Restricted Boltzmann Machines," in ICML, Jan. 2010.

[36] T. Hastie, J. Friedman, and R. Tibshirani, The Elements of Statistical Learning. New York, NY: *Springer New York*, 2001. doi: 10.1007/978-0-387-21606-5.

[37] T. J. Sorensen, A method of establishing groups of equal amplitude in plant sociology based on similarity of species content and its application to analyses of the vegetation on Danish commons. I kommission hos E. Munksgaard, 1948.

[38] C. Sammut and G. I. Webb, Eds., Encyclopedia of Machine Learning. Springer Science & Business Media, 2011.

[39] W. H. Kruskal and W. A. Wallis, "Use of Ranks in One-Criterion Variance Analysis," *J Am Stat. Assoc.*, vol. 47, no. 260, pp. 583–621, Dec. 1952, doi: 10.1080/01621459.1952.10483441.

[40] O. J. Dunn, "Multiple Comparisons among Means," *J Am Stat. Assoc.*, vol. 56, no. 293, pp. 52–64, Mar. 1961, doi: 10.1080/01621459.1961.10482090.

[41] B. Acun, M. Murphy, X. Wang, J. Nie, C.-J. Wu, and K. Hazelwood, "Understanding Training Efficiency of Deep Learning Recommendation Models at Scale," in *2021 IEEE International Symposium on High-Performance Computer Architecture (HPCA)*, Feb. 2021, pp. 802–814. doi: 10.1109/HPCA51647.2021.00072.

[42] N. Kumari and B. S. Saini, "Fully Automatic Wheat Disease Detection System by Using Different CNN Models," in *Sentiment Anal. and Deep Learn. Advances in Intell. Syst. and Comput., Singap.: Springer Singap.*, 2023, pp. 351–365. doi: 10.1007/978-981-19-5443-6_26.

[43] S. R. Nayak, D. R. Nayak, U. Sinha, V. Arora, and R. B. Pachori, "An Efficient Deep Learning Method for Detection of COVID-19 Infection Using Chest X-ray Images," *Diagnostics*, vol. 13, no. 1, p. 131, Dec. 2022, doi: 10.3390/diagnostics13010131.

[44] I. Kandel and M. Castelli, "The effect of batch size on the generalizability of the convolutional neural networks on a histopathology dataset," *ICT Express*, vol. 6, no. 4, pp. 312–315, Dec. 2020, doi: 10.1016/j.icte.2020.04.010.

[45] Z. Zhou, M. M. Rahman Siddiquee, N. Tajbakhsh, and J. Liang, "UNet++: A Nested U-Net Architecture for Medical Image Segmentation," in *Deep Learn. in Med. Image Anal. and Multimodal Learn. for Clin. Decis. Support, Cham: Springer*, 2018, pp. 3–11. doi: 10.1007/978-3-030-00889-5_1.

[46] H. Huang et al., "UNet 3+: A Full-Scale Connected UNet for Medical Image Segmentation," in *ICASSP 2020 - 2020 IEEE Int. Conf. on Acoustics, Speech and Signal Process. (ICASSP)*, Barcelona, Spain, 2020, pp. 1055-1059, doi: 10.1109/ICASSP40776.2020.9053405.

[47] Y. Deng, Y. Hou, J. Yan, and D. Zeng, "ELU-Net: An Efficient and Lightweight U-Net for Medical Image Segmentation," *IEEE Access*, vol. 10, pp. 35932–35941, 2022, doi: 10.1109/ACCESS.2022.3163711.

Intell. Neurosci., vol. 2018, pp. 1–13, 2018, doi: 10.1155/2018/7068349.

AUTHORS

Eduardo Stefanato

Eduardo Destefani Stefanato - Graduated in Physics from the Federal University of Espírito Santo. Has extensive computational experience with Python and MicroPython programming language (Machine Learning and Data Analysis). Experience and focus in Experimental Physics, signal analysis and characterization, prototyping, sensor handling and scientific programming. Worked as a student researcher and technician at the Telecommunications Laboratory (LabTel), which is part of the Center for Research, Innovation and Development (CPID) funded by FAPES (Foundation for Support of Research and Innovation of Espírito Santo). He has contributions in the making of firmwares and prototypes of microcontrollers with sensors applied to health and magnetometry, involved with Deep Learning applied to CT (Computed Tomography) images and micro-Synchrotron radiation tomography (μTC-RS), from the Cancer Imaging Archive and the Elettra Synchrotron in Trieste/IT, respectively. Currently, he is linked to the post-graduation program at the Physics Institute of the University of São Paulo (IFUSP), inserted in the project "Terahertz Photonics for the Study of Quantum Materials" financed by CNPq.

Vitor Oliveira

Vitor Souza Premoli Pinto de Oliveira - Degree in Physics at the Federal University of Espírito Santo - UFES. I have experience with the areas of Condensed Matter Physics and Electroacoustic and Piezoelectric Applications and Devices; and computational experience with Python programming language (Machine Learning and Deep Learning) by developing applications of Artificial Neural Networks (Deep ANNs) in imaging problems. I have knowledge of crystallography and structure of the minerals that compose the Sand and Silt fractions, as well as mineralogical quantification and x-ray diffraction techniques. Moreover, I have mastery in the use of piezoelectric sensors, through the project that had as theme the interaction between sensors and microcontrollers for making an electronic MIDI drum, where I used piezoelectric sensors as triggers controlled by an Arduino board. Nowadays, I am a master's student in Physics at the Physics Institute of the University of São Paulo (IFUSP), in the area of non-linear optics in photonic microdevices fabricated via laser writing technique.

Christiano Pinheiro

Christiano Jorge Gomes Pinheiro – The Professor Christiano has a degree in Physics from Universidade Federal do Rio de Janeiro (2002), master's at Engenharia Nuclear from Instituto Alberto Luiz Coimbra de Pós-Graduação e Pesquisa de Engenharia (2004) and doctorate at Engenharia Nuclear from Instituto Alberto Luiz Coimbra de Pós-Graduação e Pesquisa de Engenharia (2008). Has experience in Physics, focusing on Nuclear Disintegration and Radioactivity, acting on the following subjects: food irradiation, gamma radiation. He is currently Associate Professor III of the Department of Rural Engineering at the Federal University of Espírito Santo and is developing a project that seeks to associate histomorphometric parameters, derived from stereology, with statistics using artificial intelligence concepts, mainly for micro-Synchrotron radiation tomography (μTC-RS) and CT (Computed Tomography) images.

Regina Barroso

Regina Cély Barroso is Full Professor in the Physics Institute at the Rio de Janeiro State Univerty, UERJ, in Brazil, since 1986. Currently, she is the coordinator of the Laboratory of Applied Physics in Biomedical and Environmental Sciences, Lab_FisMed/UERJ. Dr. Barroso earned her BS in Physics at UERJ, MS and PhD in Nuclear Engineering from COPPE/Federal University of Rio de Janeiro in 1997. She published more than one hundred of papers in scientic journals and supervised more than thirty MS, PhD and postdoctor students. Her interests include the methodologies, instrumentation and applications of hard X-ray nanoprobes for quantitative three-dimensional imaging, propagation based phase contrast X-ray imaging, synchrotron based microtomography. Her research focus particularly on key applications of synchrotron X-ray on biomedical imaging.

AUTHORS

Anderson Meneses

Anderson Alvarenga de Moura Meneses - Graduated in Physics from the Federal University of Rio de Janeiro (2000), in Brazil. Master (2005) and doctorate (2010) degrees in Nuclear Engineering from COPPE Institute, at the Federal University of Rio de Janeiro, with a fellowship at the Dalle Molle Institute for Artificial Intelligence (IDSIA, University of Lugano, Switzerland) in 2009. Specialist in Systems Analysis, Design and Management from Pontifical Catholic University, in Rio de Janeiro (2008). Associate Professor at the Federal University of Western Pará (UFOPA). Head of the Computational Intelligence Laboratory (LabIC/UFOPA) since 2015. Leader of the Computational Intelligence and Optimization research group. Permanent member of the Postgraduate Program in Amazon Natural Resources (PPGRNA/UFOPA). Collaborating member of the Postgraduate Program in Society, Nature and Development (PPGSND/UFOPA). Researcher PQ2 granted by the Brazilian National Council for Scientific and Technological Development (CNPq/Brazil). Areas of interest: Nuclear Engineering (optimization of nuclear reactor fuel reload), Deep Learning (Time Series Prediction and Image Processing) and Energy (Artificial Intelligence applied to electrical energy consumption monitoring).

LATIN-AMERICAN JOURNAL OF COMPUTING

Published by

ESCUELA
POLITÉCNICA
NACIONAL

FIS

LAJC

LATIN-AMERICAN JOURNAL OF COMPUTING

Vol X, Issue 2,
July 2023

Indexed in: